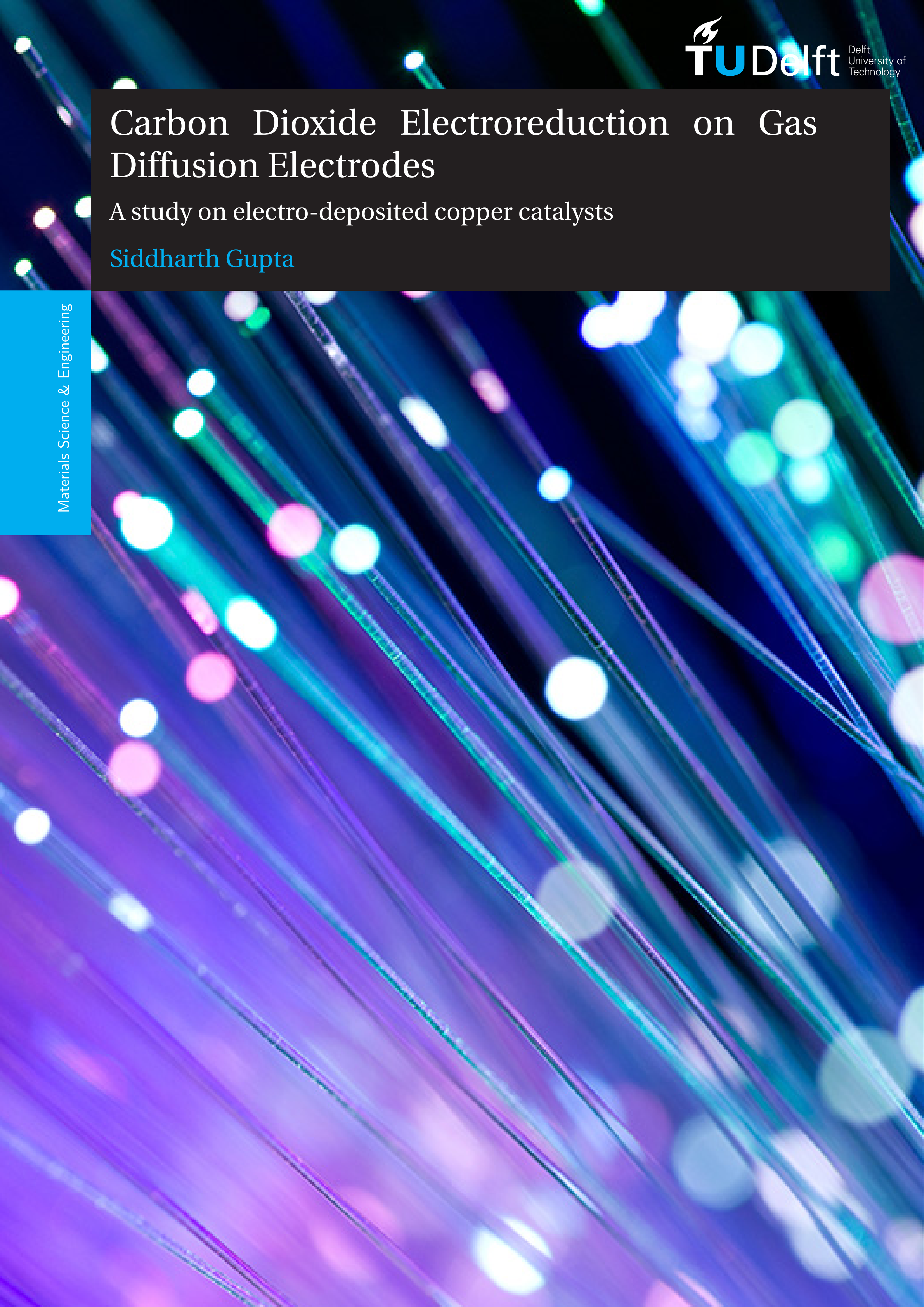

Carbon Dioxide Electroreduction on Gas Diffusion Electrodes

A study on electro-deposited copper catalysts

Siddharth Gupta

Materials Science & Engineering

CARBON DIOXIDE ELECTROREDUCTION ON GAS DIFFUSION ELECTRODES

A STUDY ON ELECTRO-DEPOSITED COPPER CATALYSTS

by

Siddharth Gupta

in partial fulfillment of the requirements for the degree of

Master of Science

in Materials Science and Engineering

at the Delft University of Technology,

to be defended publicly on **25 March 2020** at **10:00** in **Lecture Hall G, 3mE**

Student number	4738039
Project duration	May 2019 – Feb 2020

Daily Supervisors	
Dr. Francesc Sastre Calabuig,	Nederlandse Organisatie voor Toegepast Natuurwetenschappelijk Onderzoek
Dr. Robin White,	Nederlandse Organisatie voor Toegepast Natuurwetenschappelijk Onderzoek

Thesis Committee	
Dr. Arjan Mol,	Delft University of Technology
Dr. Ivan Buijnsters,	Delft University of Technology
Dr. Peyman Taheri,	Delft University of Technology
Dr. Robin White,	Nederlandse Organisatie voor Toegepast Natuurwetenschappelijk Onderzoek
Dr. Francesc Sastre Calabuig,	Nederlandse Organisatie voor Toegepast Natuurwetenschappelijk Onderzoek

This thesis is confidential and cannot be made public until March, 2022.

An electronic version of this thesis will be available from March, 2022 at
`http://repository.tudelft.nl/`.

“Arise, awake, and stop not until the goal is achieved.”

-Swami Vivekananda

ABSTRACT

Rapid industrialization and use of carbon based fuels has caused a drastic increase in the atmospheric CO_2 levels in the last few decades. The rising anthropogenic CO_2 levels pose a significant threat to the environment as evidenced by the increase in the mean global temperature levels, and the rising ocean levels. To mitigate the challenges associated with rising CO_2 levels, there is an urgent need to move towards carbon neutral sources of energy and to curb carbon emissions from large scale point emitters such as industries. Additionally, emitted CO_2 could be converted into energy dense organic fuels using carbon-neutral forms of energy. This not only helps in reducing the carbon emissions but also balances the intermittent nature of renewable energy supply. CO_2 could also be converted into platform chemicals such as ethylene/CO, which can be further up-converted or directly used in industry. Ethylene is particularly interesting due to its high energy density and wide industrial usage as a precursor in the polymer industry. Electroreduction of CO_2 provides one such approach to electrochemically convert CO_2 produced at large scale emitters to useful organic compounds. Different metallic catalysts are known to catalyse the electrochemical reduction towards different products, which follows from Sabatier's principle. In this study copper is used as the model catalyst due to its unique ability to electrochemically convert CO_2 to multi-carbon products, such as ethylene. From a cell-design perspective conventional electrochemical reduction of CO_2 in aq. media suffers from low production rates due to the low solubility of CO_2 in aq. electrolytes which makes it not feasible from an industrial standpoint. To overcome the low production rates, this study was carried out on novel gas diffusion electrodes. Another factor limiting the implementation of CO_2 electrolysers on an industrial scale, is the scalability of the catalyst synthesis. To improve this, electrodeposition of copper catalysts was employed. Electrodeposition is a well-established industrial technique and integrable within the existing infrastructure. Electrodeposition facilitates in-situ growth of the catalyst on gas diffusion layers, thereby providing a facile alternative to the conventional multi-step process for catalyst synthesis. Different morphologies of copper were synthesized by varying the electrodeposition process parameters. Copper nanowires were also synthesized by using templated electrodeposition techniques. The catalysts were characterised before and after the CO_2 reduction experiments by Scanning Electron Microscopy, and X- Ray Diffraction. CO_2 reduction experiments using the synthesised copper catalysts were carried out over a range of potentials. A peak Faradaic Efficiency (FE%) of 15% was measured at -1.5 V vs RHE (uncompensated) for ethylene, 19% FE at -1.1 V vs RHE for formic acid, and 13% FE at -1.5 V vs RHE for methane. It was also seen that the catalyst suffered from stability issues which were overcome by using pulsed electrolysis. Using pulsed electrolysis the lifetime of the catalyst was increased from 30 minutes to 15 hours.

ACKNOWLEDGEMENT

The great Austrian psychiatrist Viktor Frankl had said, " What man actually needs is not a tension-less state but rather the striving and struggling for some goal". Along the lines of Viktor's quote, completing this M.Sc has been the single most challenging yet rewarding experience of my life. I'd like to take this opportunity to thank everyone who has helped me in this journey, and specifically over the course of my M.Sc thesis.

Firstly, I would like to thank the faculty of Materials Science and Engineering, Delft University of Technology for providing students with a vibrant environment conducive to learning. I'd like to specially thank my thesis supervisors at the university, Dr. Ivan Buijnsters, and Prof. Dr. Arjan Mol for their guidance during this thesis. A special thanks to friends in Delft, Arjun, Devi, Nara, and, Sagar, for their support in the difficult times and for the countless memories during the MSE program.

I'd like to thank my supervisors at TNO, Materials Solutions(MaS), Dr. Francesc Sastre Calabuig, and Dr. Robin White, for giving me the opportunity to work on this challenging and interesting thesis project. Their scientific inputs at various stages, their support, and belief all played a huge role in me getting over the line with this study. The fun and insightful discussions we had during meetings and in the labs are something that I'll hold onto and cherish for the entirety of my life. I'll also miss the almost weekly motivational pep-talks.

I would like to thank every other staff member at TNO, specially Henk Rendering, for his help with the electrodeposition process, and Jorgen Sweelssen for his help with the XRD characterization. Special thanks to Jelle for all his help in the lab with the experimental setup, random experimental hiccups, and for all the deeply "*insightful*" conversations about anything and everything. The rather bizarre music him and Javier had playing in the labs made working at MaS a bit more challenging yet fun. If not science, I've atleast learnt the lyrics to a few Dutch carnaval songs, "*Ik Moet Zuipen ......*". This acknowledgement would not be complete without me thanking my fellow interns Sander, Quentin, Pau, Stan, Arianne and Bram for all the fun times and for their highly intellectual critique of Dutch food everyday at lunch. I'd also like to thank the flatmates I've had over the 2 odd years, Karel, Daniel, Quiterie, Pedro, Diwa and Tomo for showing me that there exists a world outside of Indian food.

I also want to express my gratitude to my parents and brother for always being there, supporting me through every decision I've taken in my life, and for being a constant source of inspiration. No amount of words could ever reflect the sacrifices you as parents have made to see both your children succeed in life. Finally, I thank God for blessing me with the required mental fortitude and direction to complete this study.

Siddharth Gupta
Eindhoven, Feb 2020

CONTENTS

List of Figures xi

1 Introduction 1

1.1 Background 1

1.2 Electrochemical Reduction 3

1.3 Research Goals 5

1.4 Approach 6

1.5 Report Outline 6

2 Theoretical Background 7

2.1 CO_2 Conversion Techniques 7

2.2 Carbon Dioxide Electroreduction 8

2.2.1 H-cell Configuration 9

2.2.2 Gas Diffusion Electrodes 10

2.2.3 Reaction Mechanism. 10

2.3 Catalysts 12

2.3.1 Copper electrocatalysts 14

2.3.2 Electrocatalyst Synthesis 14

3 Experimental Method 15

3.1 Electroreduction Experiments 15

3.2 Catalyst Synthesis 18

3.3 Product Analysis Techniques 20

3.3.1 Gas Chromatograhy (GC) 20

3.3.2 High Performance Liquid Chromatography (HPLC) 21

3.4 Electrocatalyst characterisation 22

3.4.1 Scanning Electron Microscopy (SEM) 22

3.4.2 Energy Dispersive X-ray Spectroscopy (EDX) 22

3.4.3 X-Ray Diffraction (XRD) 22

3.4.4 Cyclic Voltammetry 23

4 Catalysts **25**

4.1 Carbon Cloth with Microporous Layer 25

4.1.1 Morphology 1 - 100mA 25

4.1.2 Morphology 2 - 50mA 26

4.1.3 Morphology 3 - 10mA 28

4.1.4 Discussion 29

4.2 Copper Nanowires 30

4.2.1 Approaches to overcome CO_2 diffusion limitations 33

5 CO_2 RR Results and Discussion **37**

5.1 Current Density 37

5.2 Ethylene 39

5.3 Methane 40

5.4 Formic Acid 42

5.5 Post CO_2RR Catalyst Characterisation 44

5.5.1 SEM 44

5.5.2 XRD 46

5.6 Discussion 46

5.6.1 Catalyst Deactivation 48

5.7 Pulsed Electrolysis 48

6 Conclusion & Future Outlook **53**

6.1 Conclusion 53

6.2 Future Recommendations 54

A GC Calibration **55**

B HPLC Calibration **59**

C Gas Diffusion Layer Properties **61**

C.1 GDL Properties 61

C.2 Raman Spectra 62

D SEM Images **63**

E Supplementary CO_2 RR Data **71**

E.1 Reaction Parameters 71

E.2 Reproducibility 71

Glossary **73**

Bibliography **75**

LIST OF FIGURES

1.1 Atmospheric CO_2 Levels . . . 1

1.2 Global Land Ocean Temperature Index . . . 2

1.3 Global sea level observations . . . 2

1.4 Incorporating electrochemical CO_2 conversion in the carbon cycle . . . 3

1.5 Schematic of an electrochemical cell . . . 4

1.6 Schematic depicting the differences in aqueous phase and vapor fed electrodes . . . 4

1.7 Electrochemical CO_2 reduction on metallic catalysts . . . 5

2.1 Electrochemical CO_2 Conversion Reactions with Equilibrium Potentials . . . 8

2.2 Main Products of the electrochemical reduction of CO_2 . . . 9

2.3 Schematic of an aqueous media H-cell electrochemical setup for Co_2 reduction . . . 9

2.4 Schematic of a gas diffusion electrode based CO_2 reduction system . . . 10

2.5 Mechanistic Pathways for CO2 electroreduction to CH_4 and C_2H_4 . . . 11

2.6 Binding Strength of Reaction Intermediates on FCC(111) facet of Transition Metals . . . 12

2.7 **Mechanistic Pathways for CO^* electroreduction to CH_4 and C_2H_4** . . . 13

2.8 Highly Selective/active metal and metal-derived electrocatalysts for synthesis of specific CO_2 RR products . . . 13

3.1 Schematic of the electrochemical cell used for the CO_2 RR experiments . . . 16

3.2 Electrochemical cell used for the CO_2 RR experiments . . . 16

3.3 Setup for the CO_2 RR experiments . . . 16

3.4 Schematic of the electrodeposition setup . . . 19

3.5 Electrodeposition setup for catalyst synthesis . . . 19

3.6 Electrodeposition holder . . . 20

3.7 Cyclic Voltammetry . . . 23

4.1 XRD Spectra of Morphology 1 . . . 26
4.2 SEM Micrograph of Morphology 1 - 350x . . . 26
4.3 SEM Micrograph of Morphology 1 - 2500x . . . 26
4.4 SEM Micrograph of Morphology 1 - 8500x . . . 26
4.5 SEM Micrograph of Morphology 2 - 250x . . . 27
4.6 SEM Micrograph of Morphology 2 - 2500x . . . 27
4.7 SEM Micrograph of Morphology 2 - 10000x . . . 27
4.8 XRD Spectra of Morphology 2 . . . 27
4.9 SEM Micrograph of Morphology 3 - 350x . . . 28
4.10 SEM Micrograph of Morphology 3 - 2500x . . . 28
4.11 SEM Micrograph of Morphology 3 - 10000x . . . 28
4.12 XRD Spectra of Morphology 3 . . . 28
4.13 XRD Spectra of the 3 different morphologies on Carbon Cloth - W1S1009 . . . 29
4.14 Schematic of the nanowire plating setup . . . 30
4.15 Schematic depicting the synthesis approach for copper nanowires . . . 31
4.16 SEM micrograph of Synthesized copper nanowires - 750x . . . 31
4.17 SEM micrograph of Synthesized copper nanowires - 10000x . . . 31
4.18 XRD spectra of copper nanowires . . . 32
4.19 Porosity issue with copper nanowires . . . 33
4.20 Masking during evaporation of metal to provide diffusion pathways for CO_2 . . . 33
4.21 Electrodepostion of copper on masked PCTE templates . . . 34
4.22 In-situ growth of nanowires on the GDL . . . 35
4.23 SEM Micrograph of in-situ copper nanowire growth approach . . . 35
4.24 SEM Micrograph of in-situ copper nanowire growth approach . . . 35
4.25 Backscatter SEM micrograph of in-situ copper nanowire growth . . . 36

5.1 Current Density vs Time 38

5.2 Current density vs Potential 38

5.3 Ethylene Faradaic Efficiency 39

5.4 Ethylene Flow 40

5.5 Methane Faradaic Efficiency 41

5.6 Methane Flow 41

5.7 Formic Acid Production 42

5.8 Formic Acid Production 43

5.9 Formic Acid Faradaic Efficiency 43

5.10 SEM after CO_2 RR experiment at -1.1V 44

5.11 SEM after CO_2 RR experiment at -1.2V 44

5.12 SEM after CO_2 RR experiment at -1.3V 45

5.13 SEM after CO_2 RR experiment at -1.4V 45

5.14 SEM after CO_2 RR experiment at -1.5V 45

5.15 SEM after CO_2 RR experiment at -1.6V 45

5.16 XRD Post CO_2 RR 46

5.17 CO_2 RR Products vs Potential 47

5.18 CO_2 RR Products vs Potential 47

5.19 Current Density and Potential for the pulsed electrolysis experiments 49

5.20 Current Density and hydrogen flow rate for the pulsed electrolysis experiments 49

5.21 Current Density and ethylene flow rate for the pulsed electrolysis experiments 50

5.22 Potential and ethylene flow rate for the pulsed electrolysis experiments 51

A.1 Calibration Curves for different gases with their corresponding equations and R^2 values 57

B.1 Calibration Line for Formic Acid 59

C.1 Raman Spectra of the GDL used 62

D.1 SEM Micrograph of Morphology 1 - 350x (Enlarged) 64

D.2 SEM Micrograph of Morphology 1 - 2500x (Enlarged) 64
D.3 SEM Micrograph of Morphology 1 - 8500x (Enlarged) 65
D.4 SEM Micrograph of Morphology 2 - 250x (Enlarged) 65
D.5 SEM Micrograph of Morphology 2 - 2500x (Enlarged) 66
D.6 SEM Micrograph of Morphology 2 - 10000x (Enlarged) 66
D.7 SEM Micrograph of Morphology 3 - 350x (Enlarged) 67
D.8 SEM Micrograph of Morphology 3 - 2500x (Enlarged) 67
D.9 SEM Micrograph of Morphology 3 - 10000x (Enlarged) 68
D.10 SEM micrograph of Synthesized copper nanowires - 750x (Enlarged) 68
D.11 SEM micrograph of Synthesized copper nanowires - 10000x (Enlarged) 69

E.1 FE% of the products with error 72

1

INTRODUCTION

1.1. BACKGROUND

During the past century, there has been a steady increase in the concentration of atmospheric carbon dioxide (Fig. 1.1) which has contributed significantly to the increasingly visible global warming and associated climate change. This is evidenced by the increase in the mean global temperatures by 0.9°C since the late 19th century,[1] (Fig. 1.2) a rise in the global mean sea level by 80mm in the last 20 years (Fig. 1.3), and an increase in the acidity of the oceans by about 30% amongst many other effects that pose significant consequences for our environment.[2]

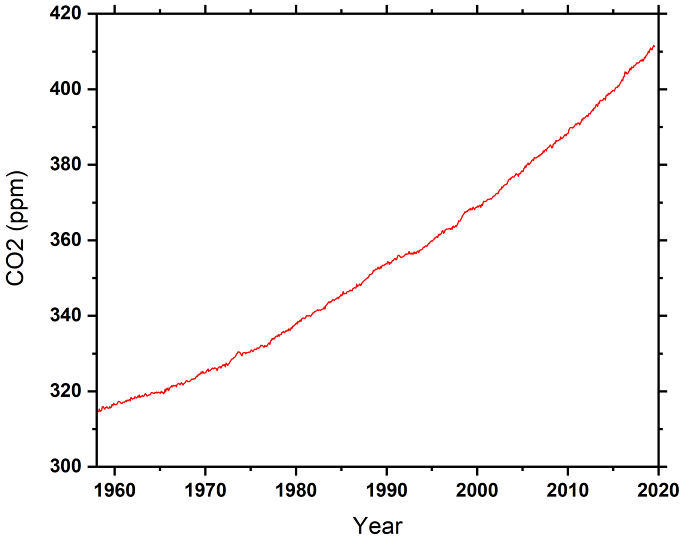

Figure 1.1: Atmospheric CO_2 levels corrected for seasonal variations. Data provided by the American Oceanic and Atmospheric Administration [2]

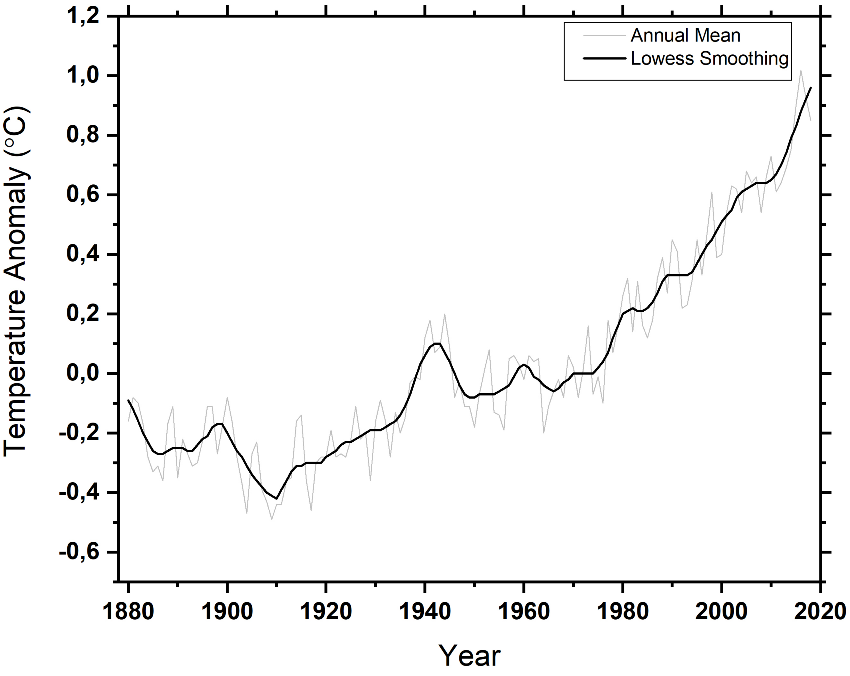

Figure 1.2: Change in global surface temperature relative to 1951-1980 average temperatures. Data provided by NASA's Goddard Institute for Space Studies (GISS)[3]

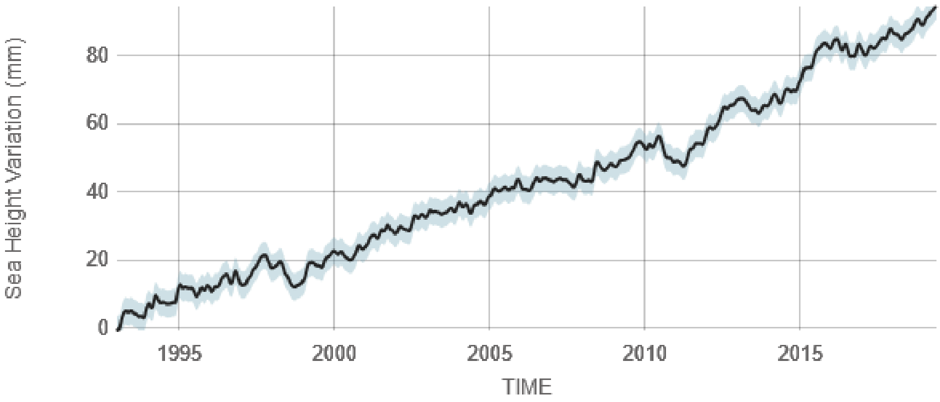

Source: climate.nasa.gov

Figure 1.3: Global mean sea level observations. Data provided by NASA's Goddard Space Flight Center [4]

Studies by the Intergovernmental Panel on Climate Change (IPCC), suggest that to stabilize atmospheric CO_2 concentrations at 350-400 ppm, and to limit the mean global temperature increase within 2.0-2.4°C, the global CO_2 emissions in 2050 would need to be reduced to 50-80 % of the 2000 levels. [5] [6] To mitigate these challenges brought about due to the rising CO_2 levels, there is an urgent need to control CO_2 emissions. Carbon Capture & Sequestration at large scale point emitters of CO_2 like industrial plants has been proposed. [7] As an extension to this approach, captured carbon dioxide can be further converted into various chemical/organic feed-stocks like formic acid, methanol, and ethylene - commonly denoted as Carbon Capture & Utilisation. (CCU)

1.2. ELECTROCHEMICAL REDUCTION

Electrochemical reduction of $CO_2$is a promising technology falling under CCU which aims to electrochemically convert the captured CO_2 into energy dense compounds.[8] The schematic in Fig. 1.4, depicts how incorporating electroreduction of CO_2 can help close the carbon cycle whereby renewable energy sources (e.g solar/wind) power the electroreduction process rendering improved ecological production credentials (relative to conventional processes).

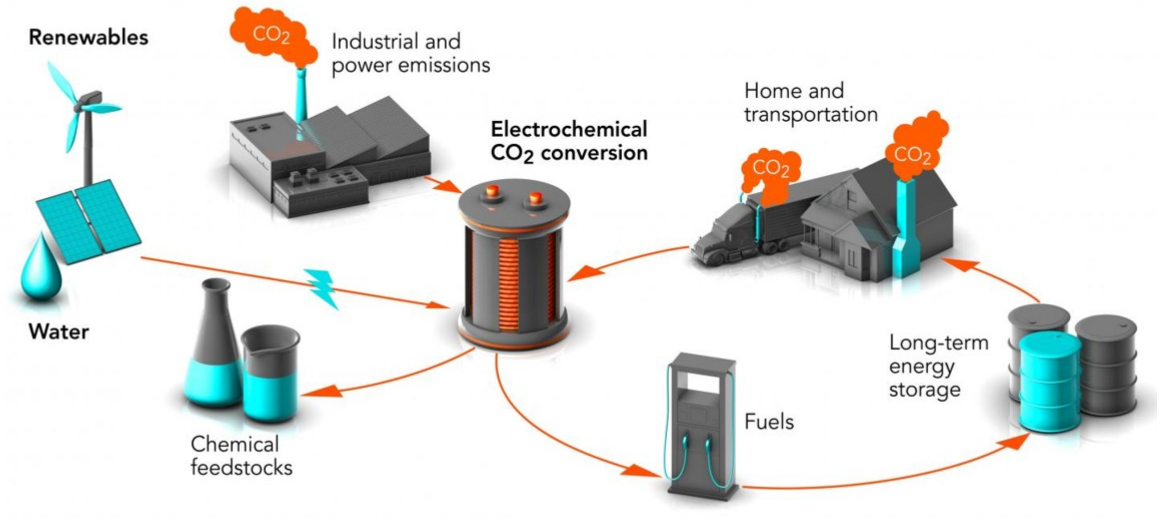

Figure 1.4: Incorporating electrochemical reduction in the carbon cycle [9]

By performing the electrochemical reduction reaction (commonly denoted in literature as CO_2 RR), it is possible to access a range of chemicals and fuels, the selectivity to which is often determined by a combination of electrocatalyst properties and process parameters. These include compounds such as ethanol or carbon monoxide, which can be employed directly as an energy carrier or as the basis for further up conversion via established processes (e.g. Fischer-Tropsch) to produce other chemicals and fuels. [10]

A representative schematic of the CO_2 RR process is depicted in Fig. 1.5. An electrochemical cell consists of two different compartments that are separated by a membrane which allows the diffusion of only H^+ ions. At the anode, hydrogen ions are produced by the oxidation of water. These hydrogen ions migrate to the cathode (catalyst), where they partake in the CO_2 RR process forming a range of different compounds depending upon the reaction parameters.

A key technological challenge to enable such a process is the synthesis of catalysts that convert CO_2 to de-

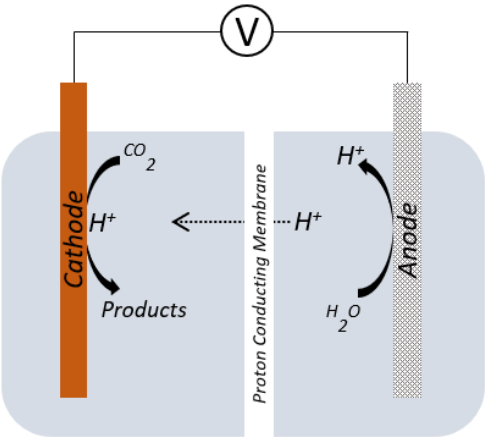
V
Cathode
CO_2
H^+
Products
Proton Conducting Membrane
H^+
H^+
H_2O
Anode

Figure 1.5: Schematic of an electrochemical cell for CO_2 RR

sired products at high energy efficiencies and production rates. [8] Currently CO_2 RR is typically carried out in CO_2 saturated aqueous electrolyte solutions. In this configuration the CO_2 molecules are solubilised in an aqueous electrolyte and reduced on the surface of a catalyst. The major drawback of using this kind of setup is the low current densities (10 mA cm^{-2}) due to the poor solubility of CO_2 in aqueous electrolytes (34 mM). [11] [12] Current densities are a direct indicator of the production rates of a particular compound. The higher the current density towards a particular compound, the higher its production rates. For industrial implementation of this technique, current densities ≥ 200 mA/cm^2 are desirable. [13] Such current densities cannot be obtained using conventional aqueous based reactors, due to limitations further discussed in Ch. 2. To overcome this issue of low current densities which limits scalability, vapour phase reactors (Gas Diffusion Electrodes - GDE) have been proposed as possible alternatives. These reactors overcome the solution phase mass transport limitations by providing hydrophobic channels that deliver the reactants to the catalyst in the gaseous phase. [11].

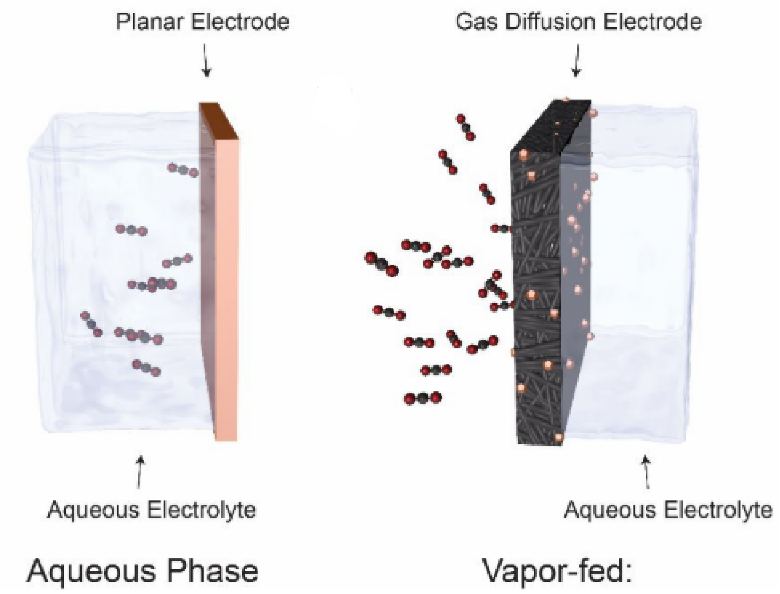
Planar Electrode
Gas Diffusion Electrode
Aqueous Electrolyte
Aqueous Electrolyte
Aqueous Phase
Vapor-fed:

Figure 1.6: Schematic depicting the differences in aqueous phase and vapor fed electrodes [12]

Fig. 1.6 depicts the basic difference in the mode of operation of the two types of reactors. In aq. phase reactors, the CO_2 being reduced is dissolved in the electrolyte, and hence the reaction rate is dependent on CO_2 solubility in the electrolyte. In the case of vapor-fed reactors, the CO_2 taking part in the reaction is in the gaseous state, and therefore the reaction rates are not limited by the solubility limit of the electrolyte thereby achieving higher current densities. [14]

The reduction process can be tuned to obtain different products by employing different process parameters and catalysts. Fig. 1.7 lists some conventionally formed products on metallic catalysts along with their corresponding faradaic efficiencies (FE%). As is seen from Fig. 1.7, carbon monoxide and formic acid are the most commonly formed reaction products. High faradaic efficiency of 80-90% have been obtained by various research groups for these two products. For multi-carbon compounds though the obtained faradaic efficiencies are much lower than C_1 compounds due to the reactions consisting of multiple steps and reaction intermediates. Multi-carbon compounds, specifically ethylene is industrially relevant due to its high energy density (50.4 MJ/kg; cf. 0.65 MJ/kg of Li-ion battery) and use as a precursor in the polymer industry. [15] Liquid products such as formic acid are also significant due to their use in the leather and rubber industry and also for their use in Direct Formic-Acid fuel cells.[16] Other liquid compounds such as methanol and ethanol are also widely used in industries and are relevant to the energy sector.

Fig. 1.7 shows that copper is one of the only metallic catalysts that can be used to obtain multi-carbon compounds such as ethylene and liquid reduction products. This peculiar property of copper to produce a wider array of compounds can be attributed to its reaction with the various intermediates. This is discussed in more detail in the forthcoming chapters. Due to the high industrial relevance of the products obtained using copper based catalysts it is chosen as the catalyst for the course of this study.

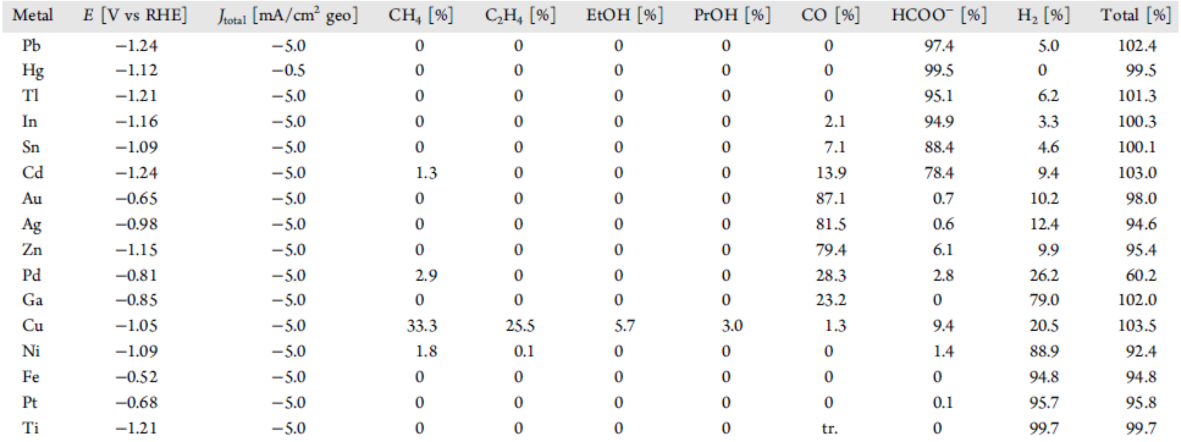

Metal	E [V vs RHE]	J_{total} [mA/cm^2 geo]	CH_4 [%]	C_2H_4 [%]	EtOH [%]	PrOH [%]	CO [%]	$HCOO^-$ [%]	H_2 [%]	Total [%]
Pb	−1.24	−5.0	0	0	0	0	0	97.4	5.0	102.4
Hg	−1.12	−0.5	0	0	0	0	0	99.5	0	99.5
Tl	−1.21	−5.0	0	0	0	0	0	95.1	6.2	101.3
In	−1.16	−5.0	0	0	0	0	2.1	94.9	3.3	100.3
Sn	−1.09	−5.0	0	0	0	0	7.1	88.4	4.6	100.1
Cd	−1.24	−5.0	1.3	0	0	0	13.9	78.4	9.4	103.0
Au	−0.65	−5.0	0	0	0	0	87.1	0.7	10.2	98.0
Ag	−0.98	−5.0	0	0	0	0	81.5	0.6	12.4	94.6
Zn	−1.15	−5.0	0	0	0	0	79.4	6.1	9.9	95.4
Pd	−0.81	−5.0	2.9	0	0	0	28.3	2.8	26.2	60.2
Ga	−0.85	−5.0	0	0	0	0	23.2	0	79.0	102.0
Cu	−1.05	−5.0	33.3	25.5	5.7	3.0	1.3	9.4	20.5	103.5
Ni	−1.09	−5.0	1.8	0.1	0	0	0	1.4	88.9	92.4
Fe	−0.52	−5.0	0	0	0	0	0	0	94.8	94.8
Pt	−0.68	−5.0	0	0	0	0	0	0.1	95.7	95.8
Ti	−1.21	−5.0	0	0	0	0	tr.	0	99.7	99.7

Figure 1.7: Electrochemical CO_2 reduction on metallic catalysts [17]

1.3. RESEARCH GOALS

Whilst copper has garnered a lot of interest in use as a catalyst for CO_2 towards multi-carbon products, there is lack of information pertaining to the combined use of copper catalysts in conjunction with gas diffusion electrodes. Additionally, traditional lab based catalysts syntheses though relevant for a mechanistic understanding, are not readily industrially applicable due to the lack of existing infrastructure. This study is done with the view of facilitating the transition of CO_2 electroreduction from a lab-scale technique to an industrially feasible technology.

The main objectives of this study are:

> *"Synthesising copper based electrocatalysts using an industrially relevant, scalable approach"*

> *"Investigating the activity/selectivity of selected electrocatalysts for CO_2 RR on gas diffusion electrodes"*

1.4. APPROACH

The synthesis of copper catalysts is performed using electrochemical methods. Varying currents were applied depending on the plating substrate to obtain different morphologies. Nanowires were also synthesized by templated electrodeposition of copper in track-etched polycarbonate templates (PCTE). The crystalline structure of the synthesised catalysts was determined using X-ray diffraction (XRD), the morphology using Scanning Electron Microscopy (SEM) and Energy Dispersive X-ray Spectroscopy (EDX).

The CO_2 experiments were carried out in a custom made gas diffusion cell. The liquid products were analysed off-line using high performance liquid chromatography (HPLC) and the gaseous products were analysed in-line using gas chromatography (GC). Cyclic voltammetry was used to characterise the electrochemical surface area (ECSA) of the catalysts. Amongst the different morphologies synthesised, one specific morphology was tested for its CO_2 RR performance.

1.5. REPORT OUTLINE

The report starts with a brief description of the context of the study and the research questions of interest in Chapter 1. This is followed by a discussion in Chapter 2 on the requisite theoretical background and the state of current research work in the field of CO_2 RR. A description of the experimental setup/process parameters, the product analysis tools, and the characterisation techniques used is given in Chapter 3. Chapter 4 deals with the approach taken for the various morphologies of catalysts synthesised. The CO_2 RR performance of the synthesised catalysts are discussed in Chapter 5. The report is concluded with an overarching conclusion of the work, and recommendations for future work on this project in chapter 6. After the conclusion of the main body of the report, a few appendices are added which consist of supporting information for the experimental work. App. A contains the calibration curves for the various gases observed during the reduction reaction, and App. B consists of the calibration data for the HPLC. Appendix C consists of data pertaining to the GDL and Appendix D consists of enlarged images of the different catalyst morphologies synthesised. Supplementary data for the CO_2 RR experiments is given Appendix E.

2

THEORETICAL BACKGROUND

This chapter deals with the requisite theoretical background needed to gain a more comprehensive understanding of the contents of this study. An overview of the CO_2 RR process, the reduction mechanism, working of the two different cell setups are mentioned alongside a discussion on the catalysts and why certain catalysts tend to favour the formation of a particular compound. The current standards in CO_2 RR across different parameters are also mentioned for benchmarking purposes and to facilitate a fair comparison between the results of this study and the current research standards.

2.1. CO_2 CONVERSION TECHNIQUES

Carbon Dioxide is a linear, non-polar, fully oxidised form of carbon that is extremely stable. A chemical conversion from this stable state requires an efficient electrocatalytic system that overcomes the sluggish kinetics of the reduction process. [18] Reduction of CO_2 into a more energetic product involves transfer of electrons to carbon thereby reducing its oxidation state. When these reactions are thermally driven, the process is known as hydrogenation. Reduction of CO_2 when driven by natural photosynthesis or bio-inspired catalysts is known as CO_2 fixation. [19]

The thermally activated chemical means of reduction by the Reverse water-gas shift reaction (2.1) or the methanation reaction (2.2) are usually run at high pressures and temperatures. The methanol synthesis reaction (2.3) which requires 100bar and 250°C for the methanol synthesis, has the mildest reaction conditions of the three mentioned reactions.

$$CO_2 + H_2 \longrightarrow \mathrm{CO} + \mathrm{H_2O} \tag{2.1}$$

$$CO + 3\,\mathrm{H_2} \longrightarrow \mathrm{CH_4} + \mathrm{H_2O} \tag{2.2}$$

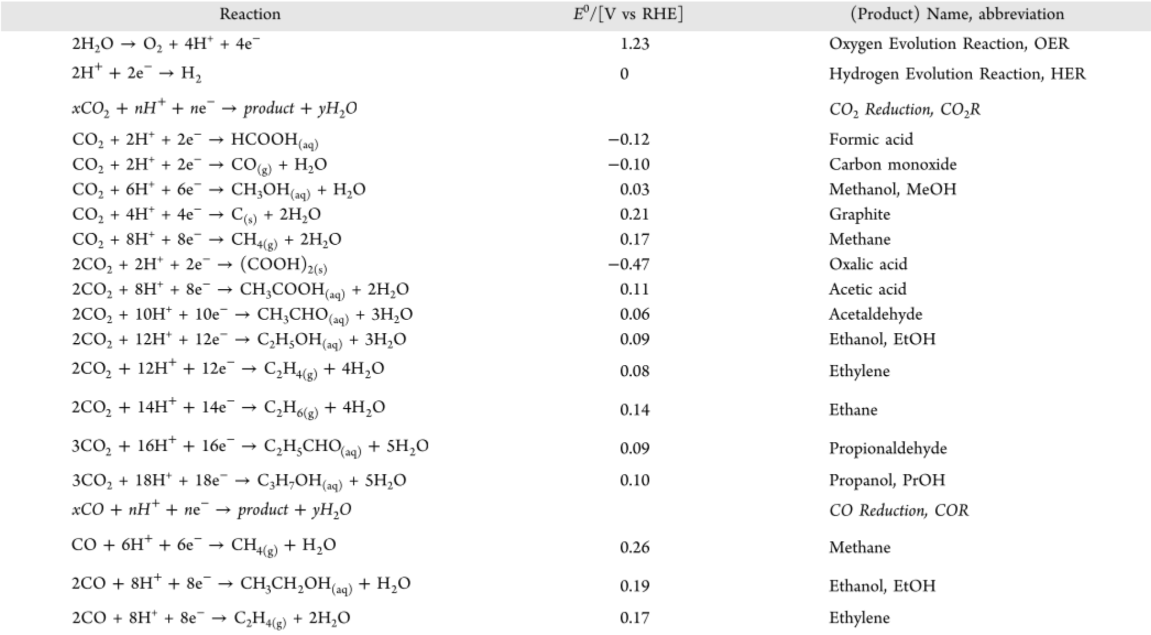

Reaction	E^0/[V vs RHE]	(Product) Name, abbreviation
$2H_2O \rightarrow O_2 + 4H^+ + 4e^-$	1.23	Oxygen Evolution Reaction, OER
$2H^+ + 2e^- \rightarrow H_2$	0	Hydrogen Evolution Reaction, HER
$xCO_2 + nH^+ + ne^- \rightarrow product + yH_2O$		*CO_2 Reduction, CO_2R*
$CO_2 + 2H^+ + 2e^- \rightarrow HCOOH_{(aq)}$	−0.12	Formic acid
$CO_2 + 2H^+ + 2e^- \rightarrow CO_{(g)} + H_2O$	−0.10	Carbon monoxide
$CO_2 + 6H^+ + 6e^- \rightarrow CH_3OH_{(aq)} + H_2O$	0.03	Methanol, MeOH
$CO_2 + 4H^+ + 4e^- \rightarrow C_{(s)} + 2H_2O$	0.21	Graphite
$CO_2 + 8H^+ + 8e^- \rightarrow CH_{4(g)} + 2H_2O$	0.17	Methane
$2CO_2 + 2H^+ + 2e^- \rightarrow (COOH)_{2(s)}$	−0.47	Oxalic acid
$2CO_2 + 8H^+ + 8e^- \rightarrow CH_3COOH_{(aq)} + 2H_2O$	0.11	Acetic acid
$2CO_2 + 10H^+ + 10e^- \rightarrow CH_3CHO_{(aq)} + 3H_2O$	0.06	Acetaldehyde
$2CO_2 + 12H^+ + 12e^- \rightarrow C_2H_5OH_{(aq)} + 3H_2O$	0.09	Ethanol, EtOH
$2CO_2 + 12H^+ + 12e^- \rightarrow C_2H_{4(g)} + 4H_2O$	0.08	Ethylene
$2CO_2 + 14H^+ + 14e^- \rightarrow C_2H_{6(g)} + 4H_2O$	0.14	Ethane
$3CO_2 + 16H^+ + 16e^- \rightarrow C_2H_5CHO_{(aq)} + 5H_2O$	0.09	Propionaldehyde
$3CO_2 + 18H^+ + 18e^- \rightarrow C_3H_7OH_{(aq)} + 5H_2O$	0.10	Propanol, PrOH
$xCO + nH^+ + ne^- \rightarrow product + yH_2O$		*CO Reduction, COR*
$CO + 6H^+ + 6e^- \rightarrow CH_{4(g)} + H_2O$	0.26	Methane
$2CO + 8H^+ + 8e^- \rightarrow CH_3CH_2OH_{(aq)} + H_2O$	0.19	Ethanol, EtOH
$2CO + 8H^+ + 8e^- \rightarrow C_2H_{4(g)} + 2H_2O$	0.17	Ethylene

Figure 2.1: Electrochemical CO_2 Conversion Reactions with Equilibrium Potentials[19]

$$CO + 2\,H_2 \longrightarrow CH_3OH \tag{2.3}$$

The hydrogen that these reactions require is usually obtained by the electrochemical splitting of water, driven by renewable sources of energy. The reduction of water is then proceeded by the thermal hydrogenation of CO_2 to the desired reduction products by employing appropriate experimental conditions. [19]

2.2. CARBON DIOXIDE ELECTROREDUCTION

The conversion of CO_2 can instead be driven completely by electrochemical means. The direct electrochemical reduction is advantageous compared to thermal hydrogenation of CO_2 as it combines the electrochemical water splitting and the thermal hydrogenation in one step. These electrochemical reactions run at near room temperatures/pressures. The electrochemical method also provides a wider range of reduction products that can be synthesised. [19] Fig. 2.1 depicts the various products that could be theoretically obtained by the electrochemical reduction of CO_2.

$$kCO_2 + n(H^+ + e^-) \longrightarrow P + mH_2O \tag{2.4}$$

The electrochemical reduction reaction of carbon dioxide to product, 'P', is depicted by the equation 2.4. The coefficient 'm' and 'n' for some common reduction products are shown in Fig. 2.2. The cathodic half-cell reaction is dependent on the catalyst used and the potential applied. These reactions are also actively competing with the hydrogen evolution reaction (HER), eq.2.5, which takes place at lower overpotentials.

$$2H^+ + 2\,e^- \longrightarrow H_2 \tag{2.5}$$

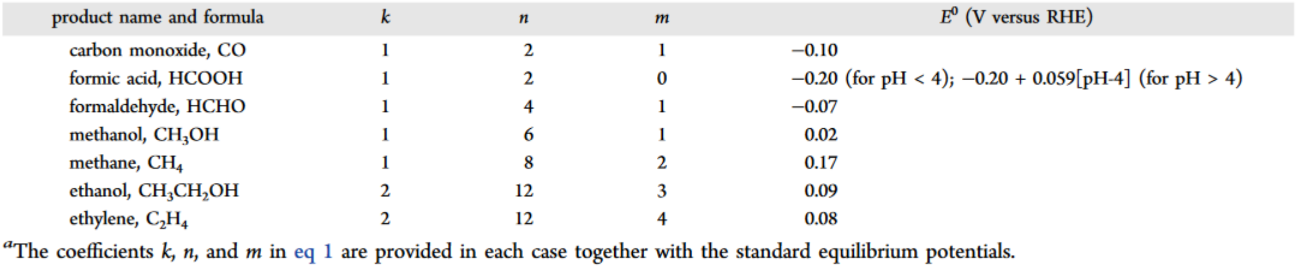

product name and formula	k	n	m	E^0 (V versus RHE)
carbon monoxide, CO	1	2	1	−0.10
formic acid, HCOOH	1	2	0	−0.20 (for pH < 4); −0.20 + 0.059[pH-4] (for pH > 4)
formaldehyde, HCHO	1	4	1	−0.07
methanol, CH_3OH	1	6	1	0.02
methane, CH_4	1	8	2	0.17
ethanol, CH_3CH_2OH	2	12	3	0.09
ethylene, C_2H_4	2	12	4	0.08

[a]The coefficients k, n, and m in eq 1 are provided in each case together with the standard equilibrium potentials.

Figure 2.2: Main Products of the electrochemical reduction of CO_2 [20]

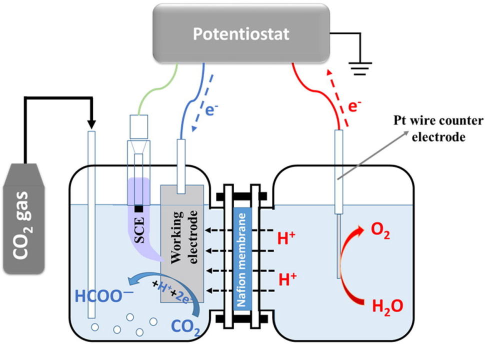

Figure 2.3: Schematic of an aqueous media H-cell electrochemical setup for Co_2 reduction [22]

In the anodic half, the oxygen evolution reaction OER takes place. It's a vital component of the CO_2 RR system as it provides the hydrogen ions required at the cathode for the subsequent CO_2 RR.

$$2H_2O \longrightarrow O_2 + 4\,H^+ + 4\,e^- \tag{2.6}$$

2.2.1. H-CELL CONFIGURATION

CO_2 reduction has been conventionally carried out in aqueous media in an H-cell setup. In this setup, a three electrode, two chamber configuration is employed as shown in Fig. 2.3. The anodic and the cathodic halves are separated by a proton conducting membrane, which allows for the migration of the hydrogen ions but prevents the products on the cathode to migrate to the anode. The CO_2 saturated electrolyte is the carbon source for the subsequent reduction reactions and this presents an inherent limitation of this system due to the low solubility of CO_2 (33 mM) in conventional aqueous solvents. This limits the obtainable current densities to 35 mA cm^{-2}. For industrial feasibility of CO_2 RR from an economic standpoint, future electrolysers will need to demonstrate long term stability (>20,000 hours) at current densities of >200 mA cm^{-2}. [13] Owing to the industrial requirements of higher current densities and the inherent limitations of the H-cell method, there has been a change in cell concept to move towards vapor-based, gas diffusion layer based systems. About 95% of the current studies and catalytic materials developed have been tested and characterised in this classical H-cell configuration where the current densities are limited. Further studies need to be carried out to ascertain if the understanding developed using the H-cell system design is representative of the gas diffusion layer based system as the CO_2 RR process is highly sensitive to changes in the reaction environment . [13] [21]

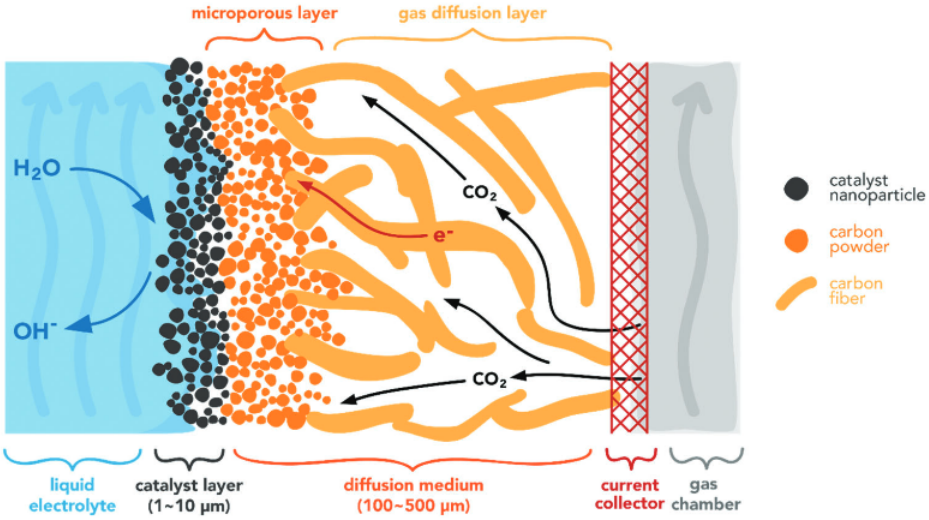

Figure 2.4: Schematic of a gas diffusion electrode based CO_2 reduction system [21]

2.2.2. GAS DIFFUSION ELECTRODES

As mentioned in the previous sections, the limitations of the H-cell configurations with regards to the low current densities can be overcome by employing a vapor fed, GDL based catalytic system. A schematic of a gas diffusion based CO_2 RR system is shown in Fig. 2.4. In this configuration the CO_2 reacts on the catalyst surface in gaseous form, and the reduction reaction is hypothesised to take place at the triple point intersection of the gas and the electrolyte on the catalyst surface. The CO_2 flows through a diffusion media before reaching the catalyst layer. The diffusion media is typically comprised of a gas diffusion layer(GDL) and may or may not include a microporous layer. The gas diffusion layer is usually a carbon fibre mesh which provides the CO_2 a pathway for homogeneous diffusion to the catalyst layer. It provides mechanical support to the catalyst layer, and also an electrically conductive pathway for the electrons to flow to the catalyst layer. The microporous layer usually consists of carbon black nanoparticles and polytetrafluoruethene(PTFE). This layer helps form the gas-liquid interface between the PTFE coating whose hydrophobic nature prevents the fouling of the diffusion media thereby preventing diffusion limitations of CO_2.[13][23]

Using a GDL based CO_2 RR setup also helps overcome another limitation of the H-cell configuration wherein concentration gradients were established on rough nanostructured catalysts. Nanostructured catalysts, in the aqueous media acted as quasi-planar catalysts as CO_2 was severely depleted at the innermost surfaces. In the GDL based system the CO_2 flows from the innermost surfaces of the catalyst to the outermost surfaces (facing the electrolyte), hence this mass transport limitation is overcome and a larger electrochemically active surface (ECSA) is available for the reaction. This is possible due to all the surface of the catalyst having access to CO_2 with shorter diffusion pathways. This higher ECSA results in lower overpotentials in comparison to the H-cell configuration. It also highlights the difficulties in translating the understanding acquired from H-cell based cells to vapor-fed cells.[23]

2.2.3. REACTION MECHANISM

The exact reaction mechanism and key reaction intermediates are still a matter of debate amongst the various research groups.[24] [25]. Fig. 2.5 shows a schematic representing the different pathways hypothesised for the formation of ethylene, methane and ethanol. Most models focus on CO as the starting point rather than CO_2 as it is known that CO_2 is first converted to CO before further reduction to >2e$^-$ products. Additionally the electroreduction of CO results in the same product distribution as that of CO_2, which also suggests that CO and CO_2 share the same reaction pathway with the reduction to CO being the first step.[26] Following the formation of * CO, either a C-C coupling could take place leading to the formation of ethylene and ethanol or a protonation resulting in the formation of methane. The dimerisation on Cu(100) is preferred as it occurs at lower overpotentials and the fact that it doesn't share any reaction pathway with methane enhances the selectivity. On the Cu (111) facets, a higher overpotential pathway is observed likely through *CHO intermediate. *CHO is also an intermediate for the production of CH_4, hence when the reduction takes place on Cu (111) facets, both methane and ethylene are observed.

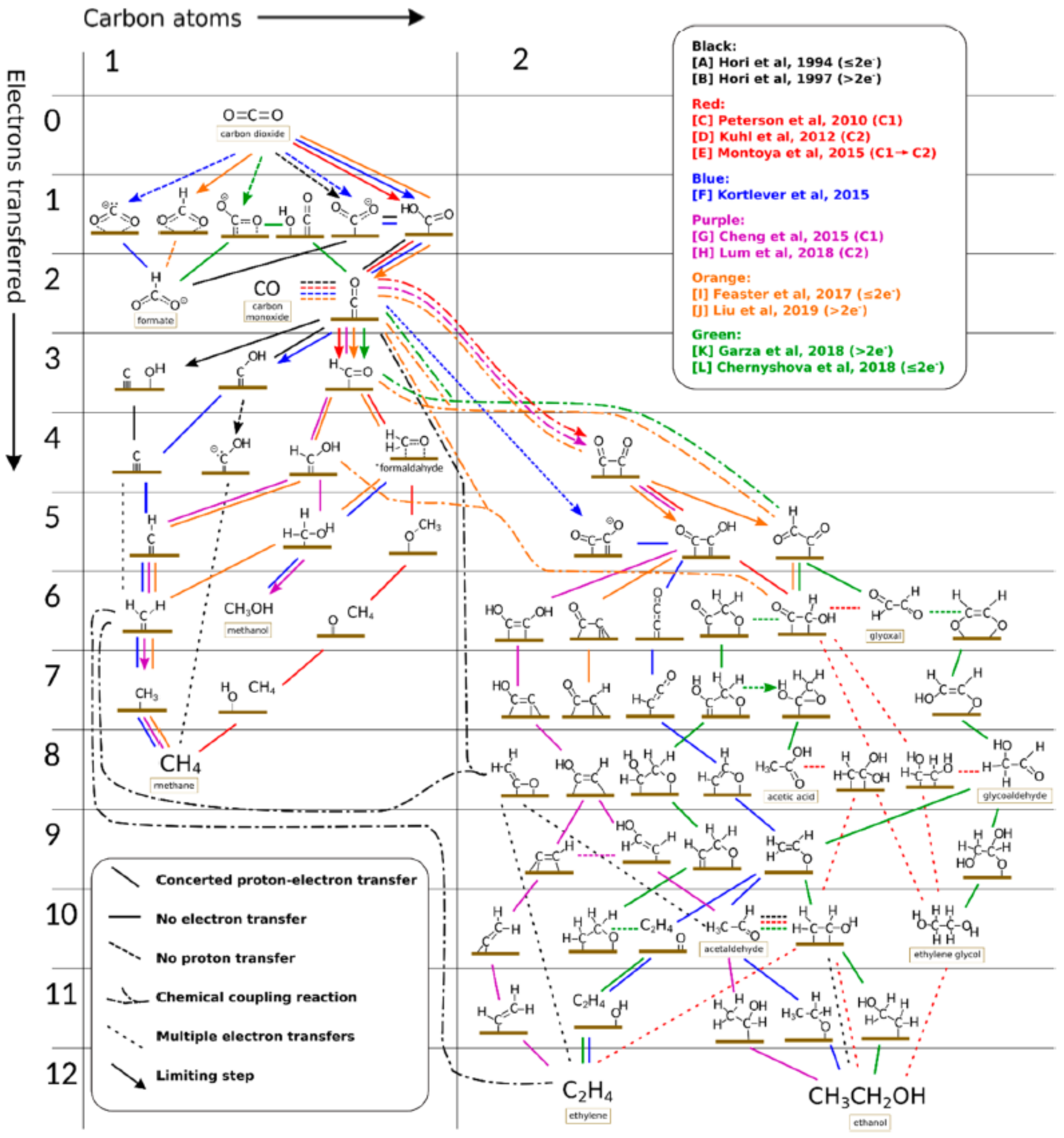
Carbon atoms
1
2
Electrons transferred
0
1
2
3
4
5
6
7
8
9
10
11
12
O=C=O
carbon dioxide
CO
carbon monoxide
formate
formaldehyde
CH3OH
methanol
CH4
methane
glyoxal
acetic acid
glycoaldehyde
acetaldehyde
ethylene glycol
C2H4
ethylene
CH3CH2OH
ethanol
Black:
[A] Hori et al, 1994 (≤2e-)
[B] Hori et al, 1997 (>2e-)
Red:
[C] Peterson et al, 2010 (C1)
[D] Kuhl et al, 2012 (C2)
[E] Montoya et al, 2015 (C1→C2)
Blue:
[F] Kortlever et al, 2015
Purple:
[G] Cheng et al, 2015 (C1)
[H] Lum et al, 2018 (C2)
Orange:
[I] Feaster et al, 2017 (≤2e-)
[J] Liu et al, 2019 (>2e-)
Green:
[K] Garza et al, 2018 (>2e-)
[L] Chernyshova et al, 2018 (≤2e-)
Concerted proton-electron transfer
No electron transfer
No proton transfer
Chemical coupling reaction
Multiple electron transfers
Limiting step

Figure 2.5: Mechanistic Pathways for CO_2 electroreduction to CH_4 and C_2H_4 [19]

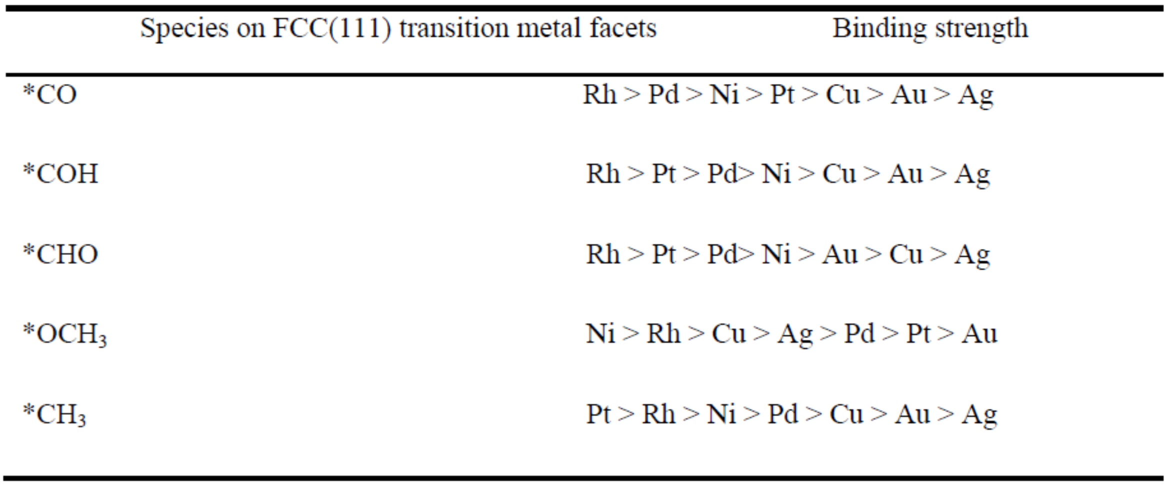

Species on FCC(111) transition metal facets	Binding strength
*CO	Rh > Pd > Ni > Pt > Cu > Au > Ag
*COH	Rh > Pt > Pd> Ni > Cu > Au > Ag
*CHO	Rh > Pt > Pd> Ni > Au > Cu > Ag
$*OCH_3$	Ni > Rh > Cu > Ag > Pd > Pt > Au
$*CH_3$	Pt > Rh > Ni > Pd > Cu > Au > Ag

Figure 2.6: Binding Strength of Reaction Intermediates on FCC(111) facet of Transition Metals [29]

2.3. CATALYSTS

The electrocatalytic reduction of CO_2 can be driven towards various different products by applying different equilibrium potentials as is shown in Fig. 2.1. The electrons required for some of the common reduction products are depicted in Fig. 2.2. In practical applications though, the potentials required to drive these reactions towards a particular product are much more negative than the equilibrium potential values due to the competition with the HER. The number of electrons required to form certain products are dependent on the number of reaction intermediates and thus the activation energy of each intermediate has to be overcome to form the final product. Therefore, though the equilibrium potential for a product might be small, the actual potential needed is much higher due to the formation of the different intermediates and overcoming their activation energy barriers. The required overpotentials are also strongly material dependent as the binding energy of reaction intermediates and their adsorbtion on the surface of the catalyst is an important factor in determining the final reduction product.[27] [28] [17]

Hori et.al [17] carried out CO_2 RR reaction on metal electrodes, Fig. 1.7, and found that several transition metals could reduce CO_2 to various different products. From this seminal study, it was also found that copper was one of the few catalysts that could reduce CO_2 to ethylene and liquid compounds like ethanol and Propanol. The multi-step, multi-electron CO_2 reduction process proceeds with the formation of multiple adsorbed intermediates, most notably CO. As mentioned earlier, the products formed are strongly dependent on the binding strength of the intermediates(CO,COH,CHO,CH_3) on the catalyst. The intermediates adsorb onto the catalyst active sites, and the product selectivity is determined by the binding strength of the intermediates on the catalyst. For instance the catalysts that show a high propensity towards the formation of CO such as Au, Ag, Zn weakly bind with CO, thereby no subsequent reduction is possible. Metals such as Pt, Ti, Fe, on the other hand bind too strongly to the metal surface, thereby limiting CO desorbtion and blocking the active catalyst surface in the process, suppressing CO_2 RR and promoting HER. In contrast, as is evident from Fig. 2.6, Cu lies in the intermediate binding strength regime, and therefore promotes CO reduction to mulit-step compounds as is seen in Fig. 1.7.[28] [29]. Catalytic activity is not only material dependent, but also morphology dependent. This can also be related to the difference in binding energies of intermediates at different crystal facets that are exposed. Presence of more active sites (low coordination sites, edge and corner) in nanostructured materials also enhance the catalytic activity in comparison to bulk metal catalysts.

In addition, nanostructured materials with high roughness factors possess higher ECSA in the same geometric areas.[29] Fig. 2.7 depicts the effect that different crystal orientations have on the product distribution obtained. It also depicts the influence of under-coordinated sites on stepped Cu single crystal surfaces. The presence of (111) or (110) steps on Cu (100) surfaces vastly changed the faradaic efficiencies obtained and made the reduction process more selective towards C-C coupling.

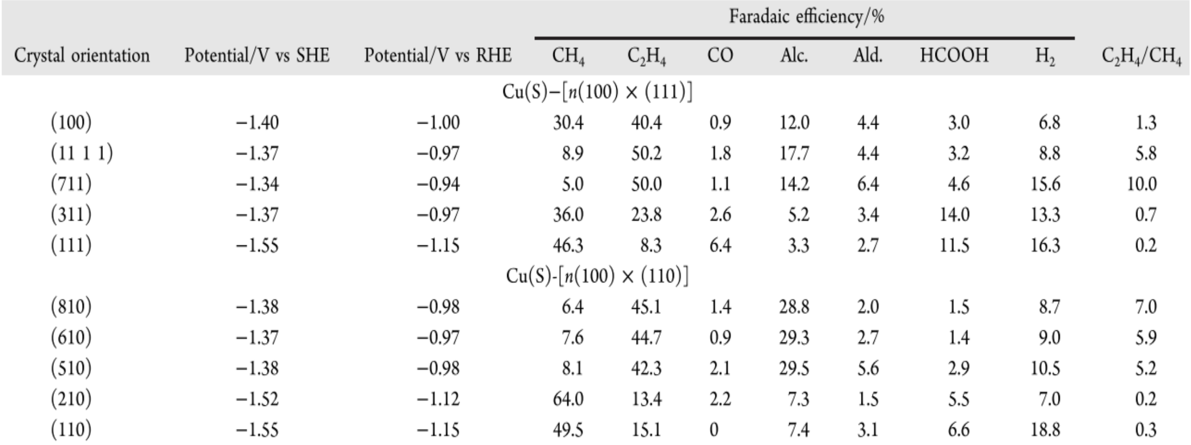

			Faradaic efficiency/%							
Crystal orientation	Potential/V vs SHE	Potential/V vs RHE	CH_4	C_2H_4	CO	Alc.	Ald.	HCOOH	H_2	C_2H_4/CH_4
			Cu(S)–[n(100) × (111)]							
(100)	−1.40	−1.00	30.4	40.4	0.9	12.0	4.4	3.0	6.8	1.3
(11 1 1)	−1.37	−0.97	8.9	50.2	1.8	17.7	4.4	3.2	8.8	5.8
(711)	−1.34	−0.94	5.0	50.0	1.1	14.2	6.4	4.6	15.6	10.0
(311)	−1.37	−0.97	36.0	23.8	2.6	5.2	3.4	14.0	13.3	0.7
(111)	−1.55	−1.15	46.3	8.3	6.4	3.3	2.7	11.5	16.3	0.2
			Cu(S)-[n(100) × (110)]							
(810)	−1.38	−0.98	6.4	45.1	1.4	28.8	2.0	1.5	8.7	7.0
(610)	−1.37	−0.97	7.6	44.7	0.9	29.3	2.7	1.4	9.0	5.9
(510)	−1.38	−0.98	8.1	42.3	2.1	29.5	5.6	2.9	10.5	5.2
(210)	−1.52	−1.12	64.0	13.4	2.2	7.3	1.5	5.5	7.0	0.2
(110)	−1.55	−1.15	49.5	15.1	0	7.4	3.1	6.6	18.8	0.3

Figure 2.7: Product distribution in CO_2 Reduction on copper single crystal electrodes [19]

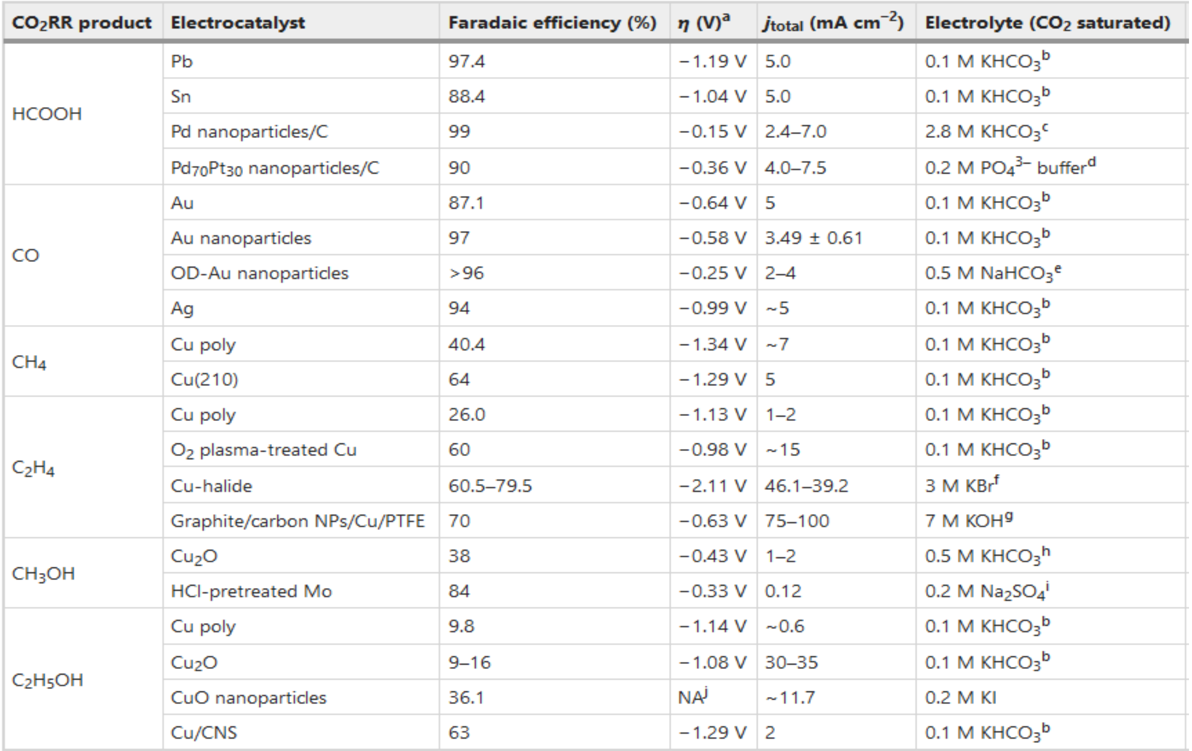

CO_2RR product	Electrocatalyst	Faradaic efficiency (%)	η (V)^a	j_{total} (mA cm^{-2})	Electrolyte (CO_2 saturated)
HCOOH	Pb	97.4	−1.19 V	5.0	0.1 M $KHCO_3$^{b}
	Sn	88.4	−1.04 V	5.0	0.1 M $KHCO_3$^{b}
	Pd nanoparticles/C	99	−0.15 V	2.4–7.0	2.8 M $KHCO_3$^{c}
	$Pd_{70}Pt_{30}$ nanoparticles/C	90	−0.36 V	4.0–7.5	0.2 M PO_4^{3-} buffer^d
CO	Au	87.1	−0.64 V	5	0.1 M $KHCO_3$^{b}
	Au nanoparticles	97	−0.58 V	3.49 ± 0.61	0.1 M $KHCO_3$^{b}
	OD-Au nanoparticles	>96	−0.25 V	2–4	0.5 M $NaHCO_3$^{e}
	Ag	94	−0.99 V	~5	0.1 M $KHCO_3$^{b}
CH_4	Cu poly	40.4	−1.34 V	~7	0.1 M $KHCO_3$^{b}
	Cu(210)	64	−1.29 V	5	0.1 M $KHCO_3$^{b}
C_2H_4	Cu poly	26.0	−1.13 V	1–2	0.1 M $KHCO_3$^{b}
	O_2 plasma-treated Cu	60	−0.98 V	~15	0.1 M $KHCO_3$^{b}
	Cu-halide	60.5–79.5	−2.11 V	46.1–39.2	3 M KBr^f
	Graphite/carbon NPs/Cu/PTFE	70	−0.63 V	75–100	7 M KOH^g
CH_3OH	Cu_2O	38	−0.43 V	1–2	0.5 M $KHCO_3$^{h}
	HCl-pretreated Mo	84	−0.33 V	0.12	0.2 M Na_2SO_4^{i}
C_2H_5OH	Cu poly	9.8	−1.14 V	~0.6	0.1 M $KHCO_3$^{b}
	Cu_2O	9–16	−1.08 V	30–35	0.1 M $KHCO_3$^{b}
	CuO nanoparticles	36.1	NA^j	~11.7	0.2 M KI
	Cu/CNS	63	−1.29 V	2	0.1 M $KHCO_3$^{b}

Figure 2.8: Highly Selective/active metal and metal-derived electrocatalysts for synthesis of specific CO_2 RR products [14]. *The overpotential values are mentioned versus RHE*

2.3.1. COPPER ELECTROCATALYSTS

As was laid out in the previous sections, for CO_2 RR towards multi-carbon/liquid products, copper is an ideal catalyst due to its moderate binding strength with key reaction intermediates. To better understand the CO_2 RR products, it is essential to understand the reaction mechanisms, the key intermediates and their interactions with different crystalline facets of the catalysts.

Copper is known to produce a variety of C_1, C_2, and C_3 compounds, the selectivity of which is heavily dependent on the surface morphology of Cu. Amongst the low index planes, the more open Cu(100) surface exhibits greater selectivity for C-C coupling than the close packed Cu(111). CH_4 formation is found to be more predominant on the Cu(111) face and C_2H_4 is preferred on the Cu(211) facets. [26] It is also observed that ethylene can be formed via two distinct pathways, a high overpotential pathway taking place on the Cu(111) facet which also shares a reaction intermediate with methane, and a lower overpotential pathway on Cu(100), which doesn't yield C_1 products. [14] For enhanced selectivity towards ethylene an ideal copper-based catalyst would consist of a Cu(100) basal plane with a large number of undercoordinated sites, and a high electrochemically active surface area.

2.3.2. ELECTROCATALYST SYNTHESIS

Compared to the catalysts for the H-cell configuration, GDE based electrocatalysts pose specific challenges with regards to the porosity of the catalyst layer. Referring to Fig. 2.4, it is seen that the reduction reaction takes place at the triple point interface on the catalyst surface where the electrolyte, and the reactant gas (CO_2) interact. If the catalyst layer (black spherical particles) consisted of a thick metallic sheet, it would act as a barrier for the diffusion of the CO_2 towards the electrolyte. Therefore it is essential for the catalyst layer to be porous, thereby limiting synthesis approaches for the electrocatalyst. The seminal work of *Hori et al.*[17] was carried out in the H-cell configuration by employing solid metallic electrodes. Due to the established limitations of the GDE system, this approach cannot be employed for the purposes of this study.

Conventionally for GDE, a multi-step process consisting of wet chemically synthesizing the catalyst particles, followed by concentrating and spray coating is used.[30] [11] Another approach includes using copper gauze substrates and then thermo-mechanically treating them in specific reaction environments to alter the crystal structure/chemical composition. This is followed by spray coating a hydrophobic coating (Teflon) to prevent fouling of the catalyst.[31] Some research groups use commercially available metallic-powders to make a dispersion with Nafion and isopropanol and then deposit onto carbon based gas diffusion layers.[32] In the current research standard CO_2 RR experiments done by *Burdyny et.al.*,[33] the catalysts were synthesized by a similar approach using commercial copper particles in a dispersion of copper/Nafion/isopropanol and spray coating onto the carbon cloth.

These synthesis techniques, whilst relevant for a scientific understanding of the CO_2 RR process, pose challenges with regards to scalabilty, catalyst synthesis times, and integration into current industrial infrastructure. In this study, electrodeposition is used to synthesize the electrocatalysts, as it is a technique which is industrially established for large scale components, and can be integrated within the current infrastructure. Additionally catalysts synthesized by electrodeposition require considerably less time for the synthesis of the catalysts. The synthesis approach is discussed in more detail in Chapters 3 & 4.

3

EXPERIMENTAL METHOD

This chapter deals with the experimental setup, the electrochemical parameters and characterisation techniques used over the course of the study. A description of the different components of the experimental setup with their function is mentioned. This is followed by a description of the analysis tools used to determine the products of the CO_2 RR. A brief overview of the different techniques used to characterise the catalysts before and after the reduction reaction is also mentioned.

3.1. ELECTROREDUCTION EXPERIMENTS

All the electrochemical experiments were carried out in an electrochemical cell consisting of three electrodes, and two compartments - cathodic (working electrode) and anodic (counter electrode). Fig. 3.1 depicts a schematic of the electrochemical cell used and Fig. 3.2 shows an image of the actual cell used. The two compartments were separated by a proton conducting membrane (Nafion 117), which only allowed for the diffusion of hydrogen ions from the anode to the cathode. A satd. Ag/AgCl electrode, placed in the cathodic chamber, was used as the reference to measure the potential at the working electrode. A platinum mesh was used as the counter electrode (anode) while the working electrode (cathode) was the GDL supported catalyst being tested. The working electrode had an area of 6.25 cm^2 (2.5cm × 2.5cm). Two external electrolyte (1M KOH) baths supplied the cathodic and anodic compartments with the electrolyte at a constant bulk temperature. The electrolyte baths supplied the electrolyte to the electrochemical cell using a peristaltic pump. Fig. 3.3 depicts the entire CO_2 RR setup with the various different components.

The bulk temperature of the electrolyte was kept constant at 20°C using a *Julabo CF-30* heating/cooling circulator. The total volume of electrolyte flowing in the working electrode system was kept at 60ml, with the volume of the working electrode compartment inside the cell being 20ml. The electrolyte was pre-saturated with CO_2 before the start of the experiment (pH = 7.6 after saturation with CO_2). This pre-saturation was done to have constant starting conditions of the reaction, as on exposure to CO_2 the pH of the electrolyte rapidly decreased from a value of 14 at the unsaturated state to 7.6 at its saturated state. The decrease in pH could be attributed to the dissolution of CO_2 in the electrolyte and the formation of carbonate through a chemical

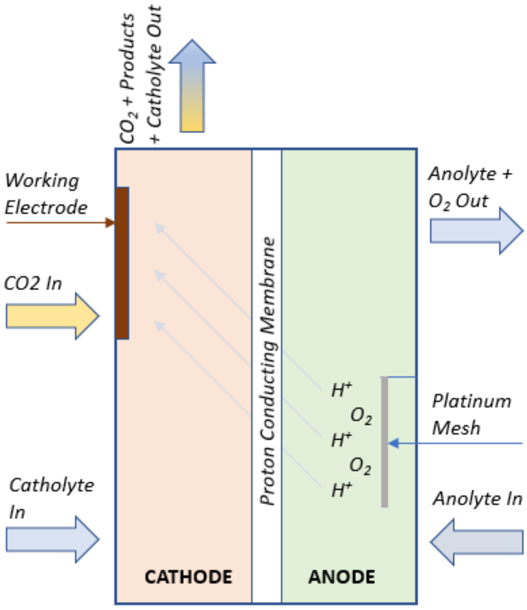
CO$_2$ + Products
+ Catholyte Out
Working Electrode
CO2 In
Catholyte In
Proton Conducting Membrane
CATHODE
ANODE
H$^+$
O$_2$
H$^+$
O$_2$
H$^+$
Anolyte + O$_2$ Out
Platinum Mesh
Anolyte In

Figure 3.1: Schematic of the electrochemical cell used for the CO$_2$ RR experiments

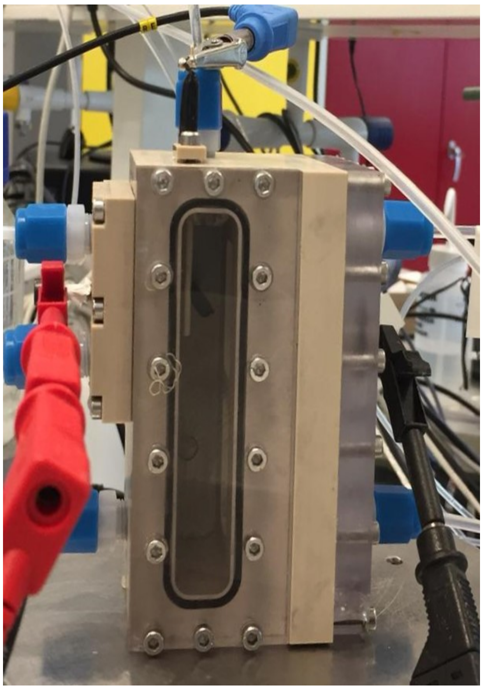

Figure 3.2: Electrochemical cell used for the CO$_2$ RR experiments

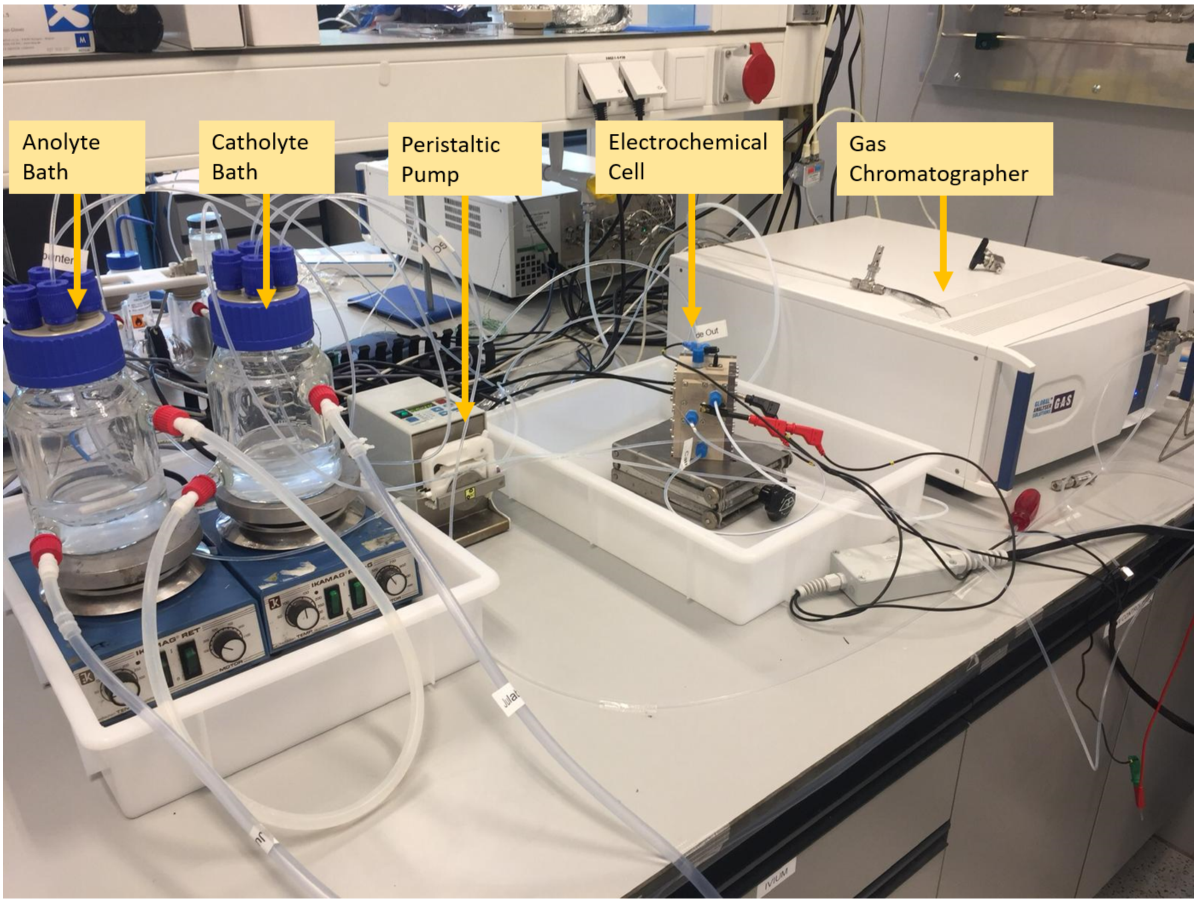
Anolyte Bath
Catholyte Bath
Peristaltic Pump
Electrochemical Cell
Gas Chromatographer

Figure 3.3: Setup for the CO$_2$ RR experiments

reaction (Eq. 3.1 & 3.2) between KOH and CO_2.[34]

$$KOH + CO_2 \longrightarrow KHCO_3 \tag{3.1}$$

$$KHCO_3 + CO_2 \longrightarrow KHCO_3 \tag{3.2}$$

This was not conducive from the perspective of reporducibility of the experiments because of the difference in the ionic conductivity of carbonate. Different conductivity would imply different ionic migration rates and therefore alter the kinetics of the reaction as well. Also, carrying out experiments at different pH values would result in challenges pertaining to normalizing the potential values to the RHE scale. A 20ml/min flow of nitrogen was supplied to the catholyte bath. It was used to normalise the obtained GC data to volumetric flows (App. A). Carbon Dioxide at a flow rate of 10ml/min was continuously supplied to the cathodic chamber of the electrochemical cell. The CO_2 diffused through the GDL and the microporous layer before reaching the catalyst surface. The anolyte bath was also bubbled with CO_2. The flow rates of the gases were controlled using *Bronkhorst El-Flow Prestige* mass flow controllers. The flow controllers were calibrated for 4 bars of pressure. Potentiostatic experiments were carried out via an *Autolab PGSTAT302N* Potentiostat to evaluate the CO_2 RR performance. The current data was logged every second, and was used in conjunction with the data from the product analysis tools to calculate the faradaic efficiencies for different applied potentials.

The Potentiostatic experiments were conducted in the potential regime of -1.8 V vs -2.3 V vs Ag/AgCl. The upper limit of -2.3 V vs Ag/AgCl was established due to no product formation at higher potentials and similarly at lower potentials than -1.8 V vs Ag/AgCl no ethylene formation was evidenced. The potential data observed was converted to the RHE scale using Eq. 3.8, this was done to facilitate easier comparison with data reported in literature and to also remove the pH dependency. A pH value of 7.6 was used to convert the potentials observed vs Ag/AgCl. The experiments were carried out for a time period of 1 hour, and for the case of the pulsed electrolysis approach, experiments were carried out for 15 hours.

CALCULATION OF FARADAIC EFFICIENCY

When multiple reactions occur simultaneously at the surface of an electrode, the fraction of the total current going to a specific reaction over the course of the entire reaction is expressed using the term Faradaic Efficiency FE% or Current Efficiency.[35] Over the course of this study, the faradaic efficiency of the gaseous products was measured every 5.5 mins, and the Faradaic Efficiency of the liquid products was measured once at the end of the reaction.

The fundamental expression for the faradaic efficiency for a particular reaction product ’x’ is:

$$FE_x\% = \frac{Q_x \times 100}{Q_{total}} \tag{3.3}$$

where Q_{total} represents the total charge, and, Q_x represents the fractional charge.
The total charge (Q_{total}) is calculated by integrating the measured current over the time of measurement.

$$Q_{total} = \int_0^t i\,dt \tag{3.4}$$

The fractional charge (Q_x) towards a particular reaction product is calculated using the expression in eq. 3.5 derived from faraday laws of electrolysis,

$$Q_x = n_x \times z \times F \tag{3.5}$$

where 'n$_x$' is the number of mols of product 'x', which is calculated using the data obtained from the GC/HPLC; 'z' is the number of electrons required for the formation of product 'x'(values of 'z' for some common products are mentioned in Fig. 2.1); and 'F' is Faraday's Constant (*96485.33 C mol^{-1}*).

Substituting Eq. 3.4 and Eq. 3.5 in Eq. 3.3 gives us the expression used to calculate the Faradaic Efficiency.

$$FE_x\% = \frac{n_x \times z \times F \times 100}{\int_0^t i\,dt} \tag{3.6}$$

REVERSIBLE HYDROGEN ELECTRODE

Potentials in electrochemistry are reported versus a reference electrode. For this study, the potentials were applied with respect to a Ag/AgCl electrode. The most commonly used reference standard is the standard hydrogen electrode SHE. However the potential values reported versus SHE and Ag/AgCl are pH dependent. In order to remove the pH dependency, a new reference called reversible hydrogen electrode RHE is used. [36] The potentials obtained versus Ag/AgCl are converted to the new reference standard of RHE using the Eq. 3.8.

$$E_{\mathrm{SHE}} = E_{\mathrm{Ag/AgCl}} + E^0{}_{\mathrm{Ag/AgCl}} \tag{3.7}$$

where $E^0{}_{\mathrm{Ag/AgCl}} = 0.1976$ V at 25°C and $E_{\mathrm{Ag/AgCl}}$ is the applied potential. All the potentials in the study hereon, are converted to RHE unless explicitly specified.

$$E_{\mathrm{RHE}} = E_{\mathrm{SHE}} + .0591 \times pH \tag{3.8}$$

3.2. CATALYST SYNTHESIS

The catalysts were synthesized by electrodepositing copper from a copper sulfate bath onto a carbon cloth. By changing the deposition parameters, time & current densities, different morphologies of the catalyst were obtained. The influence of the parameters and the different structures obtained are discussed in Ch. 4. The as-synthesized catalysts were then used for the electrocatalytic experiments.

Fig. 3.4 schematically represents the electrodeposition setup, whereas Fig. 3.5 shows the actual setup. The setup consists of a stainless steel back contact on which a carbon GDL is placed. The stainless steel back contact and the GDL are then housed inside a PEEK holder (Fig. 3.6), which exposes only the front face of the GDL to the electrolyte. This makes sure that the deposition takes place only on the front face of the GDL and protects the back contact from any deposition. O-rings are used between the PEEK housing and the GDL to ensure a leak-proof seal thereby preventing any electrolyte leakage inside the holder. The carbon GDL in the holder is the surface on which the deposition of copper takes place. An area of 6.25 cm^2 (2.5 cm × 2.5 cm) was exposed to the electrolyte, to be compatible with the CO_2 RR setup shown in Fig. 3.5. A platinated titanium

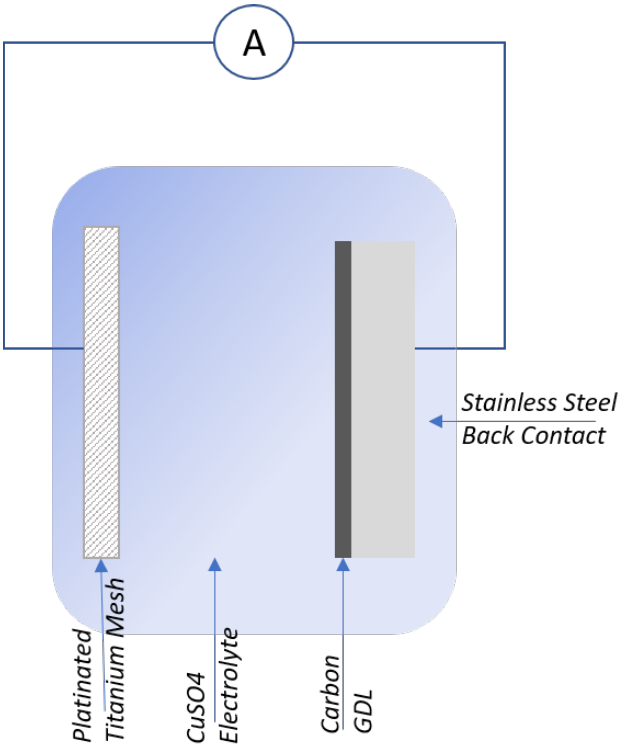

Figure 3.4: Schematic of the electrodeposition setup

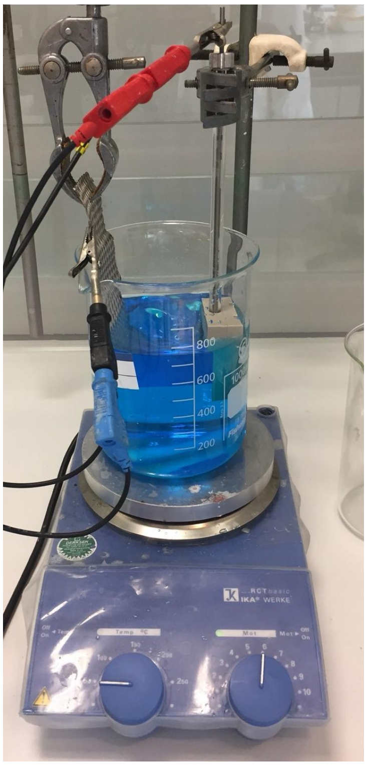

Figure 3.5: Electrodeposition setup for the catalyst synthesis

mesh is used as the counter electrode. On applying cathodic current to the working electrode, the copper ions in the electrolyte are reduced on the exposed surface of the working electrode. The duration of the experiment and the applied current density determine the structure formed. The electrolyte used for all the experiments had a copper concentration of 24.94 g/l. The deposition was done at room temperature and the electrolyte was constantly stirred at 600rpm using a magnetic stirrer. All the electrodeposition experiments were carried out using an Autolab PGSTAT302N.

To calculate the loading of the catalyst, Eq. 3.9 is used, which is derived from Faraday's laws of electrolysis. Here, 'M' is the molar mass of Copper - 63.546g/mol and, 'm' is the mass of copper deposited.

$$Q = \frac{m_{\text{Cu}} \times z \times F}{M_{\text{Cu}}} \tag{3.9}$$

For the synthesis of the catalysts a constant current, 'I' is applied for a time, 't', and therefore the total charge transferred can be calculated using Eq. 3.10.

$$Q = I \times t \tag{3.10}$$

Combining Eq. 3.10 and Eq. 3.9, and solving for 'm' gives us

$$m_{\text{Cu}} = \frac{M_{\text{Cu}} \times I \times t}{z \times F} \tag{3.11}$$

The value of 'z', the number of electrons transferred over the reduction reaction is 2, and follows from Eq. 3.12

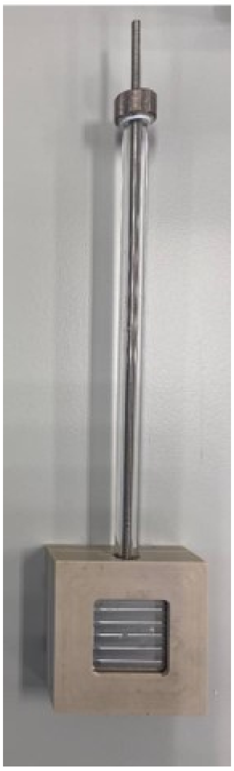

Figure 3.6: Electrodeposition holder

$$Cu^{2+}(aq) + 2\,e^{-} \longrightarrow Cu(s) \tag{3.12}$$

3.3. PRODUCT ANALYSIS TECHNIQUES

During the course of the CO_2 RR process, both gaseous and liquid products were formed. The gaseous products were analysed in-line every 5.5 minutes using a gas chromatographer(GC) and the liquid products were analysed at the end of the reaction using a high performance liquid chromatographer (HPLC).

3.3.1. GAS CHROMATOGRAHY (GC)

Gas Chromatography in conjunction with specific detectors is a separation/analytical tool used to quantitatively classify volatile compounds. GCs primarily work upon the difference of boiling point/vapour pressure and polarity of the analytes. The product mixture (CO_2 RR Products + Nitrogen) are injected into the gas chromatographer where they are flash evaporated onto the column along with a mobile phase carrier gas (Helium). The column is an open temperature controlled tube with a highly viscous liquid stationary phase, with the gas mixture being the mobile phase. The separation of the different constituents of the mixtures takes place depending upon the interactions of the gas mixtures with the stationary phase as they move along the column. Once the gases are separated, the compounds can then be quantitatively analysed by various detectors. [37]

The reaction products were analysed using *Interscience's Compact GC 4.0* which was equipped with two detectors, a Flame Ionisation Detector(FID) and a Thermal Conductivity Detector (TCD) and three channels (one for FID and two for TCD). In the FID detector the eluted compounds are mixed with hydrogen and ionised by combustion. The ionised compounds are then quantified depending upon the current they induce when interacting with a polarised collector plate. This detector is conventionally used to detect volatile hydrocarbons. The TCD works on the principle of change in thermal conductivity that the elueted compounds induce in comparison to the bare carrier gas. This detector was used to analyse nitrogen, hydrogen, oxygen, carbon monoxide and carbon dioxide. [37]

In this study GC was the primary analysis technique used to separate and analyse the formed gaseous products. The gaseous products formed on the surface of the catalyst/working electrode flowed along with the catholyte to the external catholyte bath. The external catholyte bath was supplied with a 20ml/min flow of Nitrogen which acted as a volumetric reference for the reaction products. These reaction products then flow through a condenser tube, to avoid any particulate contamination of the GC column, before entering the GC.

Prior to the CO_2 RR experiments, the GC was calibrated by using different gas mixtures with known volumetric ratios. The calibration plots and a sample calculation for the conversion of the raw GC data to production rates are mentioned in appendix A

3.3.2. HIGH PERFORMANCE LIQUID CHROMATOGRAPHY (HPLC)

High performance/pressure liquid chromatography (HPLC), developed in 1970, is one of the most powerful tools of analytical chemistry. It is used to separate, identify and quantify the different compounds present in a sample. Modern HPLC uses high pressures to force the mobile phase and the analyte through a closed column packed with micron-sized particles, which are the stationary phase. Depending on the interactions that the mobile and stationary phase have, the different constituent compounds are separated and sent to the refractive index detector. A refractive index detector monitors the difference in refractive index of the column eluent and a reference stream containing only the mobile phase. [38] An *Agilent 1260 Infinity HPLC* was used over the course of this work. An Aminex HPX-87H column was used with a 50/50 (v/v) acetonitrile/water mobile phase. 25μl of the sample was injected at a pump flow rate of .8ml/min.

Post the CO_2 RR experiments, 100 μl of the electrolyte was taken from the working and counter electrode chamber for HPLC analysis. The sample from the counter electrode chamber served as a baseline and also indicated the presence of any leak of electrolyte from the working electrode to the counter electrode side. The sample from the catholyte, was analysed for the presence of formic acid, and other liquid products. A refractive index based detector was used for the quantitative analysis of the products formed. As a known volume of catholyte was used for every experiment (60ml), from the concentration obtained via the HPLC results the total amount of the product formed could be easily quantified and the FE%% calculated. The calibration plot for Formic Acid and a set of sample calculations converting the raw data to faradaic efficiency are provided in appendix A

3.4. ELECTROCATALYST CHARACTERISATION

3.4.1. SCANNING ELECTRON MICROSCOPY (SEM)

Scanning electron microscopy is a technique which enables us to achieve resolutions higher than conventional optical microscopes. The resolution of a microscope is limited by the wavelength of the incident beam. In optical microscopy, the incident beam is constituted of packets of photons whose wavelength is limited to 400nm. In the case of matter waves, the De-Broglie wavelength is dependent on the momentum of the wave, which is in turn controlled by the acceleration voltages. By using electron beams, much lower De-Broglie wavelengths are achievable, depending upon the acceleration voltages, thereby achieving much higher resolutions.

Conventional SEM's have typical energy range of (1-30keV). The incident/primary beam of electrons interact with the constituents of the sample and emit secondary electrons which are detected by a Everhart-Thornley detector. The beam is raster scanned over the entire sample surface thereby generating an image of the entire surface. A backscattered electron detector is also used in some cases. The backscattered electrons originate from the subsurface regions of the sample, and their intensity/contrast is dependent directly on the atomic number of the constituent atoms. These electrons therefore helps us to gain a better understanding of the subsurface regime of the sample and also provide a quasi-elemental mapping of the surface. [39]

During this study a FEI Quant 600 SEM with an additional Octane Elect EDX attachment by EDAX was used. Each SEM micrograph attached contains the details of the characterisation parameters but predominantly a 30keV electron beam was used, to achieve the highest possible resolution. The spot size unless otherwise mentioned, was 5.0, and a working distance of 10mm was maintained. The SEM micrographs were used for structural/morphological configuration of the samples. In the case of the metallic nanowires, they were also used to estimate the length of the wires, and establish a relationship between the length of the wires and the deposition parameters.

3.4.2. ENERGY DISPERSIVE X-RAY SPECTROSCOPY (EDX)

Apart from the secondary and back-scattered electrons, the electron beam via inelastic scattering mechanisms can also generate X-rays. Characteristic x-rays are produced when the primary electron beam knocks off an electron from a lower energy electron shell, and the subsequent electron transition from a higher energy states causes an X-ray of a specific energy. These x-rays are dependent on the constituent element and thus can be used for elemental mapping of the entire surface. In this study, EDX analysis was carried out to ascertain the surface coverage of some selected catalysts. [39]

3.4.3. X-RAY DIFFRACTION (XRD)

X-ray diffraction works on the ability of a material to diffract X-rays in a characteristic manner depending on the inter-planar spacing of its crystallographic planes. The X-rays are emitted when accelerated electrons generated by heating a tungsten filament strike a target material. Two types of X-rays are produced when the electrons approach/strike the target, characteristic x-rays that take place due to electronic transitions between different energy levels and Bremsstrahlung x-rays generated due to the deceleration of the electrons close to the nucleus of the target material. By using appropriate filters/monochromators, only the highest in-

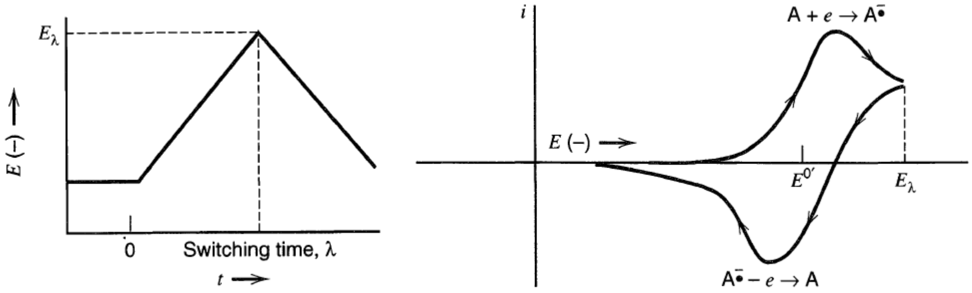
E_λ
E (−) →
0
Switching time, λ
t →
i
$A + e \rightarrow A^{\bar{\bullet}}$
E (−) →
$E^{0'}$
E_λ
$A^{\bar{\bullet}} - e \rightarrow A$

Figure 3.7: Cyclic Voltammetry

tensity K_α radiations are chosen for the diffraction studies. [39] When the X-ray photons, reach the substrate, amongst other interactions constructive interference of the diffracted x-rays from the periodic crystal facets occurs. Bragg's law gives the geometrical interpretation and condition for the XRD phenomena.

$$n\lambda = 2d_{\text{hkl}} sin(\theta) \tag{3.13}$$

where n is the order of diffraction, λ is the wavelength of the incident x-rays, d_{hkl} the inter-planar spacing of the hkl plane, and θ the angle of diffraction. By detecting the diffracted x-rays on changing the angle of diffraction for a constant incident beam wavelength, the inter-planar spacing can be determined. The inter-planar spacing is a characteristic material property and can be directly correlated to a particular crystalline facet (eq:3.14), thereby indicating its presence. [39]

$$d_{hkl} = \frac{a_o}{\sqrt{h^2 + k^2 + l^2}} \tag{3.14}$$

a_0 is the lattice constant, a material property, and hkl are the allowed crystal planes for the crystal structure of the material being tested.

Over the course of this study, a Pananalytical Empyrean XRD, Cu K_α source ($\lambda = .154nm$) and Nickel filter was used. The different catalyst morphologies were characterised to ascertain the presence and ratios of different crystalline facets, as the ratio of the facets has an impact on the CO_2 RR performance.

3.4.4. CYCLIC VOLTAMMETRY

Cyclic Voltammetry(CV) is a powerful electrochemical technique used to investigate the reduction and oxidation processes of molecular species and for the characterisation of electrocatalyst electrode surfaces.[40] In this technique, the current is measured when the potential is linearly swept across a potential regime and then swept back to the initial value. Fig. 3.7 depicts a typical cyclic potential sweep and the resulting cyclic voltammogram and the oxidation and reduction peaks. Cyclic voltammetry can provide us information pertaining to both, the potential regions where there is a faradaic process such as a redox reaction occurring, and the potential regions where non-faradaic processes such as double layer charging are taking place. [41] [35]

In this study, CV is used to determine the electrochemically active surface area (ECSA). The ECSA was estimated from the non-faradaic capacitive current associated with the double layer charging from scan-rate dependent cyclic voltammograms. To measure the double layer capacitance (C_{DL}), a potential regime was chosen where no faradaic process occurred, in our case, -0.4V to -0.9V vs Ag/AgCl. The CV was run at multiple scan rates (v) to obtain the charging currents (i_c) pertaining to specific scan rates. A minimum of 3 scans were run for each scan rate, and the second scan was chosen for the estimation of the area. The charging current at particular arbitrary potential (-0.6V vs Ag/AgCl) was determined in the oxidation and reduction cycle for each scan rate. The difference of the charging currents was plotted against the applied scan rate, and a linear relation between the charging current and the scan rate was obtained. The electrochemical double layer capacitance, in Farads, was represented by the slope of the linear regression line of the current vs scan rate plot. (Eq. 3.15) The measurements were done under constant CO_2 flow and in a 1M KOH electrolyte. [42] [43]

$$i_c = vC_{DL} \tag{3.15}$$

The ECSA was determined by comparing the obtained capacitance(C_{DL}) to the capacitance of a perfectly flat copper plate of a known area.

4

CATALYSTS

This chapter deals with the approach taken for the synthesis of the catalyst. A description of the in-situ synthesis process on the carbon cloth and the different morphologies obtained is mentioned. The XRD and SEM data are also discussed for the different morphologies. This is followed by a discussion on copper nanowire synthesis and the challenges it poses for direct use as GDE catalysts. Additionally, enlarged SEM images of the different catalyst morphologies synthesised are provided in App. D

4.1. CARBON CLOTH WITH MICROPOROUS LAYER

For this set of experiments a woven carbon cloth GDL with a microporous layer was chosen as the substrate for the electrodeposition of copper. The microporous layer of carbon nanoparticles aids the diffusion of the gas over the GDL layer, and improves the electrical contact. The cloth also had a polytetrafluoroethylene hydrophobic coating to prevent fouling of the gas diffusion layer. [21] The properties of the carbon cloth and its Raman spectra are provided in App. C

Three different morphologies were synthesised on this carbon cloth. The different morphologies were obtained by changing the current density while the deposition time was kept constant at 500 seconds. The synthesis was carried out in the electrodeposition setup depicted in Fig. 3.5. The synthesis was repeated multiple times (>3) to ensure the reproducibility of the structures observed. This in-situ growth of the catalyst directly on the GDL is a novel synthesis approach which drastically reduces the number of steps in the catalyst preparation thereby making it readily industrially relevant. A more elaborate discussion on different catalyst synthesis approach is carried out in Ch. 2.

4.1.1. MORPHOLOGY 1 - 100MA

For this morphology the copper electrodeposition was carried out at 100mA (current density - 16mA/cm^2) for a duration of 500 seconds. A poly-crystalline film of copper was obtained, as seen in Figs. 4.2 - 4.4. The

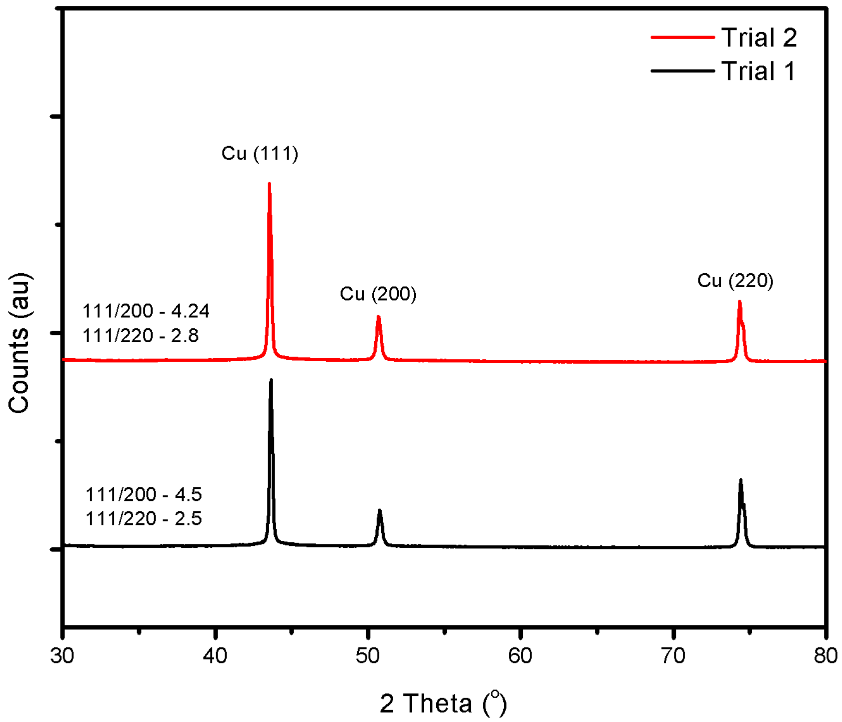

Figure 4.1: XRD Spectra of Morphology 1

synthesized copper film had a loading of 2.63 g/cm^2 and was calculated using Eq. 3.11. The copper film showed a strong presence of Cu (111) facets evidenced by the XRD spectra in Figure 4.1. The ratios of the 111/200 and 111/220 peaks were found to be 4.35 and 2.65 respectively.

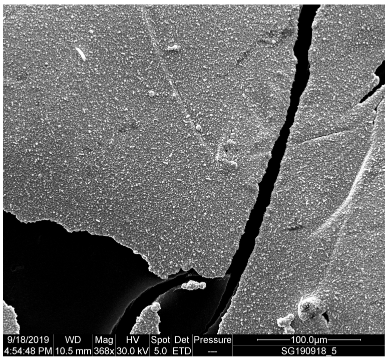
9/18/2019 WD Mag HV Spot Det Pressure 100.0µm
4:54:48 PM 10.5 mm 368x 30.0 kV 5.0 ETD --- SG190918_5

Figure 4.2: SEM Micrograph of Morphology 1 - 350x

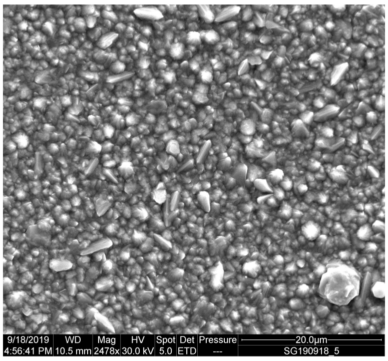
9/18/2019 WD Mag HV Spot Det Pressure 20.0µm
4:56:41 PM 10.5 mm 2478x 30.0 kV 5.0 ETD --- SG190918_5

Figure 4.3: SEM Micrograph of Morphology 1 - 2500x

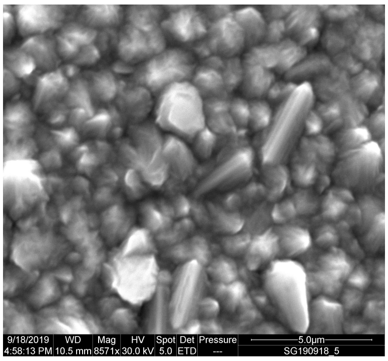
9/18/2019 WD Mag HV Spot Det Pressure 5.0µm
4:58:13 PM 10.5 mm 8571x 30.0 kV 5.0 ETD --- SG190918_5

Figure 4.4: SEM Micrograph of Morphology 1 - 8500x

4.1.2. MORPHOLOGY 2 - 50MA

For this morphology the current used for the electrodeposition was reduced to 50mA (current density - 8mA/cm^2) for the same duration of 500 seconds. This was done with a view to increase the porosity of the film, to aid the diffusion of the gas. As is seen in Fig. 4.5 - Fig. 4.7, a more porous, less-dense poly-crystalline film was obtained. The loading of the copper was experimentally calculated to be 1.31 g/cm^2. Fig. 4.8, depicts the

XRD spectra of the synthesized catalyst. The ratios of the 111/200 and 111/220 peaks were found to be 4.0 and 7.4 respectively. This morphology showed less pronounced Cu(220) facets compared to Morphology 1. Additionally, the figure also, depicts the reproducibility of the catalyst synthesis, and for the three trial runs we observe a very similar peak/peak ratios. The reporducibility was also evidenced by the SEM micrographs and the data from the potentiostat. For the purposes of the CO_2 RR experiments, this morphology is more promising, due to lesser loading and enhanced porosity, thereby improving the diffusion of the gas.

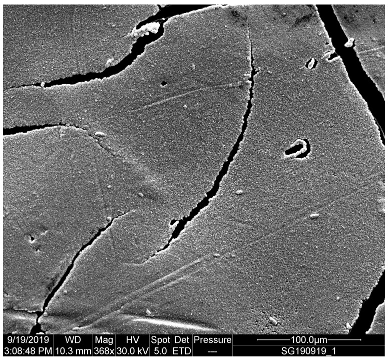
9/19/2019 WD Mag HV Spot Det Pressure
3:08:48 PM 10.3 mm 368x 30.0 kV 5.0 ETD ---
100.0μm
SG190919_1

Figure 4.5: SEM Micrograph of Morphology 2 - 250x

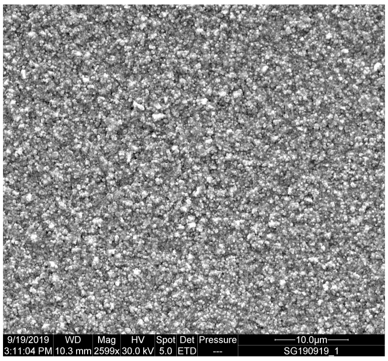
9/19/2019 WD Mag HV Spot Det Pressure
3:11:04 PM 10.3 mm 2599x 30.0 kV 5.0 ETD ---
10.0μm
SG190919_1

Figure 4.6: SEM Micrograph of Morphology 2 - 2500x

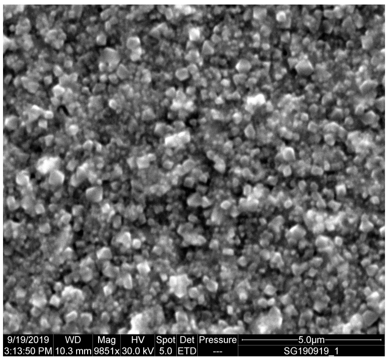
9/19/2019 WD Mag HV Spot Det Pressure
3:13:50 PM 10.3 mm 9851x 30.0 kV 5.0 ETD ---
5.0μm
SG190919_1

Figure 4.7: SEM Micrograph of Morphology 2 - 10000x

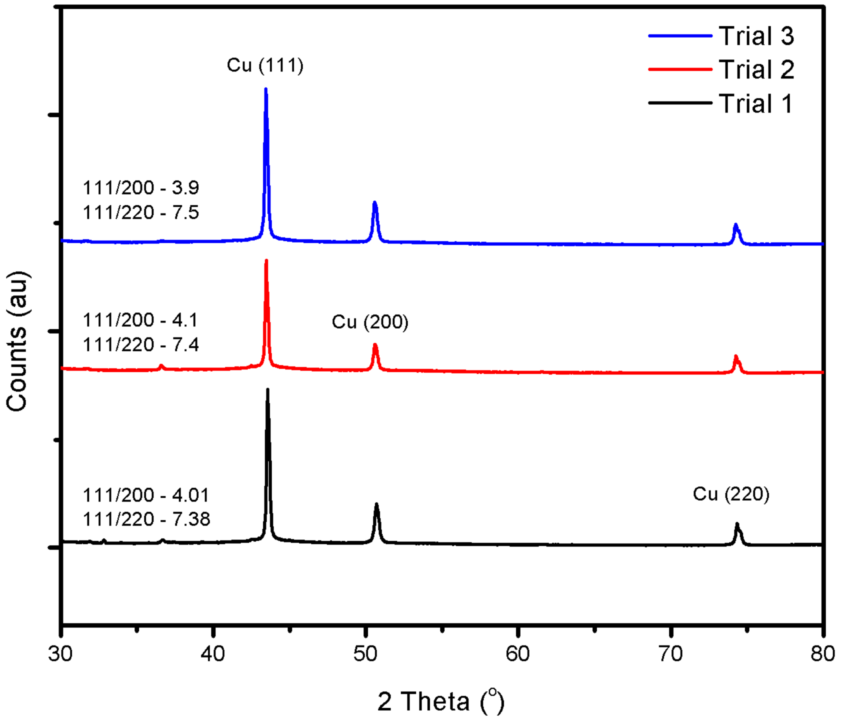

Figure 4.8: XRD Spectra of Morphology 2

4.1.3. MORPHOLOGY 3 - 10MA

On further decreasing the plating current to 10mA (current density - 1.6mA/cm^2) a completely different structure of spherical copper crystals was observed. Fig. 4.9 to Fig. 4.11 show the morphology of the synthesized catalyst. These catalysts also had a much lower experimentally derived loading of .262 g/cm^2. From the XRD data in Fig. 4.12, the ratio of the 111/200 and 111/220 peaks were found to be 4.25 and 11.2 respectively. There is a drastic decrease in the Cu(220) facets, in comparison to morphology 1 and 2 whereas the difference in the Cu(200) facets amongst the three different morphologies is considerably lesser. Fig. 4.12 also includes the data obtained by the other runs of the synthesis experiment to prove the reproducibility of the morphology synthesis. Whilst, the Cu 111/200 peak ratio is constant for the three different trials, there is a small difference the ratio of the 111/220 peaks. This is due to the 220 peaks being of very low intensities and therefore giving rise to a larger deviance in the peak ratio calculations.

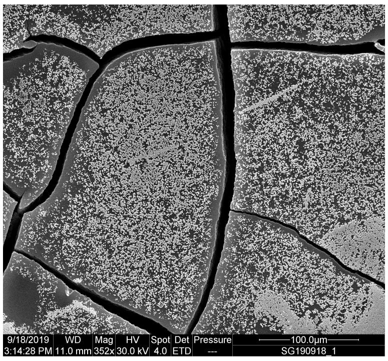
9/18/2019 3:14:28 PM | WD 11.0 mm | Mag 352x | HV 30.0 kV | Spot 4.0 | Det ETD | Pressure ---
100.0µm
SG190918_1

Figure 4.9: SEM Micrograph of Morphology 3 - 350x

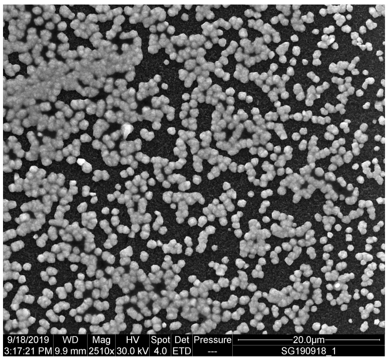
9/18/2019 3:17:21 PM | WD 9.9 mm | Mag 2510x | HV 30.0 kV | Spot 4.0 | Det ETD | Pressure ---
20.0µm
SG190918_1

Figure 4.10: SEM Micrograph of Morphology 3 - 2500x

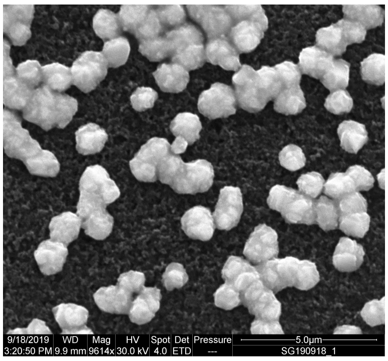
9/18/2019 3:20:50 PM | WD 9.9 mm | Mag 9614x | HV 30.0 kV | Spot 4.0 | Det ETD | Pressure ---
5.0µm
SG190918_1

Figure 4.11: SEM Micrograph of Morphology 3 - 10000x

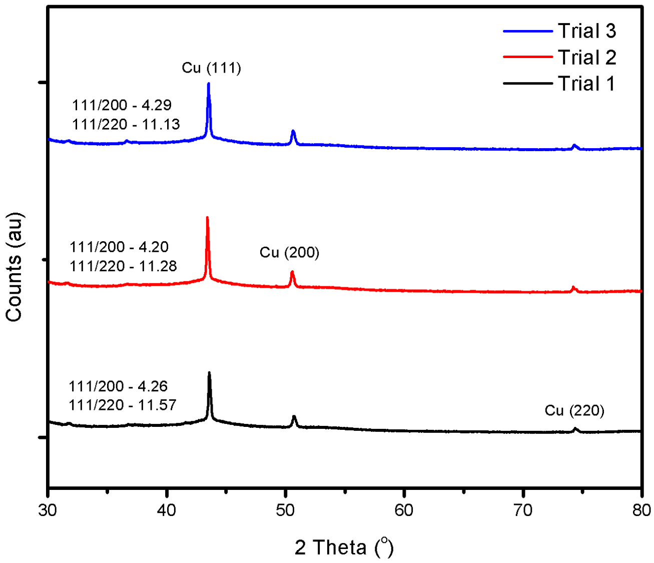

Figure 4.12: XRD Spectra of Morphology 3

4.1.4. DISCUSSION

As was already discussed in previous subsections, and also evident from the Fig. 4.13 the different morphologies have different crystalline structures, which should catalyse the CO_2 RR towards different products. It is seen from Fig. 4.13 that the Cu (111) facet remains the most dominant facet in all the three cases. The Cu (111)/Cu (200) ratio remains relatively constant in the three morphologies and not a lot of conclusions can be drawn from this as there is no observable trend. There is though an observable decrease in the Cu (111)/Cu (220) facets on increasing current density (going from morphology 3 to morphology 1). This implies that as we increase the current density (from morphology 3 to morphology 1), we get more Cu (220) facets which suggests that as the deposition process goes on, the copper growth takes place along the Cu (220) facets and the initial growth of the copper particles takes place along the Cu (111) and Cu (200) facets. Increasing the current density (for the same deposition time) firstly leads to more material being deposited as more charge is transferred, additionally, the current density also affects the kinetics of the nucleation and growth. In the case of the lowest current density (morphology 3) we see distinct spherical copper clusters. The reason for the different morphology could be due to the fact that we don't have enough copper to cover the entire surface in a thin film (like Morphology 1 & 2) and/or that due to the lower current densities we alter the nucleation/-growth mechanism. At low current densities we nucleate lesser sites and the growth then takes place only on those sites. This is as opposed to nucleating more number of sites at higher current densities, and thereby achieving a poly-crystalline film.

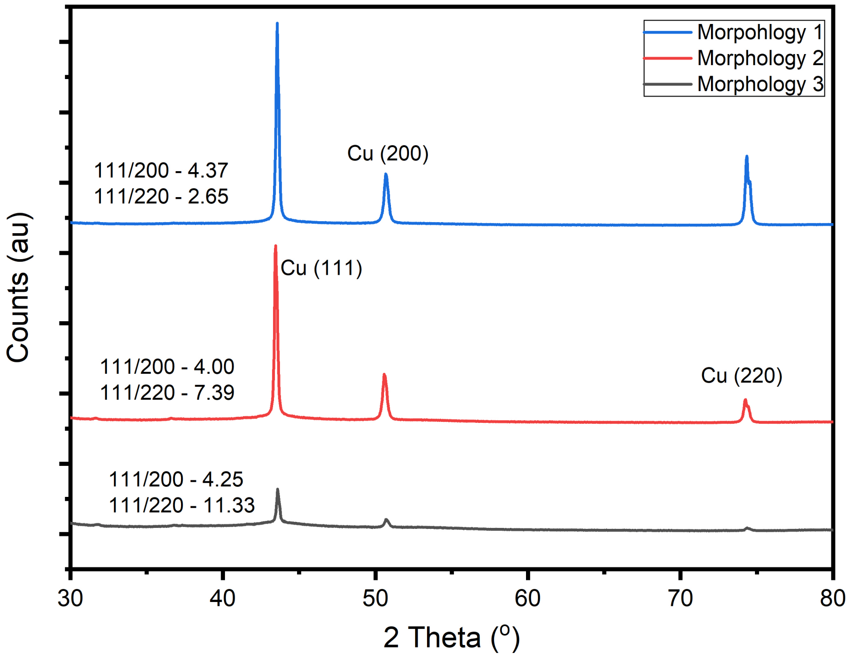

Figure 4.13: XRD Spectra of the 3 different morphologies on Carbon Cloth - W1S1009

To ascertain the reasons behind the difference in morphologies, further experiments would need to be carried out. For the three different current densities used, experiments must be carried out at time intervals such that in all the three cases the charge transferred (material deposited) is the same. If on doing so we observe a different structure in the three cases then it can be asserted that the difference in structure observed in this study is due to different nucleation and growth process and not on the amount of material deposited (charge transferred). If instead we observe a similar structure for the same amount of charge transferred (material deposited), then the difference in morphologies we see in the SEM images of this study, could be attributed just to the amount of material deposited and not the kinetics of the growth.

Additionally, a more thorough study on copper electrodeposition on different GDL, different deposition parameters (time, current/potentials) could be undertaken to obtain a large data set of different crystalline structures obtained with the change in parameters. This would enable us to make a more rational choice for the selection of the catalyst morphology, as the crystalline structure of the catalyst plays a vital role in the CO_2 RR product selectivity.

4.2. COPPER NANOWIRES

Nanowires are an interesting morphology, due to the high ECSA that they offer in the same geometrical area of the electrode. Higher ECSA would provide higher active surface areas for the electrocatalytic reduction of CO_2, resulting in higher production rates and therefore higher current densities. The use of nanowires was limited in the H-cell based method due to CO_2 mass transfer limitations inherent to the system. [44] (These limitations are discussed in Ch. 2.) The use of GDE helps overcome these CO_2 transport limitations, making nanowires an interesting morphology for use as electrocatalysts in a vapor-phase electroysers.

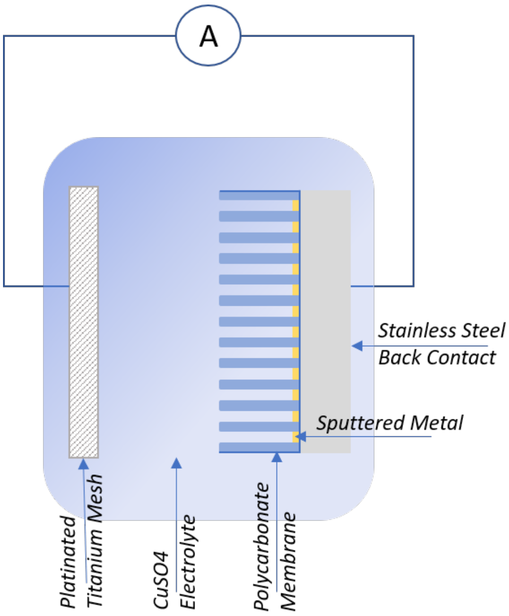

Figure 4.14: Schematic of the nanowire plating setup

The copper nanowires were synthesized by templated-electrodeposition within commercial PCTE membranes. A schematic of the setup used for the synthesis of the nanowire is shown in Fig. 4.14. The setup used is similar to the one described in Ch. 3.2 with the only difference being that instead of using a carbon cloth a PCTE membrane was used as a substrate on the stainless steel back contact.

The side of the PCTE membrane in contact with the stainless steel back plate was evaporated with a 200nm thick coating of gold/silver. This helped to block the pores on one side for the deposition process and to also provide an electrical pathway to the stainless steel back contact. On applying cathodic current on the working

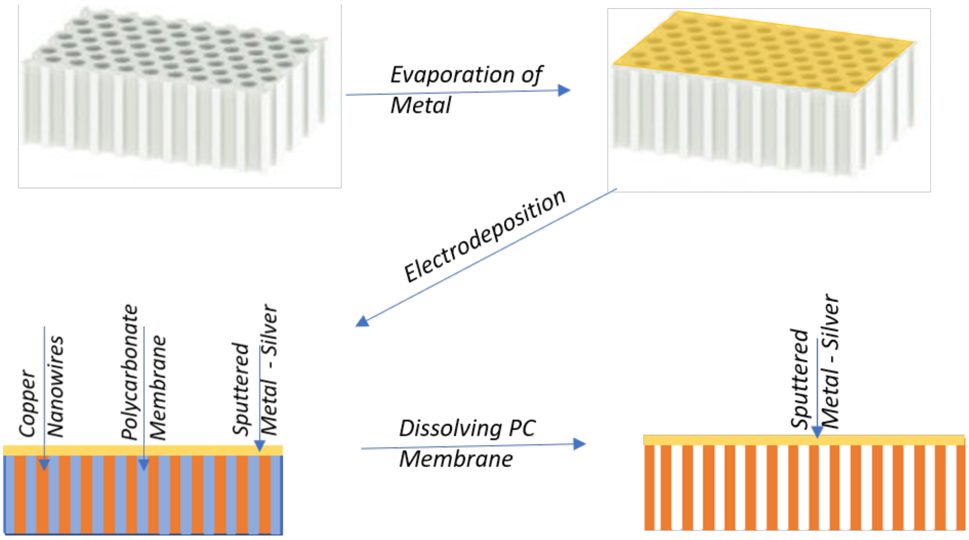
Evaporation of Metal
Electrodeposition
Copper Nanowires
Polycarbonate Membrane
Sputtered Metal - Silver
Dissolving PC Membrane
Sputtered Metal - Silver

Figure 4.15: Schematic depicting the synthesis approach for copper nanowires

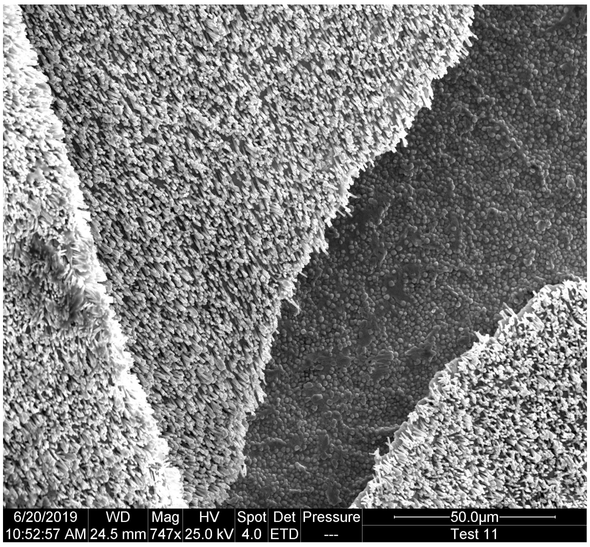
6/20/2019 10:52:57 AM
WD 24.5 mm
Mag 747x
HV 25.0 kV
Spot 4.0
Det ETD
Pressure ---
50.0µm
Test 11

Figure 4.16: SEM micrograph of Synthesized copper nanowires - 750x

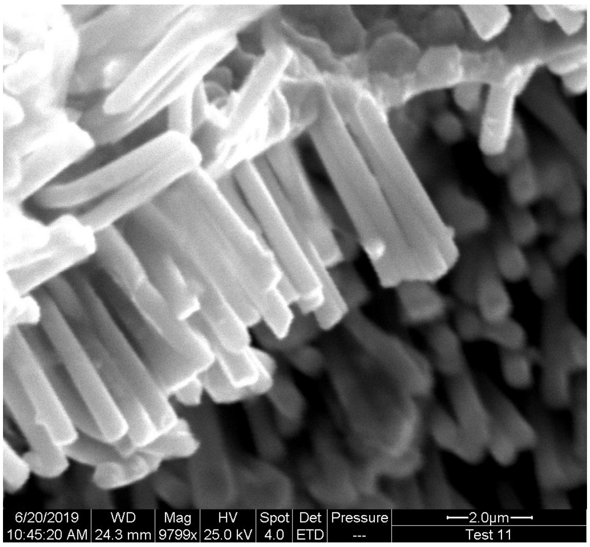
6/20/2019 10:45:20 AM
WD 24.3 mm
Mag 9799x
HV 25.0 kV
Spot 4.0
Det ETD
Pressure ---
2.0µm
Test 11

Figure 4.17: EM micrograph of Synthesized copper nanowires - 10000x

electrode, the copper in the electrolyte reduces on the evaporated metal within the pores of the membrane. As the deposition process goes on, more and more of the copper ions reduce in the pores of the PCTE membrane eventually filling them. The length of the wires is controlled by the deposition time and current densities whereas the diameter of the wires was dependent on the pore diameter of the commercial PCTE membrane. After obtaining the desired length, the polycarbonate was dissolved in dichloromethane for 30 minutes, and nanowires supported on the evaporated metallic contact were obtained. Fig. 4.15 schematically depicts the approach taken for the copper nanowire synthesis.

Figures 4.16 & 4.17 depict the synthesized copper nanowires. As is seen from the images, the distribution of the copper nanowires is homogeneous over the entire surface of the evaporated metal. The XRD spectra of the copper nanowires synthesized, seen in Fig. 4.18, shows a predominance of the Cu(111) peak over the Cu(200) and Cu (220) peaks. The ratio of the Cu 111/200 peaks and Cu 111/220 are 4.22 and 8.25 respectively. The peaks corresponding to silver arise due it being the evaporated metal in this case.

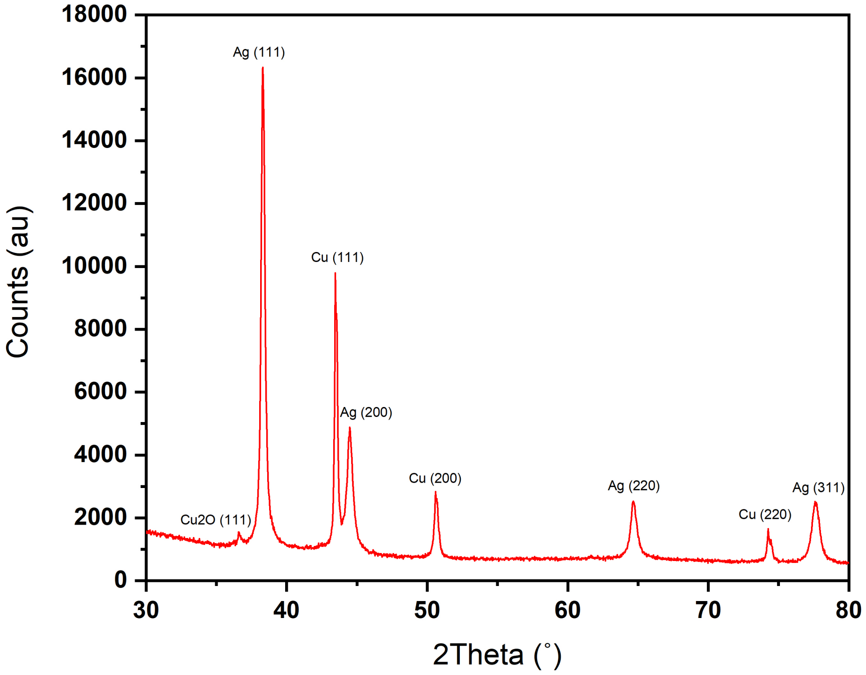

Figure 4.18: XRD spectra of copper nanowires

Whilst, these nanowires are interesting as electrocatalysts for CO_2 RR they couldn't be directly as a GDE due to the evaporated metallic layer acting as a barrier between the CO_2 and the electrolyte. This problem is schematically represented in Fig. 4.19. The evaporated metal (thick black line) prevents the CO_2 to diffuse towards the electrolyte to interact with the hydrogen ions present in the electrolyte. Two different approaches were taken to overcome this problem. The first approach involved using a mask during the evaporation of the metal and the other involved in-situ growth of the catalyst directly on the GDL.

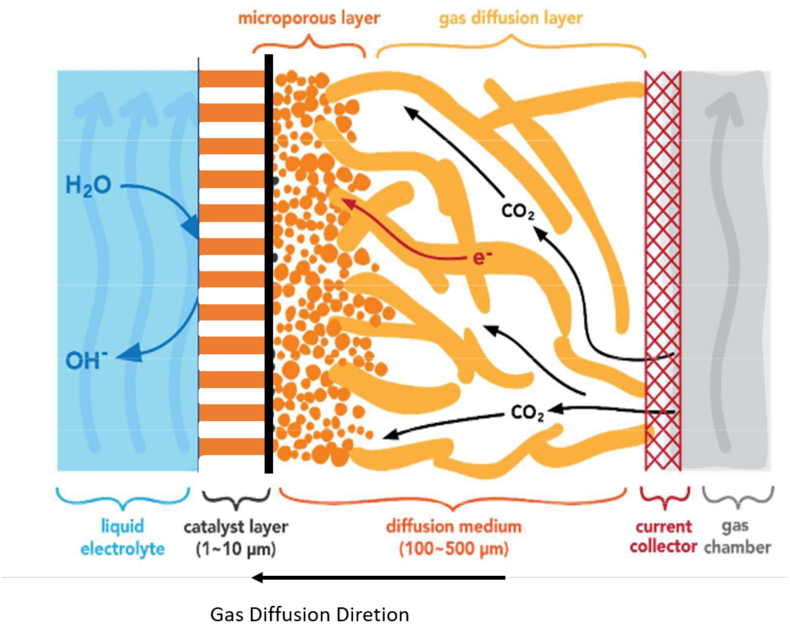
microporous layer
gas diffusion layer
H₂O
OH⁻
CO₂
e⁻
CO₂
liquid electrolyte
catalyst layer (1~10 μm)
diffusion medium (100~500 μm)
current collector
gas chamber
Gas Diffusion Diretion

Figure 4.19: Porosity issue with copper nanowires

4.2.1. APPROACHES TO OVERCOME CO_2 DIFFUSION LIMITATIONS

MASKING

In this approach, a mask was placed over the PCTE during the evaporation process. This resulted in the metal being deposited only on specific places depending on the geometry of the mask used. This can be seen schematically in Fig. 4.20, wherein by using a mask, the metal was deposited only on specific parts of the PCTE template.

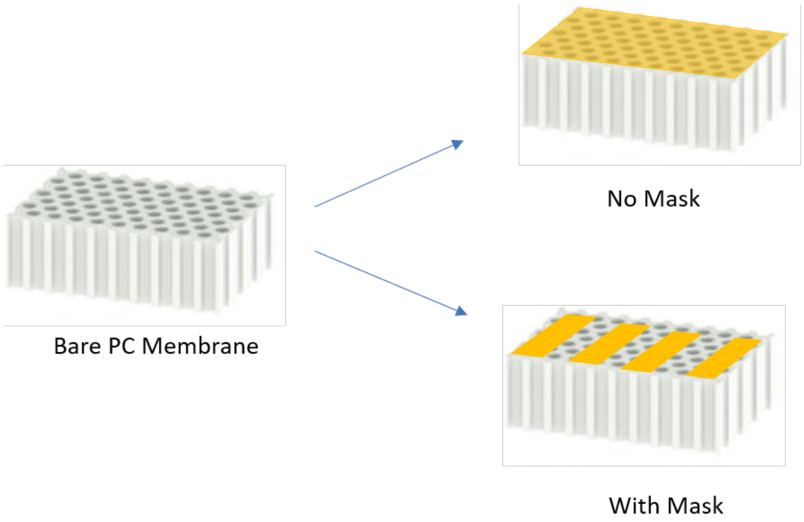
Bare PC Membrane
No Mask
With Mask

Figure 4.20: Masking during evaporation of metal to provide diffusion pathways for CO_2

As the evaporated metal, acts as the site on which the initial nucleation and growth of the nanowires occurs, the copper wires are only grown in the areas where there is a presence of the evaporated metal. This enables us to selectively grow the nanowires in certain areas of the PCTE template and the other areas allow for the diffusion of the CO_2

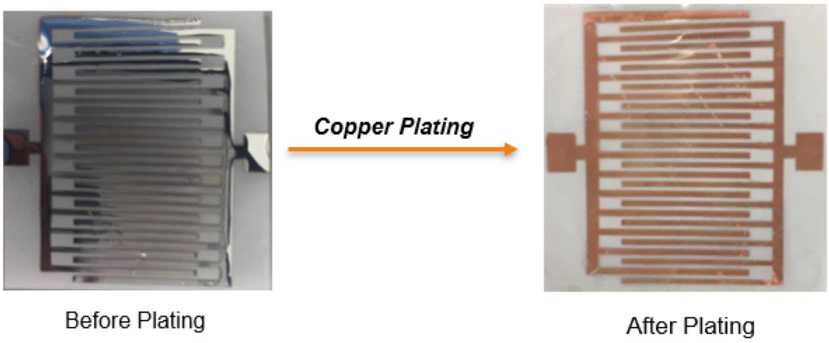

Figure 4.21: Electrodepostion of copper on masked PCTE templates

For the conventional growth of the nanowires, the evaporated metal (in this image - Silver) was deposited homogeneously over the entire polycarbonate membrane. In this approach however, as a mask was used, the evaporated metal (silver) was only present in specific places depending on the geometry of the mask. After using the desired copper plating conditions, it was seen that the deposition of the copper only occurred in the region where the evaporated metal was present. This is also evidenced visually in Fig. 4.21, wherein post plating the regions where the evaporated metal was present, show a reddish-brown color indicating the presence of copper. Using this approach the CO_2 could now diffuse through the regions where there was no growth of wires/no presence of the evaporated metal. This process could be further improved by using mask's which had lower inter-fringe distances to increase the coverage of the nanowires. Additionally further work needs to be done to improve the mechanical rigidity before testing these nanowires as catalysts in a GDE.

IN-SITU GROWTH OF COPPER NANOWIRES ON THE GDL

In this approach the carbon GDL was used as the conductive support for the polycarbonate template instead of an evaporated metal. It was presupposed that copper would initially deposit onto the conductive carbon gas diffusion layer, and then through further deposition, grow through the pores of the polycarbonate template, resulting in nanowire like structures. This would imply not requiring the layer of evaporated metal thereby overcoming the diffusion limitation of the CO_2. A schematic of this is shown in Fig. 4.22, where its seen that the PCTE template was clamped on the GDL inside the electrodeposition holder. After clamping the PCTE template and the GDL in place, copper nanowires were grown using similar conditions as mentioned above.

On characterising the samples, no growth of nanowires was observed on the carbon gas diffusion layer as is seen in Fig. 4.23. Instead an entirely different structure was obtained on the gas diffusion layer which had a flattened top surface. The deposition entirely took place on the GDL and the presence of the PCTE clamped on top of the membrane acted as a barrier to the natural growth of the copper film. The PCTE template on the other hand showed some presence of a copper nanowire like morphology (Fig. 4.25), but these were not homogeneously distributed over the entire PCTE membrane.

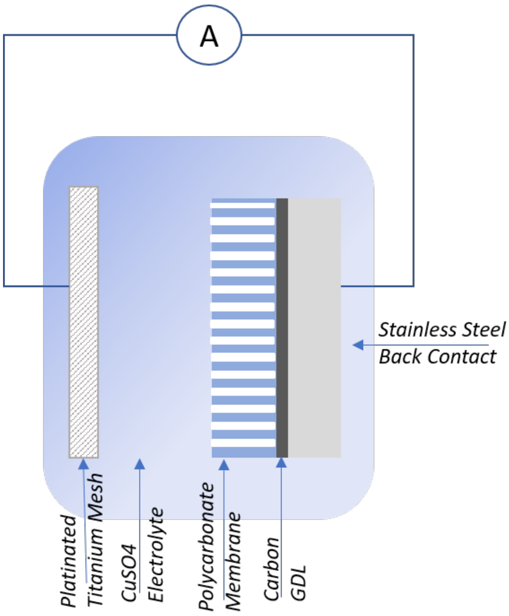
A
Stainless Steel
Back Contact
Platinated
Titanium Mesh
CuSO4
Electrolyte
Polycarbonate
Membrane
Carbon
GDL

Figure 4.22: In-situ growth of nanowires on the GDL

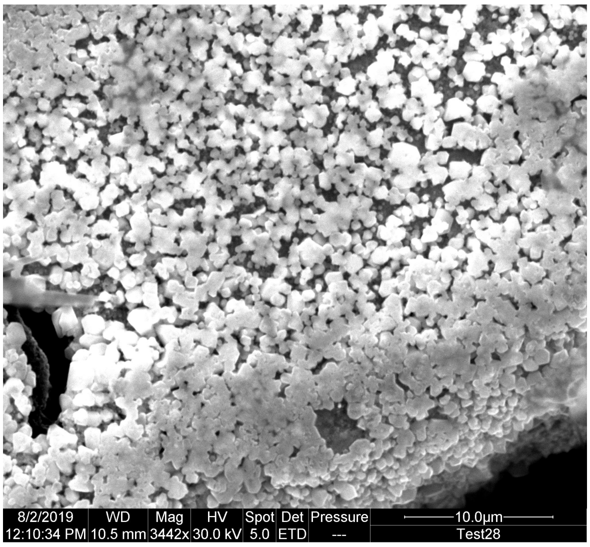
8/2/2019 12:10:34 PM
WD 10.5 mm
Mag 3442x
HV 30.0 kV
Spot 5.0
Det ETD
Pressure ---
10.0µm
Test28

Figure 4.23: SEM Micrograph of in-situ copper nanowire growth approach

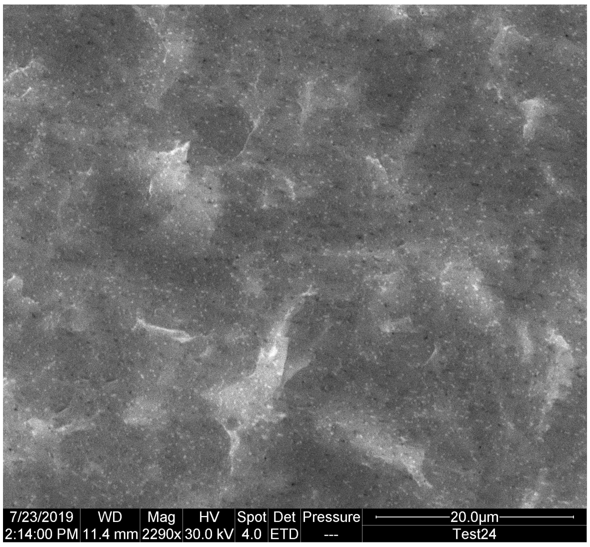
7/23/2019 2:14:00 PM
WD 11.4 mm
Mag 2290x
HV 30.0 kV
Spot 4.0
Det ETD
Pressure ---
20.0µm
Test24

Figure 4.24: SEM Micrograph of in-situ copper nanowire growth approach

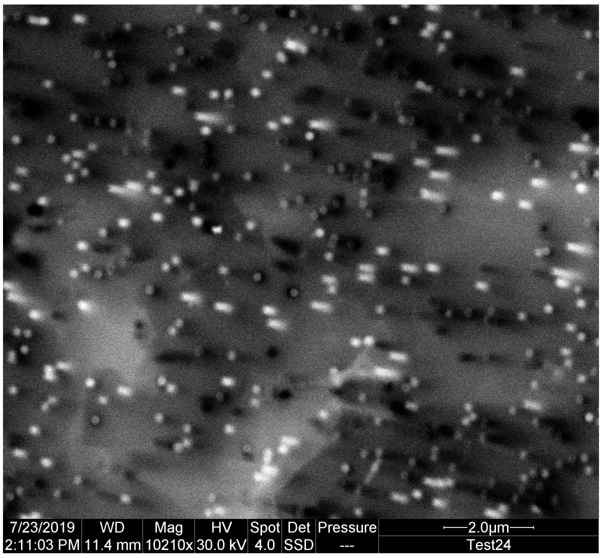
7/23/2019
2:11:03 PM
WD
11.4 mm
Mag
10210x
HV
30.0 kV
Spot
4.0
Det
SSD
Pressure

2.0µm
Test24

Figure 4.25: Backscatter SEM micrograph of in-situ copper nanowire growth

5

CO_2 RR RESULTS AND DISCUSSION

The results of the CO_2 RR experiments on morphology 3 are presented and discussed in this chapter. Morphology 3 was selected for the first set of experiments due to the the high porosity of the synthesized catalyst and the spherical structure, not observed previously in literature. The current density observed and the FE% of the different CO_2 RR products are discussed. The characterization results of the used catalysts are also mentioned. This is followed by an overarching discussion on the results of the CO_2 RR performance of this morphology. The chapter is concluded by a discussion on the pulsed electrolysis experiments conducted to increase the lifetime of the catalyst.

5.1. CURRENT DENSITY

For the different potentials applied, current density values were measured over the course of the reaction. Fig. 5.1 depicts the current density response as a function of time for the different potentials applied. It is observed that the current density gradually increases as the CO_2 RR reaction proceeds over time. The increase in current density could be due to the formation of reduction products that improve the conductivity of the electrolyte. Additionally, from the SEM images taken post the reaction, a change in the morphology of the catalysts is observed. This change in morphology could also result in higher electrochemically active surface area and therefore an increase in the current density could be attributed to it. Fig. 5.2 depicts the current density (measured at 20 mins) vs potential relationship. On applying different reduction potentials, it is seen that the current density changes. As expected the current density increases with an increase in the applied potential.

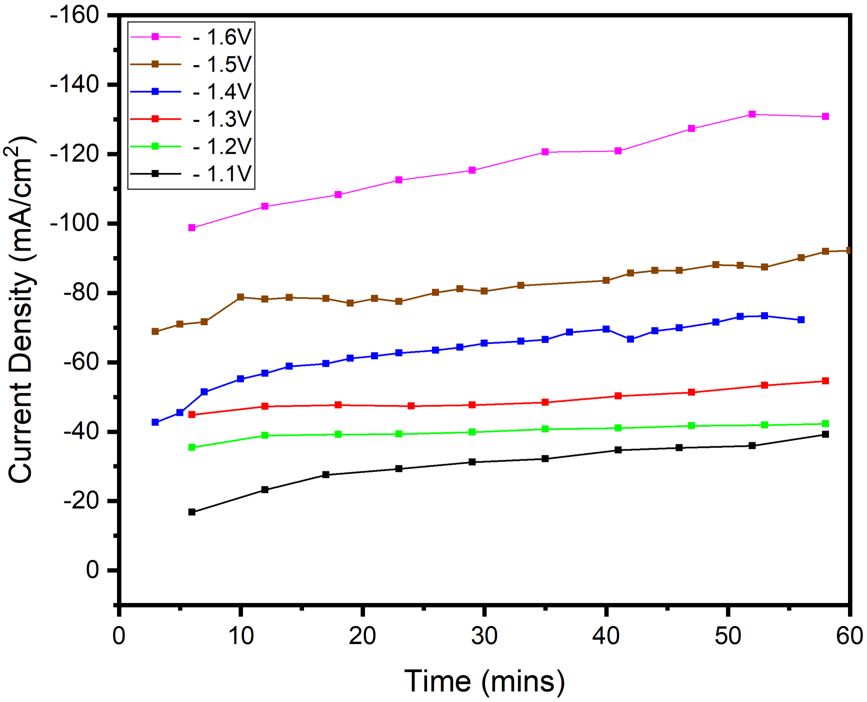

Figure 5.1: Current density vs time for the different applied potentials

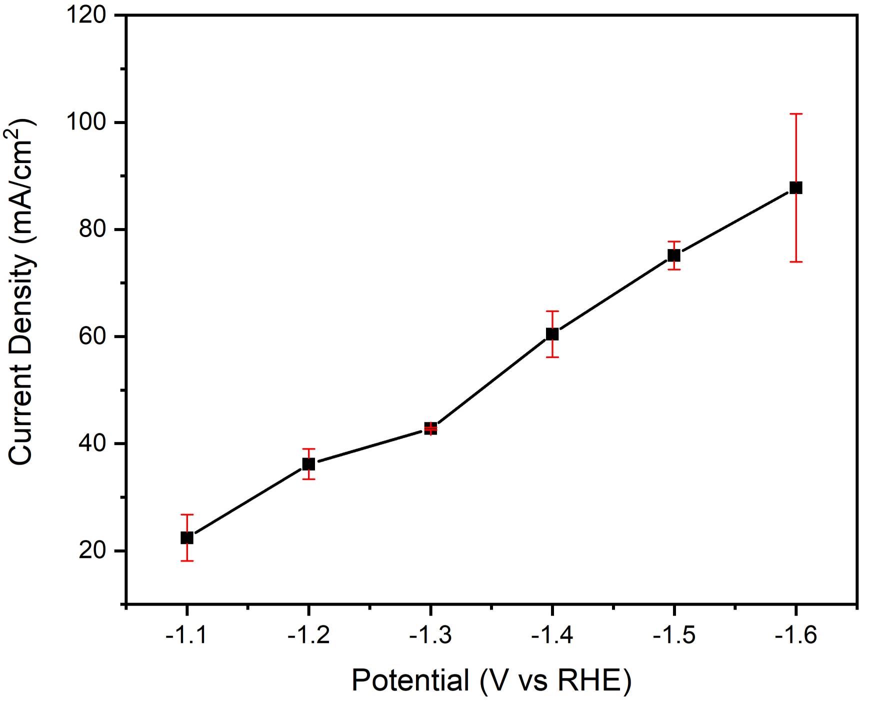

Figure 5.2: Current density at 20 minutes averaged over two repetitions

5.2. ETHYLENE

Fig. 5.3 & Fig. 5.4 depict the change in the faradaic efficiency and the flow rate of ethylene with respect to time. It is clearly evident that the formation of ethylene reaches a peak value at about 20 minutes after the start of the reaction and the catalyst then slowly deactivates resulting in the production of only hydrogen. From Fig. 5.4 it can also be seen, that the rate of deactivation of the catalyst for ethylene formation is related to the applied potential values. As the applied potential is increased, a general trend is observed wherein the rate of deactivation of the catalyst also increases. This suggests that increased reaction rates/potentials result in faster deactivation of the catalyst. The peak faradaic efficiency obtained for ethylene is 18% at -1.5 V vs RHE (uncompensated). Whilst the production rate (flow rate) is higher in the experiment conducted at -1.6 V, the overall faradaic efficiency is lower, due to much higher total current densities in the experiment at -1.6 V. This implies that the excess current was being used up for the hydrogen evolution reaction, thereby negatively impacting the ethylene faradaic efficiency.

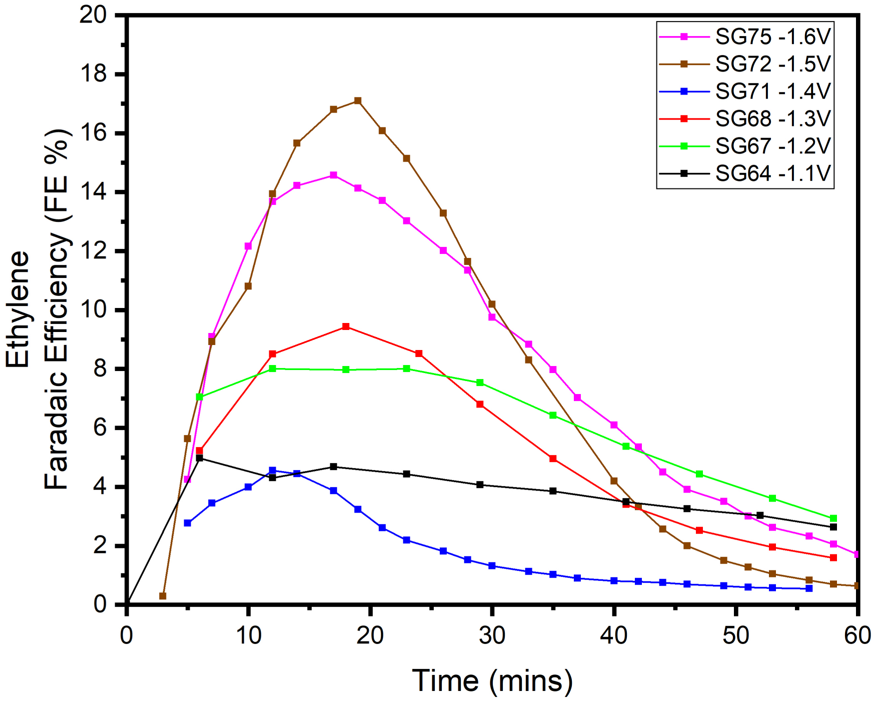

Figure 5.3: Ethylene Faradaic Efficiency

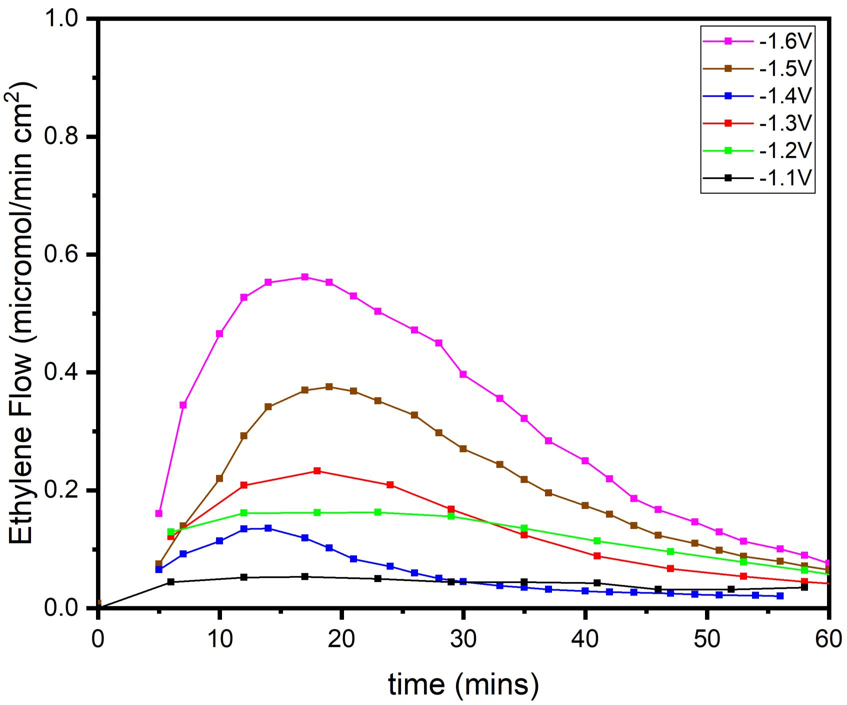

Figure 5.4: Ethylene Flow

5.3. METHANE

A very similar trend as seen for ethylene was observed for methane too. This suggests that both methane and ethylene follow a very similar pathway for CO_2 RR on the predominant crystal facets of the synthesized catalysts. The synthesized catalysts show a predominance of Cu (111) facets over the Cu (220) and Cu (200) facets as is evident from Fig. 4.12. From literature, it is known that on Cu (111) facets, both methane and ethylene share a similar pathway for CO_2 RR. As the catalyst being tested showed a high amount of Cu (111) facets, it is reasonable that we see significant methane and ethylene production. If instead of Cu (111) facets, the catalyst showed a predominance of Cu (220)/ Cu (200) facets, ethylene would be the major component, with trace amounts of methane. The discussion on the relation between the crystal structure and the product selectivity is dealt with in Ch. 2. A peak faradaic efficiency of 13% was observed for methane at -1.6 V vs RHE, and the peak methane flow of .8 micromol/min cm_2 was also observed at -1.6 V.

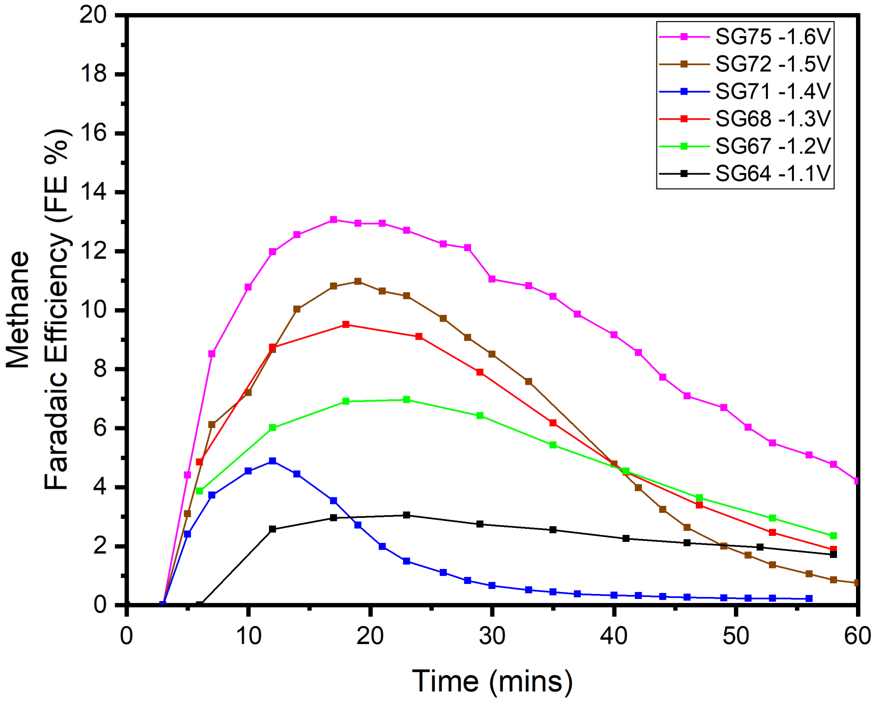

Figure 5.5: Methane Faradaic Efficiency

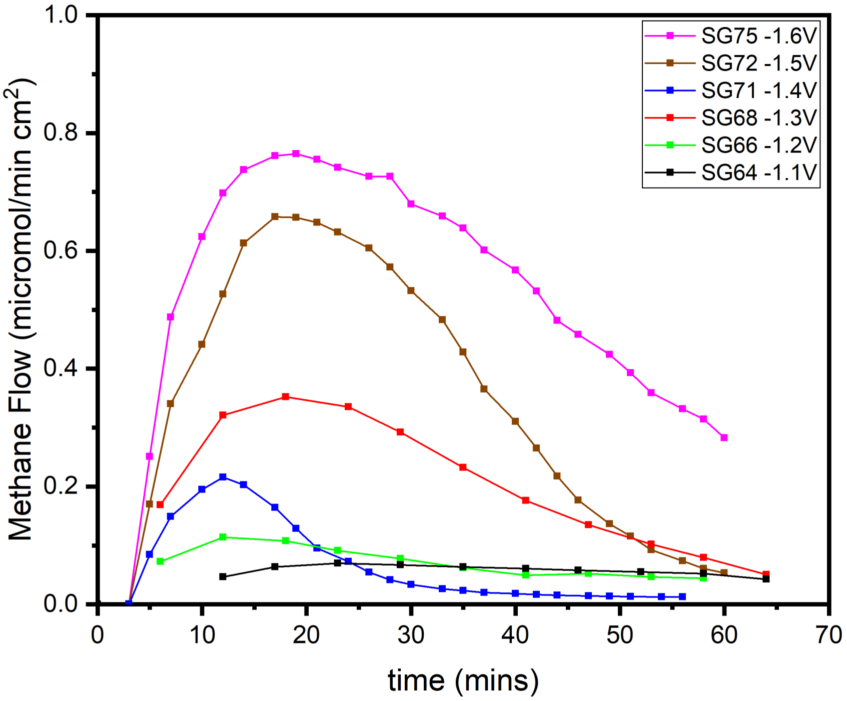

Figure 5.6: Methane Flow

5.4. FORMIC ACID

Formic Acid production showed faradaic efficiency vs potential relation different compared to methane and ethylene. This is due to formic acid having a considerably different reaction pathway. The peak formic acid production of 19.3% is observed at -1.1 V vs RHE. At -1.2 V it drops to 18.9%. On further increasing the potential, the faradaic efficiency drops and then stabilizes at around 7% at the highest potentials. The calculations for formic acid were carried out only at the end of the experiment and therefore a relation of the formic acid production with time for all the experiments is not shown. For one of the experiments, liquid samples were taken at four different intermittent times to establish whether formic acid production took place at the beginning of the reaction or at the end. Fig. 5.7 depicts the cumulative production of the formic acid. It can be seen from this that within the first 10 minutes 0.2 mmols of formic acid is produced which is 60% of the total formic acid production. Fig. 5.8 depicts the change in the production rate of Formic acid with time, it is seen that the peak formic acid production rate is at the beginning of the reaction and then starts to decrease. Therefore, the majority of the formic acid production takes place in the first 10 minutes of the reaction. While the production rate of formic acid decreases after the first 10 minutes, the production of the other hydrocarbons continues to increases till 20 minutes. From this it can be understood that the initial low production of methane and ethylene could be attributed to the competition with formic acid.

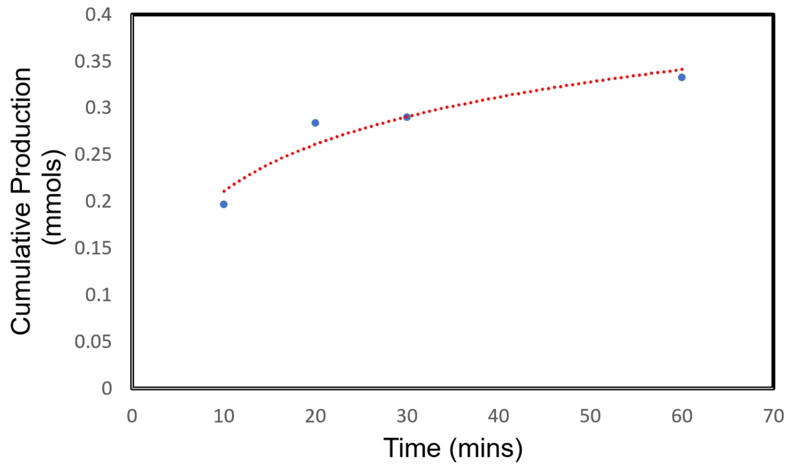

Figure 5.7: Formic Acid Production

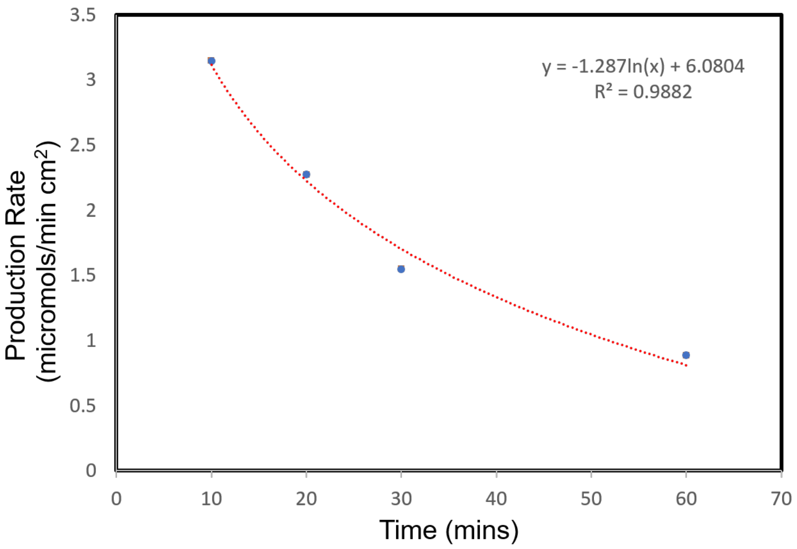

Figure 5.8: Formic Acid Production

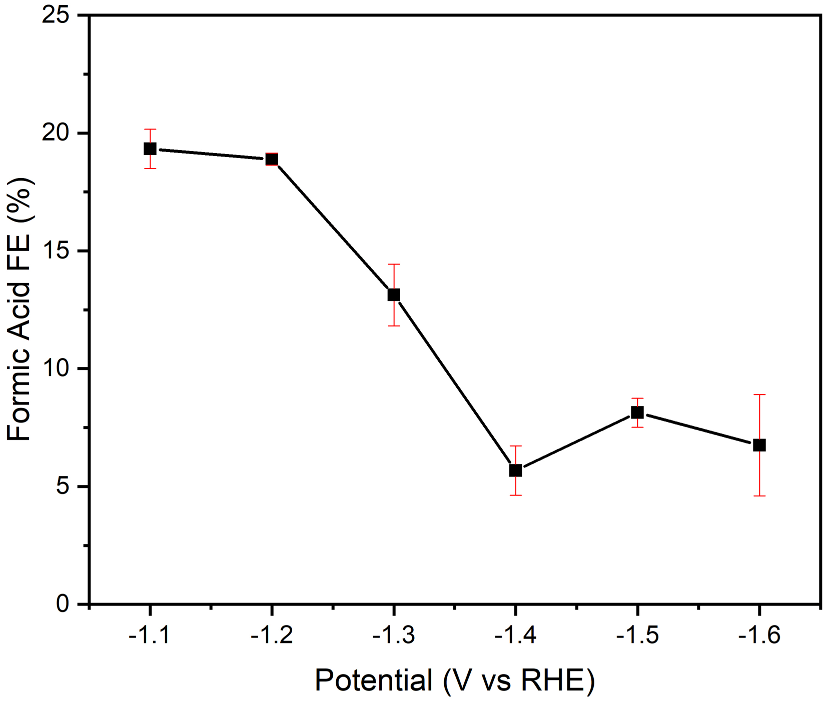

Figure 5.9: Formic Acid Faradaic Efficiency

5.5. POST CO_2RR CATALYST CHARACTERISATION

5.5.1. SEM

After the CO_2 RR experiments, the catalysts were characterised to see if there was any change in the morphology. Fig. 5.10 - Fig. 5.15 show SEM micrographs of the used catalysts. It can be clearly seen from these figures that the morphology of the catalyst changes as the reaction proceeds. There also seems to be a correlation between the applied potential and the structure of the used catalyst. At lower applied potentials the morphological change is limited to the spherical cluster disintegrating into smaller constituent particles. At higher potentials of -1.5 V dendritic structures start to originate and at the highest potential of -1.6 V distinct dendritic structures can be seen. ECSA measurements need to be conducted after the reaction to ascertain any change due to the formation of the dendrites. An increase in the ECSA could account for the secondary increase in the hydrocarbon production between -1.4 V and -1.6 V.

In a recent study by Huang et.al, they observed a change in morphology with respect to time at a constant potential. They concluded that the dendritic morphology arises due to random collision of particles that segregate. In the initial time periods, the clusters segregate into smaller particles which on further random collisions give rise to the dendritic structures.[45] [46] In the SEM images below it can be seen that at lower potentials there is a segregation of the spherical clusters and at higher potentials they form the dendritic structures. Conducting experiments for longer times at lower potentials should also result in the dendritic structures. It could be hypothesised that the increasing potential accelerates the formation of these dendrites and therefore at higher potentials we see the formation at earlier times than at lower potentials.

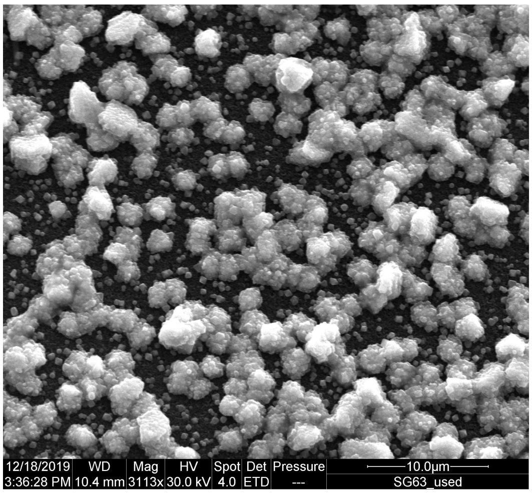

Figure 5.10: SEM after CO_2 RR experiment at -1.1V

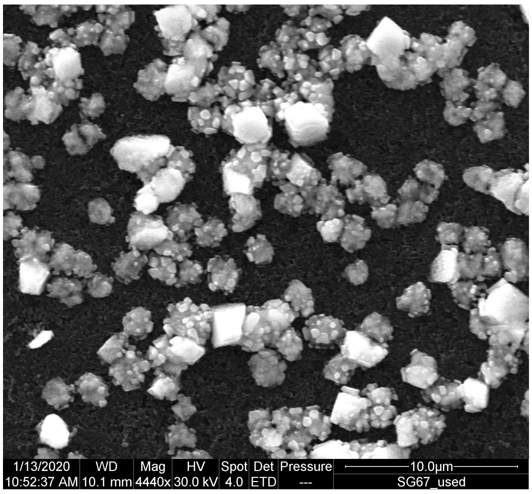

Figure 5.11: SEM after CO_2 RR experiment at -1.2V

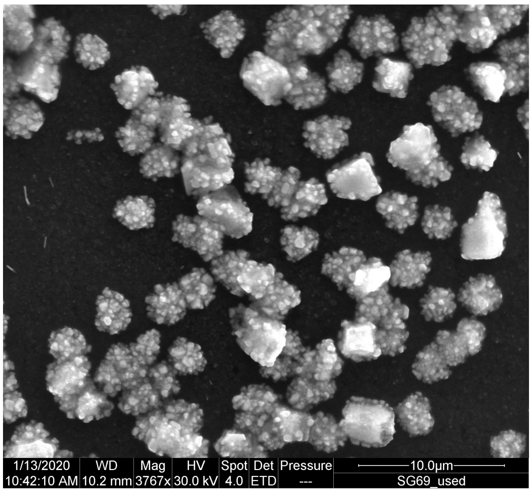
1/13/2020 10:42:10 AM
WD 10.2 mm
Mag 3767x
HV 30.0 kV
Spot 4.0
Det ETD
Pressure ---
10.0µm
SG69_used

Figure 5.12: SEM after CO_2 RR experiment at -1.3V

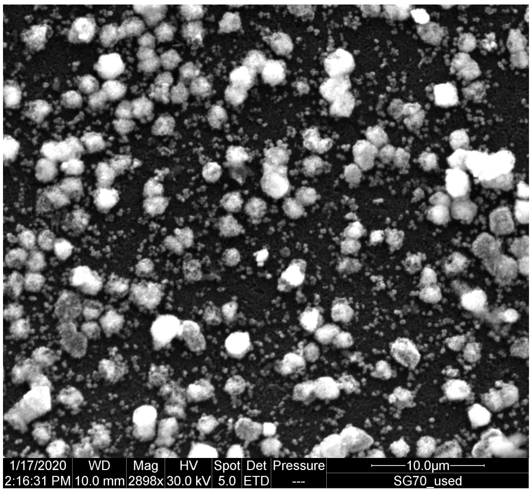
1/17/2020 2:16:31 PM
WD 10.0 mm
Mag 2898x
HV 30.0 kV
Spot 5.0
Det ETD
Pressure ---
10.0µm
SG70_used

Figure 5.13: SEM after CO_2 RR experiment at -1.4V

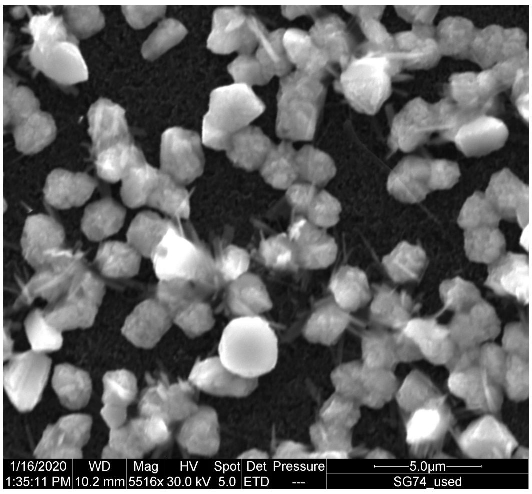
1/16/2020 1:35:11 PM
WD 10.2 mm
Mag 5516x
HV 30.0 kV
Spot 5.0
Det ETD
Pressure ---
5.0µm
SG74_used

Figure 5.14: SEM after CO_2 RR experiment at -1.5V

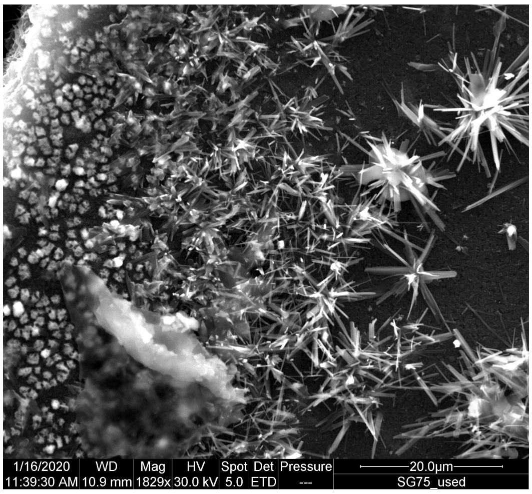
1/16/2020 11:39:30 AM
WD 10.9 mm
Mag 1829x
HV 30.0 kV
Spot 5.0
Det ETD
Pressure ---
20.0µm
SG75_used

Figure 5.15: SEM after CO_2 RR experiment at -1.6V

5.5.2. XRD

Post the CO_2 RR experiments XRD spectra of the used catalysts was collected to see if there was any discernible change in the crystal structure. From the spectra in Fig. 5.16 it can be seen that the ratio of the 111/200 peaks for all the samples is around 3.5. This is considerably lower than the 4.25 (Fig. 4.13) of the as-synthesised catalysts. The presence of methane suggests, that the CO_2 RR takes place primarily on the Cu (111) facets and a decrease in the Cu (111) facets would result in a decrease of methane and ethylene production. As the morphology changes over the course of the reaction, it could be that due to the reduction in the Cu (111)/ Cu (200) ratio there is a decrease in the hydrocarbon production. The resulting FE%'s obtained are due to an interplay between the change in the crystal structure and the change in the ECSA due to the formation of the dendrites. It is also seen that on increasing the potential from -1.1 V to -1.6 V, the 111/200 ratio further decreases from 3.67 to 3.44. Whilst this decrease should result in lower production of methane/ethylene (via the Cu (111) pathway), the increased production between -1.4 V and -1.6 V could be due to the change in the ECSA.

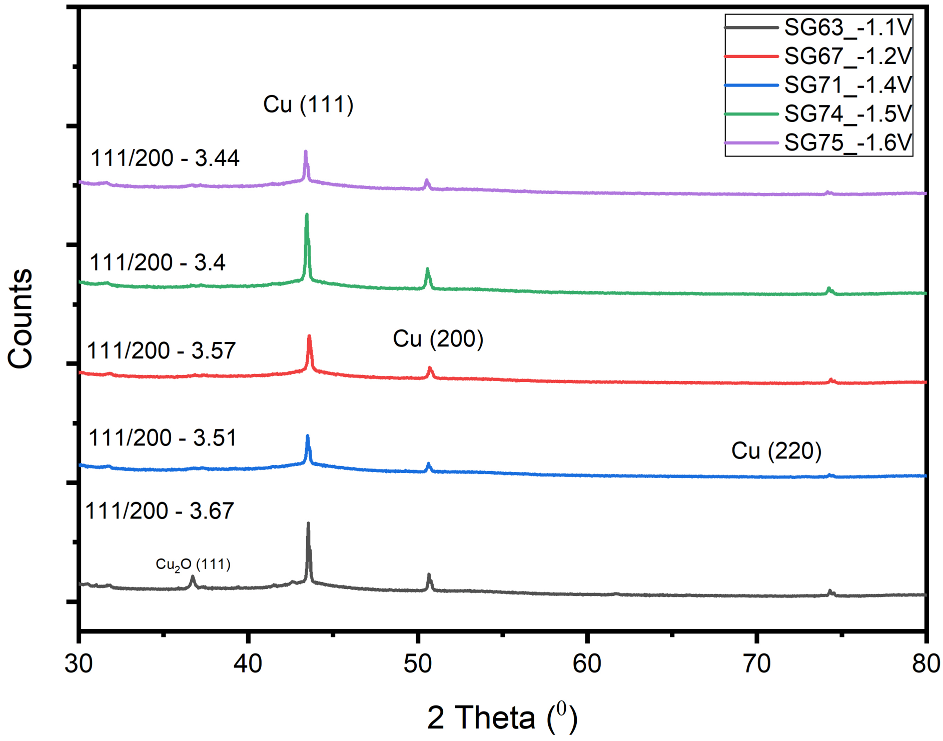

Figure 5.16: XRD Post CO_2 RR

5.6. DISCUSSION

The main reduction products obtained over the course of the experiment were ethylene, formic acid, methane, and hydrogen. The product distribution changes with the applied potential, as is seen in Fig. 5.17 & Fig. 5.18. A predominance of formic acid is seen at the initial potentials, which then slowly decreases. The faradaic efficiencies for the other hydrocarbons increases from -1.1 V to -1.3 V, after which it decreases at -1.4 V. On further increasing the potential to -1.6 V, a secondary increase in the production of hydrocarbons is seen.

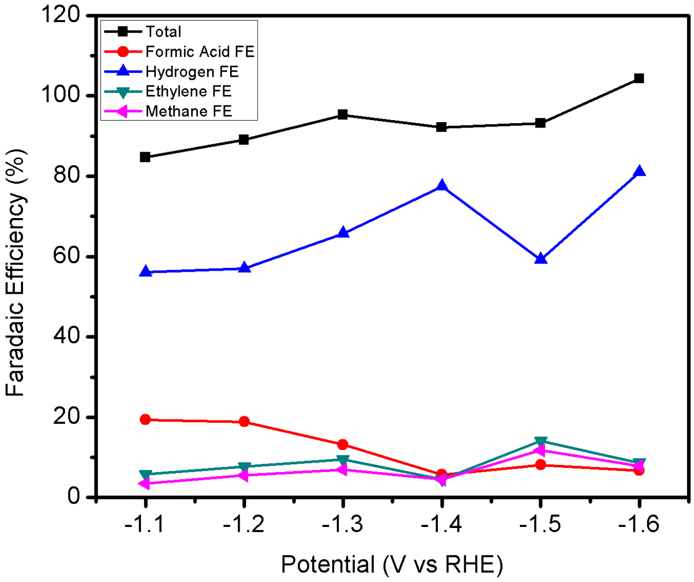

Figure 5.17: CO_2 RR Products vs Potential averaged over two repetitions

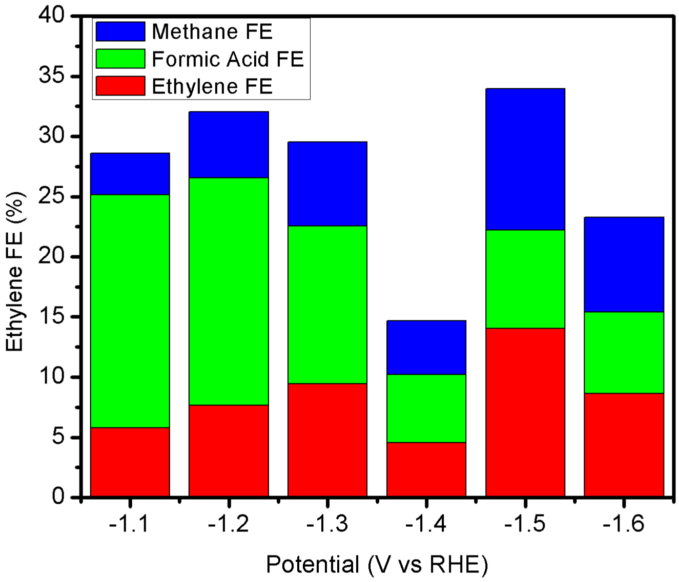

Figure 5.18: CO_2 RR Products vs Potential averaged over two repetitions

This inflection point at -1.4 V is peculiar, as it deviates from the general trend observed over the range of potentials. Additionally, from the reproducibility data in App. E, it is seen that the error is the lowest at -1.4 V therefore the inflection cannot be attributed to experimental error. The initial increase from -1.1 V to -1.3 V and subsequent decrease at -1.4 V is the expected trend observed as per literature. The secondary increase in the production of ethylene/methane at -1.5 V and -1.6 V observed in this study could be caused due to the formation of the dendritic structures which alters the ECSA and the crystal structure.

5.6.1. CATALYST DEACTIVATION

As was seen from the production rate curves of the hydrocarbons the production decreases considerably after the initial 30 minutes of applying the reduction potential. From the charachterisation carried out after the CO_2 RR experiments it was seen that there still was copper on the GDL. The presence of copper on the GDL post the experiment implied that the deactivation of the catalyst was not entirely due to potential leeching of copper from the GDL.

It is postulated in literature that the deactivation of the catalyst could be due to the poisoning of the catalyst surface by impurities (experimental/reaction intermediates), or a change in structure of the catalyst.[19] Poisoning due to graphitic carbon which favours HER over CO_2 RR is seen in the cases where methane is produced.[47] [48] As in this study the formation of methane is observed it could be that the deactivation is indeed due to the deposition of graphitic carbon. To rule out that the role of the electrolyte in the deactivation, experiments were conducted wherein a catalyst was used in an used electrolyte. It was seen that the catalyst still showed activity towards CO_2 RR, thereby also ruling out the role of the electrolyte in the deactivation of the catalyst.

5.7. PULSED ELECTROLYSIS

To increase the lifetime of the catalyst pulsed electrolysis experiments were carried out wherein the reduction potential was applied for 45 minutes and the potential was then reduced to 0V vs Ag/AgCl for the next 15 minutes. Therefore, one cycle of the experiment consisted of a 45 minute period where the CO_2 RR reaction was taking place and a 15 minute period wherein no reduction reaction was occurring. 15 such cycles were ran on the same catalyst to observe the catalytic activity.

The results are shown in Fig. 5.19 - Fig. 5.22. Fig 5.19 depicts the potential vs time and current density vs time relations. The potential was cycled between -2 V vs Ag/AgCl (-1.3 V vs RHE) and 0 V vs Ag/AgCl (0.61 V vs RHE) for each cycle. A gradual increase in the current density is observed in subsequent cycles. Most of the increased current density is used for the hydrogen evolution reaction, as can be understood from Fig. 5.20, wherein the increase in current density directly correlates with an increase in the hydrogen flow. The relation between the ethylene flow, and the current density is not as scalable, seen from Fig. 5.21. The results for the pulsed electrolysis experiments are mentioned in terms of flow rates and not faradaic efficiencies owing to data inconsistencies at the start and end of each pulse originating due to a slight lag between the production of the compound and the application of the pulse.

Fig. 5.22 & Fig. 5.21 depict the relation between the potential pulses/current densities and the ethylene flow rates. It can clearly be seen that the flow rate of ethylene changes with each successive cycle. It is seen that the flow rate decreases in the first 4 cycles, after which it increases from cycle 5-10 and then stabilises between cycle 11-15. Using pulsed electrolysis, we were able to reactivate the catalyst and increases its lifetime from 30 minutes to 15 hours. It is difficult to ascertain the exact cause of this behaviour due to the interplay of various factors. The increasing current density in successive cycles would ideally result in an increased flow rate, potential leeching of the copper into the electrolyte would induce a decrease in the flow rate due to lower catalyst amounts, and change in morphology of the catalyst surface also alters the flow rate due to the change in ECSA and the crystal structure. It could also be that the poisoning impurities desorp from the catalyst surface on the removal of the applied potential. Also, on applying the anodic pulse O V vs Ag/AgCl

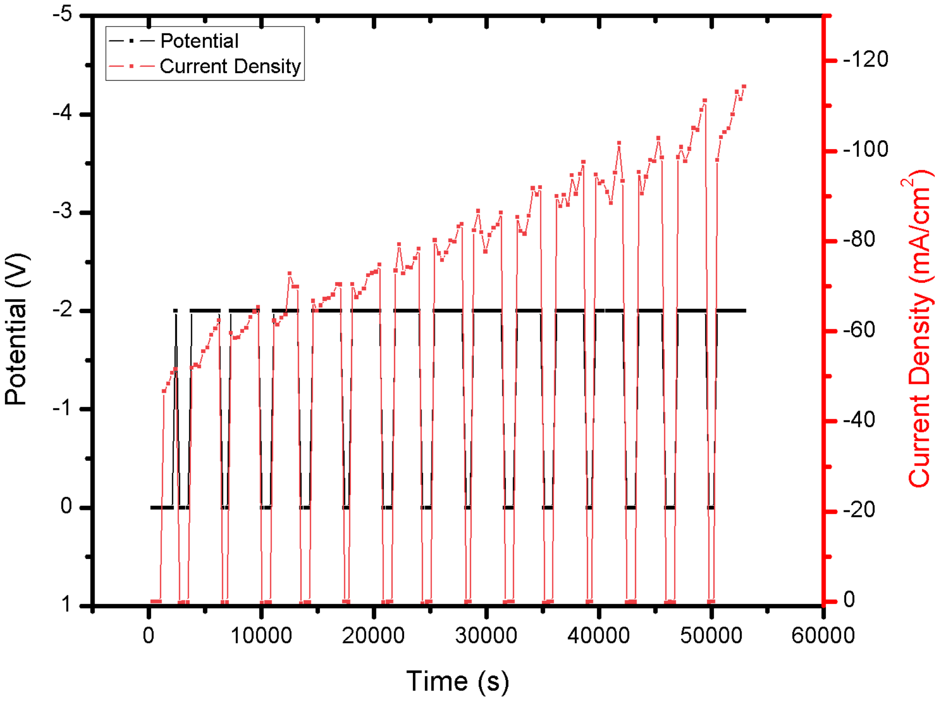

Figure 5.19: Current Density and Potential for the pulsed electrolysis experiments

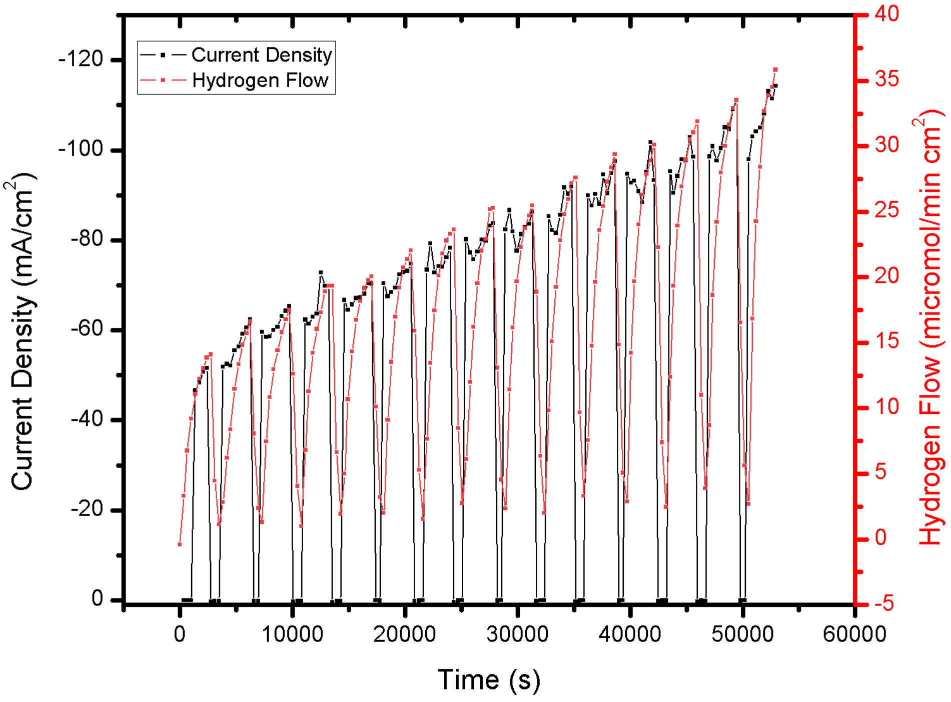

Figure 5.20: Current Density and hydrogen flow rate for the pulsed electrolysis experiments

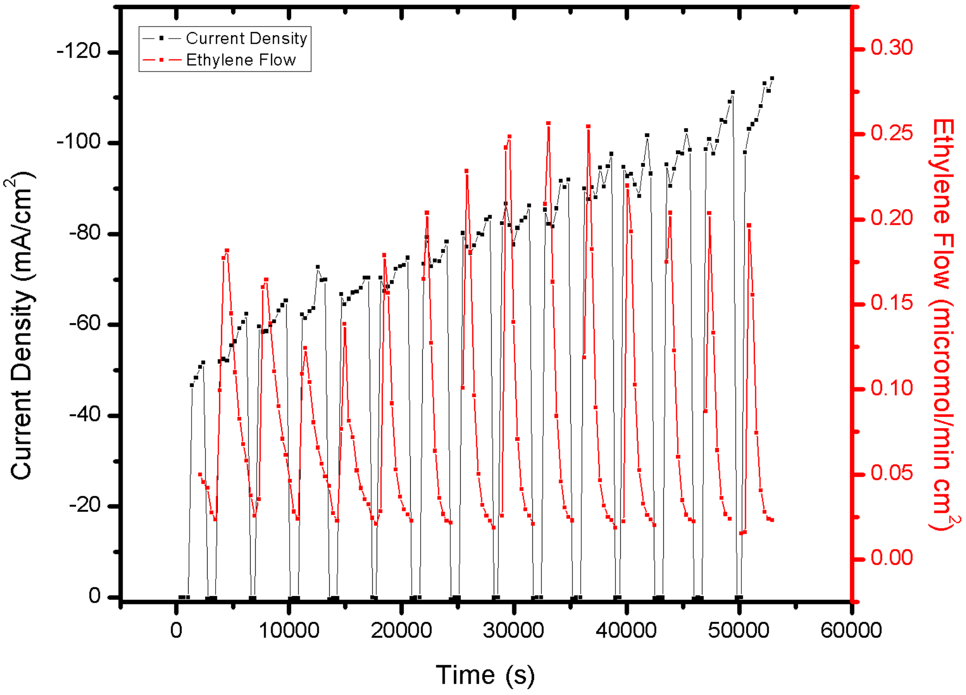

Figure 5.21: Current Density and ethylene flow rate for the pulsed electrolysis experiments

(0.61 V vs RHE) a surface oxide film might be formed which during the CO_2 RR process reduces and gives rise to surface irregularities that promote ethylene growth.[49] To ascertain the exact cause of this behaviour, further in-situ spectroscopic studies would need to be carried out.

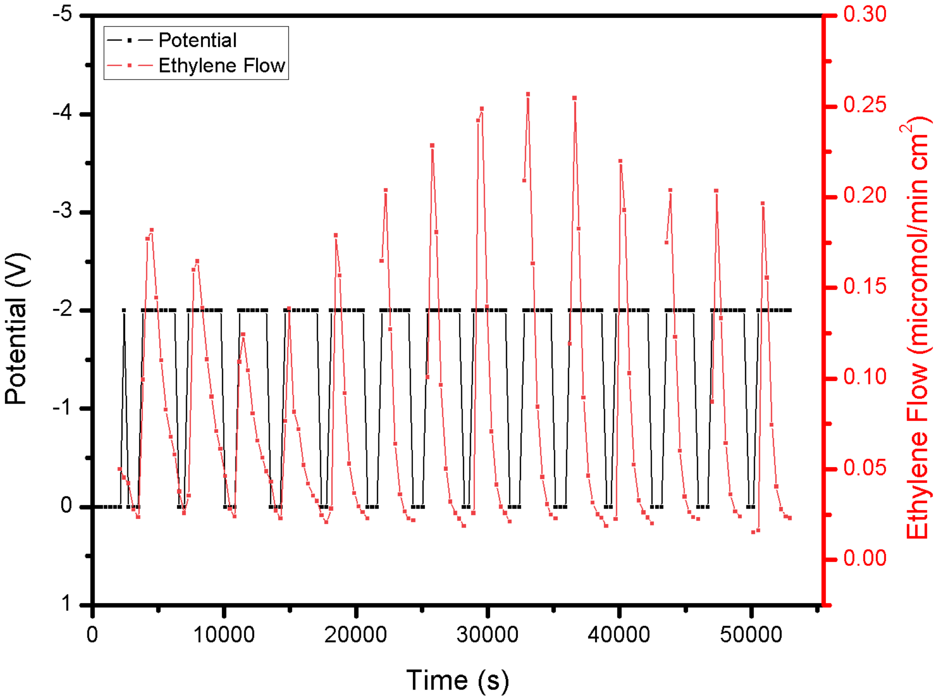

Figure 5.22: Potential and ethylene flow rate for the pulsed electrolysis experiments

6

CONCLUSION & FUTURE OUTLOOK

6.1. CONCLUSION

The aim of this study was to facilitate the transition of CO_2 RR from a lab-scale technique to an industrially feasible technology. The objectives of this study dealt with realising this aim and overcoming two of the many impending obstacles preventing widespread industrial implementation of CO_2 RR.

The main objectives of this study were to :

1. *Synthesize copper based electrocatalysts using an industrially relevant scalable approach*

This was solved by synthesizing the catalysts by electrodeposition which is a technique already widely used in industry. It was seen that by varying the deposition parameters different morphologies of the catalyst could be obtained, ranging from discrete spherical copper micro-clusters to polycrystalline films. This was evident by the SEM images. Additionally, the results from the XRD suggested that by changing the deposition parameters different crystalline structures could also be obtained. As was mentioned in the early sections of the report, the crystalline structure is of paramount importance to the activity/selectivity of the catalyst. Further experiments could be carried out to achieve different crystalline structures resulting in a different catalytic performance.

2. *Investigate the activity/selectivity of selected electrocatalysts for CO_2 RR on GDE*

To improve the production rates of the CO_2 RR GDE's were used. Experiments were conducted to first find out process parameters that were limiting the reproducibility and performance of the catalysts. It was found that not pre-saturating the electrolyte with CO_2 was a major factor affecting the reproducibility of the reaction. Additionally, the CO_2 flow was increased to 10ml/min after initial experiments to avoid any mass transport limitations. Once these process parameters were fixed CO_2 RR experiments were carried out on Morphology 3, and the results of the various products were discussed. A peak FE% of 15% for ethylene and 12% for methane at -1.5 V vs RHE, and at total current densities of 75mA/cm^2 was observed. Formic acid was prevalent at the lower potentials, with a FE of 19% at -1.1 V. The catalysts were characterized before and after the CO_2 RR experiments and a change in the morphology post the CO_2 RR was observed from the SEM micrographs and the XRD spectra. The change in morphology was also found to be dependent on the CO_2 RR potential. Higher applied potentials resulted in dendritic structures. There were also some challenges with regards to the stability of the catalyst as the production of the hydrocarbons drastically dropped after about 30 minutes. This was overcome by using pulsed electrolysis and the catalyst lifetime was increased from 30minutes to 15 hours.

6.2. FUTURE RECOMMENDATIONS

From an experimental perspective a few further experiments/changes that can be incorporated to improve the system are as follows,

- Higher concentration of the electrolyte (3M KOH) to see if there is an improvement in the obtained current densities.
- Incorporating in-situ measurements to better understand the dynamic changes in the morphology of the catalyst, and to ascertain the presence of any adsorbed species on the catalyst surface.
- Optimizing the pulsed electrolysis method by varying the on and off time intervals. Also, characterizing the catalyst surface after regular a certain number of pulses to evaluate any change in morphology.
- Measuring the ECSA and catalyst mass on the GDL after each experiment to quantitatively evaluate the loss of catalyst and/or change in the electrochemically active surface area.
- Employing a larger electroplating bath of $CuSO_4$, to minimize changes in the concentration of copper in solution after each plating experiment.
- Compensating the potential for the internal cell resistance.

From a catalytic perspective various experiments could be carried out to improve the CO_2 RR performance. Some recommendations that can be carried out using the existing equipment in the lab are as follows,

- Testing the copper nanowire catalysts in the electrochemical cell after improving their mechanical stability.
- Spray coating a solution of a proton conducting substance and carbon black on the catalyst surface to improve the conductivity.
- Synthesizing Au-Cu bi-metallic catalysts, by either spray coating or electrodepositing gold on the synthesized copper catalysts. Gold is a known catalyst for CO_2 to CO while copper further reduces CO to multi-carbon compounds.
- Carrying out a comprehensive study on the catalyst growth and the different catalyst morphologies obtainable on the carbon based GDL by electrodeposition. Different time intervals and current densities could be tried for the electrodeposition.
- Synthesising catalysts on different carbon GDL's.

A

GC CALIBRATION

To calculate the Faradaic efficiencies, it is essential to quantitatively determine the gaseous products detected by the GC and the liquid products detected by the HPLC. On determining the amount of product formed, the faradaic efficiency can be calculated using Faraday's laws of electrolysis.

To quantitatively determine the products formed, the TCD & FID detectors were calibrated for six gases, Nitrogen, Hydrogen, Carbon Monoxide, Methane, Ethane, Ethylene. Eight different volumetric ratios were used for the calibration of the hydrocarbons, as shown in Table A.1

Compound				**Volume Ratios**				
Methane	0.983	0.73725	0.4915	0.24575	0.0953	0.071475	0.04765	0.023825
Ethane	0.994	0.7455	0.497	0.2485	0.0951	0.071325	0.04755	0.023775
Ethylene	1.003	0.75225	0.5015	0.25075	0.0969	0.072675	0.04845	0.024225
Carbon Monoxide	0.994	0.7455	0.497	0.2485	0.0974	0.07305	0.0487	0.02435
Nitrogen	96.026	97.0195	98.013	99.0065	99.6153	99.71148	99.80765	99.90383
Total	100	100	100	100	100	100	100	100

Table A.1: Hydrocarbon Gas Mixtures used for calibration

After calibrating the gases and determining the equations of the calibration curves, the volume ratios(%) of each gas flowing through the GC could be ascertained by relating it to the peak area. The peak area was automatically integrated by the Chromeleon 7 software.The volumetric % of all the different gases were thus determined in a similar manner. The volume flow rate for nitrogen was always kept constant at 20ml/min, thus nitrogen volume % was always equal to 20ml/min, this relation enabled us to find us the flow rates of the other measured gases. A sample calculation for is provided below.

$$\text{Measured Peak Area of } H_2 = 0.757 mV * min \tag{A.1}$$

$$\text{Measured Peak Area of } N_2 = 0.313 mv * min \tag{A.2}$$

Using the Calibration Curve for Hydrogen (eq. A.3) the volume % of H_2 corresponding to the peak area is calculated

$$\text{Volume \%}_{\text{ H2}} = 19.209 \times \text{ Peak Area} - .3191 \tag{A.3}$$

Volume % H_2 = 14.22

Similarly using eq. A.4, the volume % of nitrogen corresponding to the peak area is calculated

$$\text{Volume \%}_{\text{ N2}} = 212.62 \times \text{ Peak Area} + 1.003 \tag{A.4}$$

Volume % N_2 = 67.55

We also know that the nitrogen flow rate is 20ml/min, and this corresponds to 67.55% of the total volume flow. Using this the flow rate of hydrogen can also be calculated.

$$\text{FlowRate}_{\text{ H}_2} = \frac{20 \times 14.22}{67.55} \tag{A.5}$$

This gives us a hydrogen flow rate of 4.2108 ml/min. Using the ideal gas relation the production rate in terms of mols was calculated which was used for the calculation of the Faradaic Efficiency.

$$\text{n}_{\text{H}_2} = \frac{4.2108}{22.4} \tag{A.6}$$

This gives a hydrogen production rate of 0.1879 mmol/min averaged over one specific 5.5 minute injection.

In a similar way the concentration of all the other gases were calculated with respect to time.

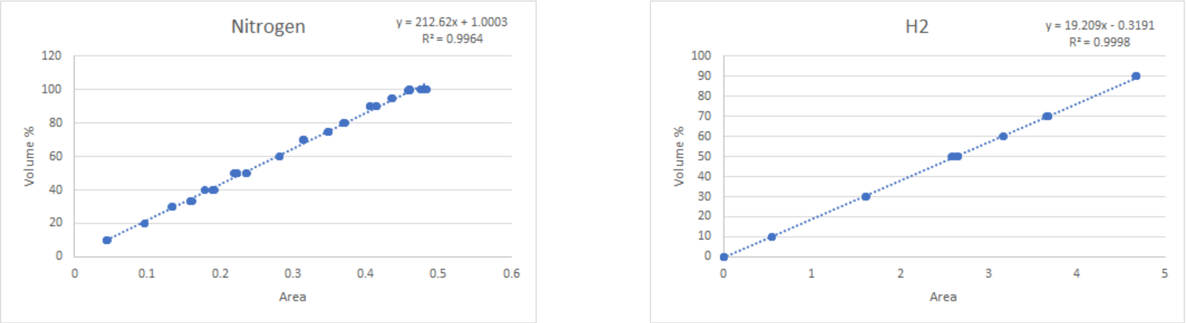

(a) Calibration curve for Nitrogen

(b) Calibration curve for Hydrogen

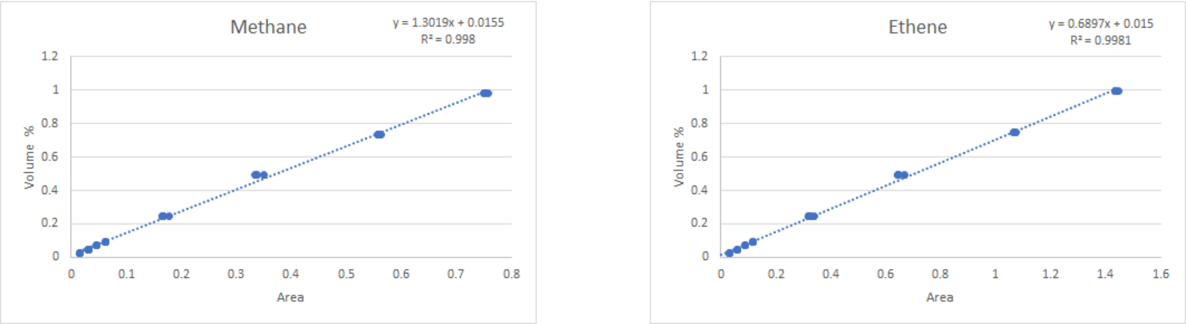

(c) Calibration curve for Methane

(d) Calibration curve for Ethylene

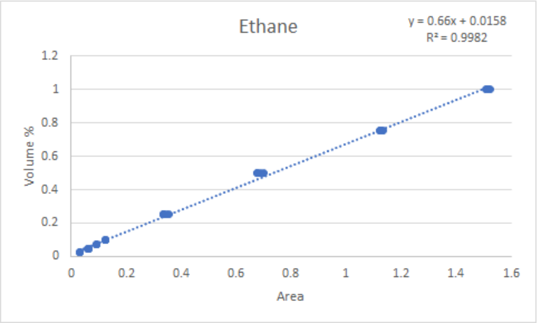

(e) Calibration curve for Ethane

Figure A.1: Calibration Curves for different gases with their corresponding equations and R^2 values

B

HPLC CALIBRATION

Similar to the GC calibration, calibration of the HPLC was required to quantitatively determine the liquid products detected.

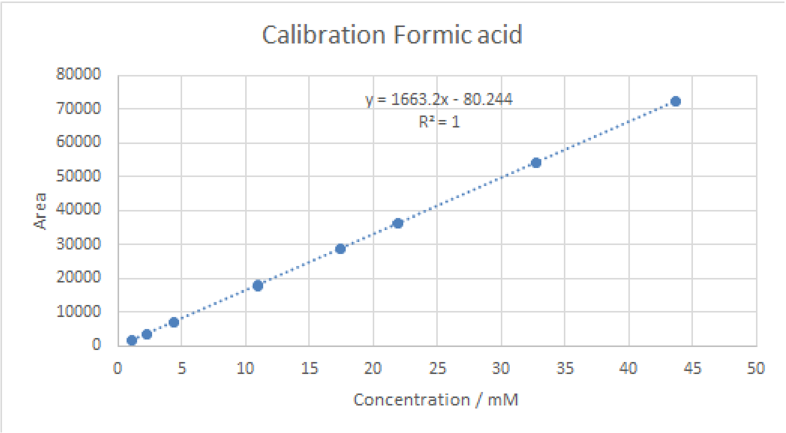

Figure B.1: Calibration Line for Formic Acid

The peak area obtained from the HPLC results, was converted into concentration(mM) using the calibration line depicted in Fig. B.1. The calibration line was determined by using 8 different dilution ratios as mentioned in Table.B.1. After running an HPLC analysis and integrating the peaks, peak areas were obtained. The peak area was then converted into concentration(mM) using the calibration lines. As the volume of the catholyte was kept constant (60ml), from the concentration obtained the number of mols of product formed was determined. On determining the mols of product formed, the faradaic efficiency was calculated using eq. 3.6. The total current passed over the course of the reaction was calculated by integrating the current vs time curve obtained after the potentiostatic experiments.

Sample Name	g Stock	g Total	Dilution	Conc. (mg/ml)	Ret. Time (min)	Peak Area	Conc. (mM)
A	0.2519	10.01	39.73	0.05	17.66	1811.7454	1.099304
A duplo	0.2519	10.01	39.73	0.05	17.63	1785.3828	1.099304
B	0.50	10.02	19.88	0.10	17.66	3629.6111	2.197195
B duplo	0.50	10.02	19.88	0.10	17.64	3532.6707	2.197195
C	1.00	10.02	10.01	0.20	17.65	7131.8799	4.363704
C duplo	1.00	10.02	10.01	0.20	17.64	7149.9702	4.363704
D	2.50	10.01	4.00	0.50	17.65	17853	10.92867
D duplo	2.50	10.01	4.00	0.50	17.63	18044.2	10.92867
E	4.02	10.07	2.50	0.80	17.64	29023	17.44648
E duplo	4.02	10.07	2.50	0.80	17.64	28953.8	17.44648
F	5.02	10.01	2.00	1.01	17.65	36545	21.88197
F duplo	5.02	10.01	2.00	1.01	17.64	36426.8	21.88197
G	7.51	10.02	1.33	1.51	17.64	54387.1	32.75111
G duplo	7.51	10.02	1.33	1.51	17.63	54149.9	32.75111
H	10.00	10.00	1.00	2.01	17.648	72560.7	43.67454
H duplo	10.00	10.00	1.00	2.01	17.63	72599.7	43.67454

Table B.1: Calibration Data for Formic Acid

C

GAS DIFFUSION LAYER PROPERTIES

C.1. GDL PROPERTIES

Gas Diffusion Layer - W1S1009	
Material Type	Woven Carbon Fiber (cloth)
Thickness (nm)	410
Basic Weight(g/m^2	200
Air Permeability(l/m^2/s)	<55
Electrical Resistivity(through plane)	$<13\text{m}\Omega\text{cm}^2$
Tensile Strength	MD: 10N/cm ; XD: 5N/cm
PTFE Treatment	Yes
Microporous Layer	Yes, on one side

Table C.1: Properties of Carbon Cloth W1S1009

C.2. RAMAN SPECTRA

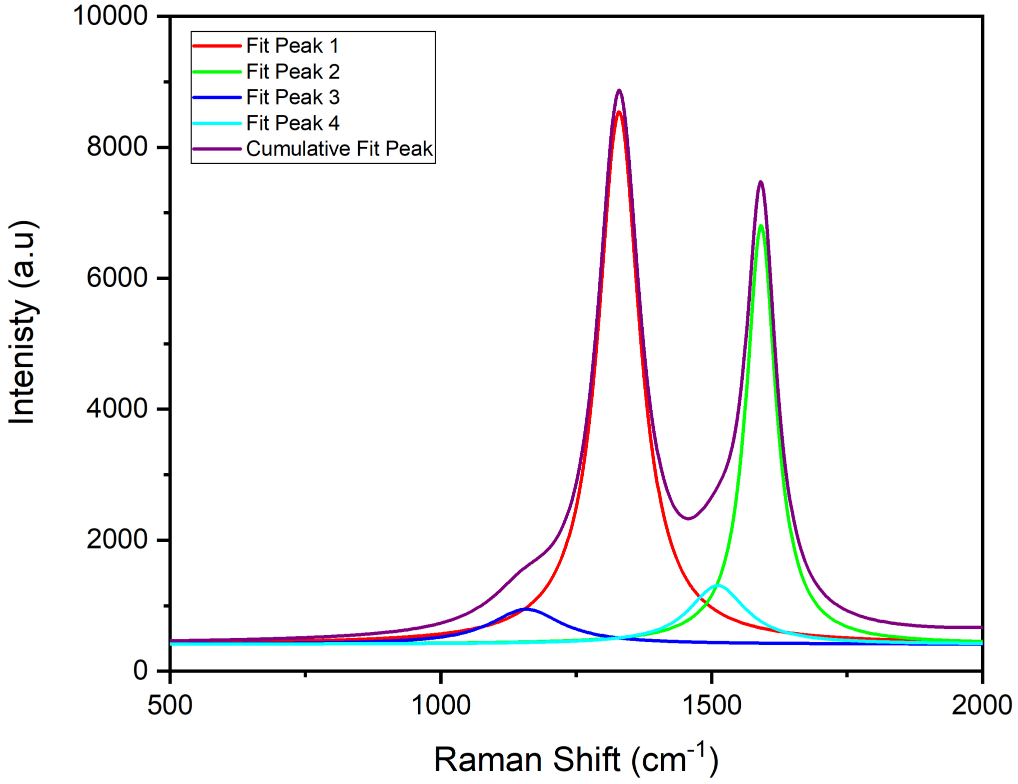

Figure C.1: Raman Spectra of the GDL used

Peak Label	**Peak 1**	**Peak 2**	**Peak 3**	**Peak 4**
Peak type	D1	G	D4	D3
Raman Shift (cm-1)	1328.95	1591.23	1157.69	1511.18
R- sqaure	0.99575			

Table C.2: Raman Spectra peak fitting

D

SEM IMAGES

This Appendix includes enlarged images of the different morphologies obtained.

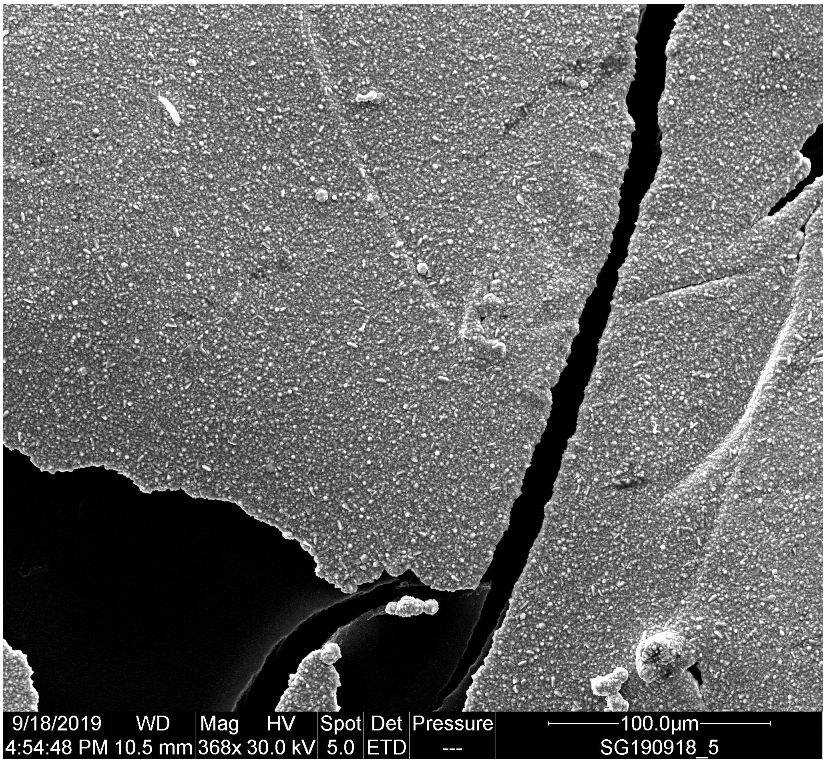
9/18/2019
4:54:48 PM
WD
10.5 mm
Mag
368x
HV
30.0 kV
Spot
5.0
Det
ETD
Pressure

100.0µm
SG190918_5

Figure D.1: SEM Micrograph of Morphology 1 - 350x (Enlarged)

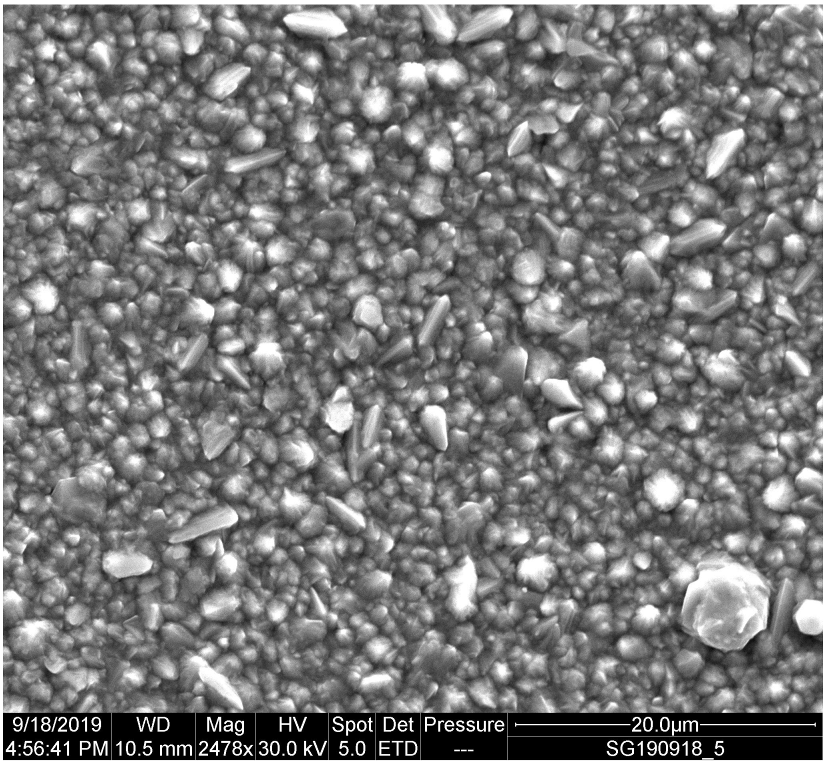
9/18/2019
4:56:41 PM
WD
10.5 mm
Mag
2478x
HV
30.0 kV
Spot
5.0
Det
ETD
Pressure

20.0µm
SG190918_5

Figure D.2: SEM Micrograph of Morphology 1 - 2500x (Enlarged)

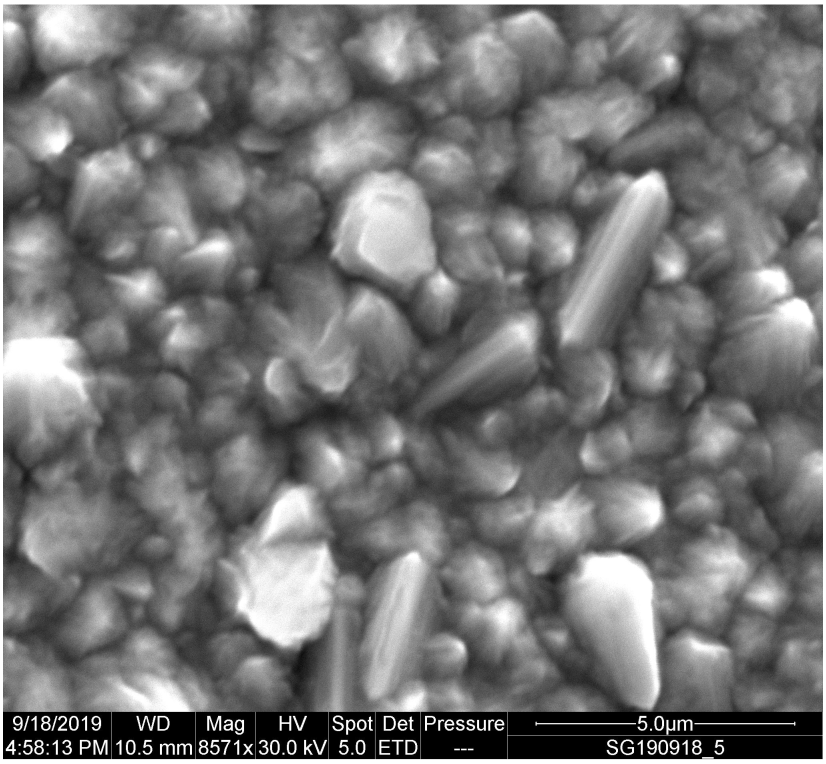
9/18/2019
4:58:13 PM
WD
10.5 mm
Mag
8571x
HV
30.0 kV
Spot
5.0
Det
ETD
Pressure

5.0µm
SG190918_5

Figure D.3: SEM Micrograph of Morphology 1 - 8500x (Enlarged)

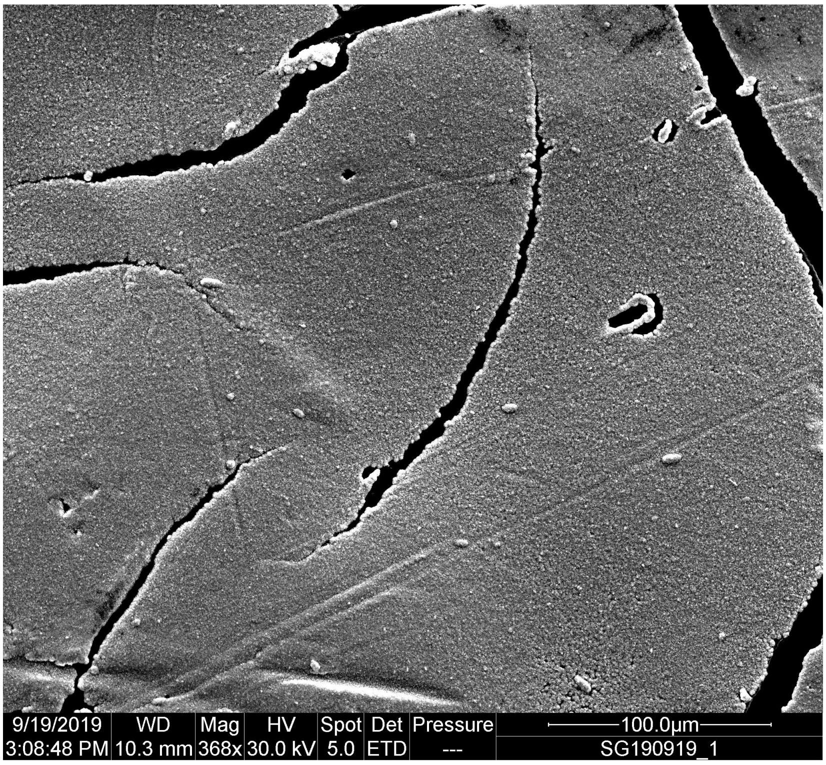
9/19/2019
3:08:48 PM
WD
10.3 mm
Mag
368x
HV
30.0 kV
Spot
5.0
Det
ETD
Pressure

100.0µm
SG190919_1

Figure D.4: SEM Micrograph of Morphology 2 - 250x (Enlarged)

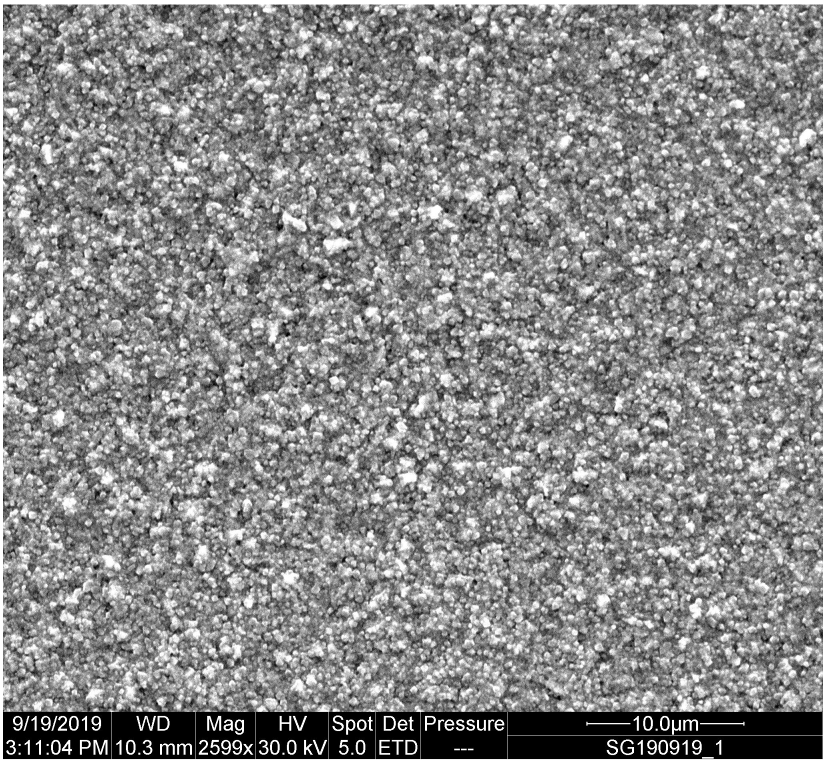
9/19/2019
3:11:04 PM
WD
10.3 mm
Mag
2599x
HV
30.0 kV
Spot
5.0
Det
ETD
Pressure

10.0μm
SG190919_1

Figure D.5: SEM Micrograph of Morphology 2 - 2500x (Enlarged)

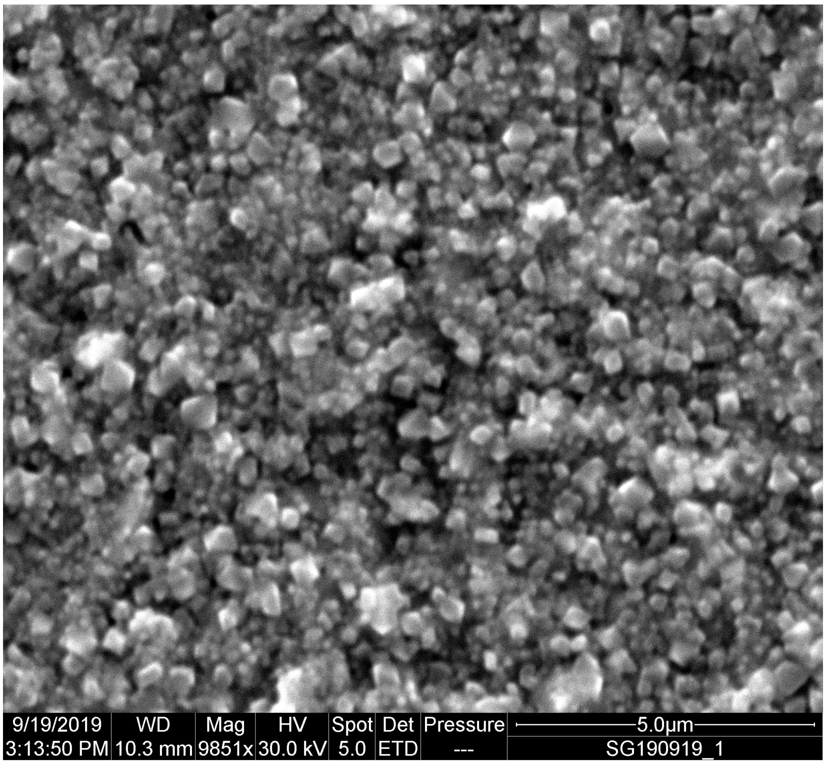
9/19/2019
3:13:50 PM
WD
10.3 mm
Mag
9851x
HV
30.0 kV
Spot
5.0
Det
ETD
Pressure

5.0μm
SG190919_1

Figure D.6: SEM Micrograph of Morphology 2 - 10000x (Enlarged)

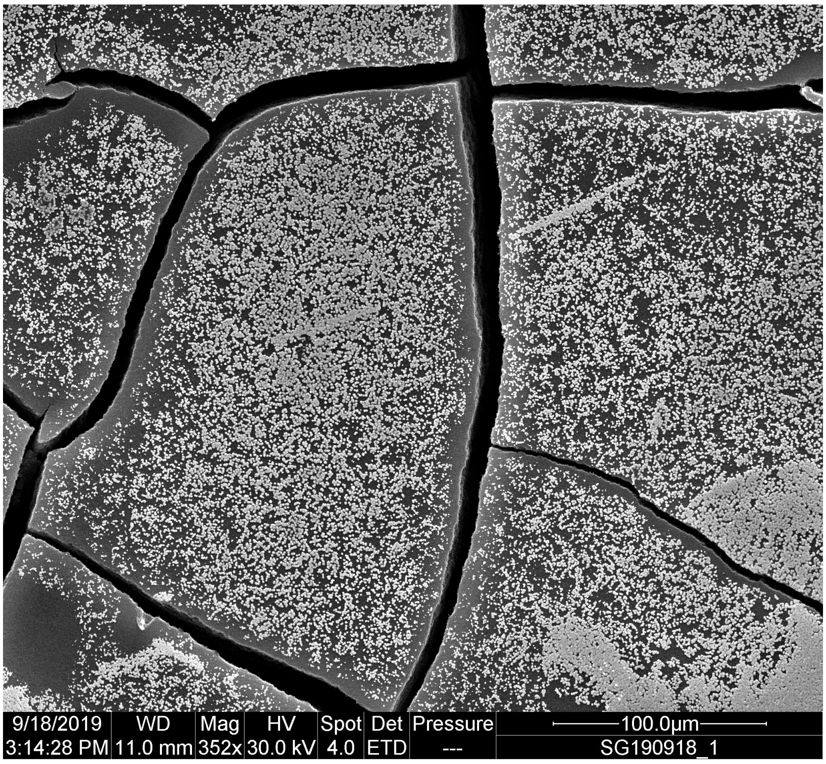
9/18/2019
3:14:28 PM
WD
11.0 mm
Mag
352x
HV
30.0 kV
Spot
4.0
Det
ETD
Pressure

100.0μm
SG190918_1

Figure D.7: SEM Micrograph of Morphology 3 - 350x (Enlarged)

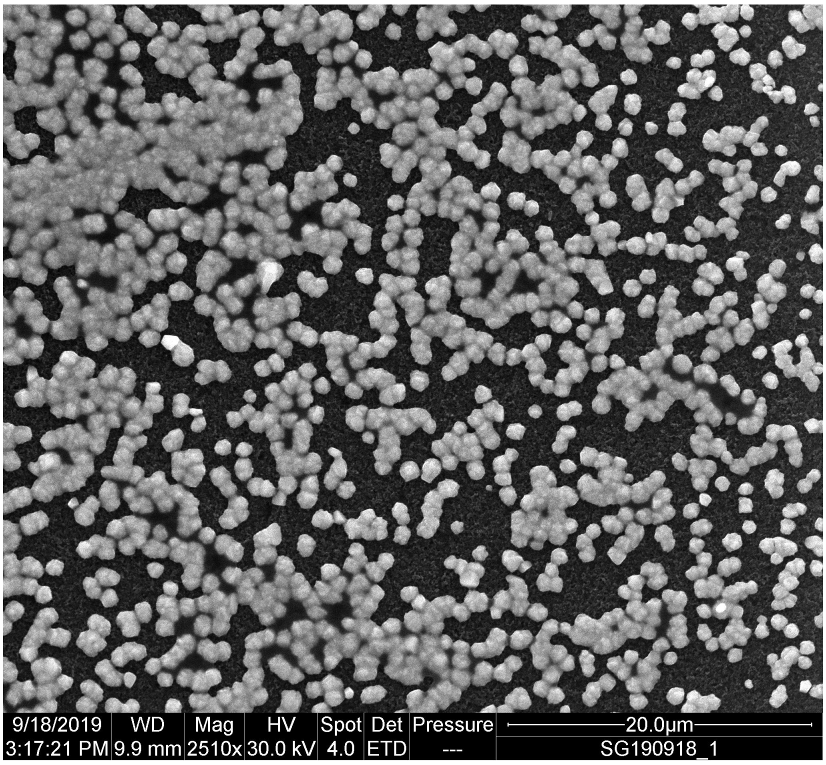
9/18/2019
3:17:21 PM
WD
9.9 mm
Mag
2510x
HV
30.0 kV
Spot
4.0
Det
ETD
Pressure

20.0μm
SG190918_1

Figure D.8: SEM Micrograph of Morphology 3 - 2500x (Enlarged)

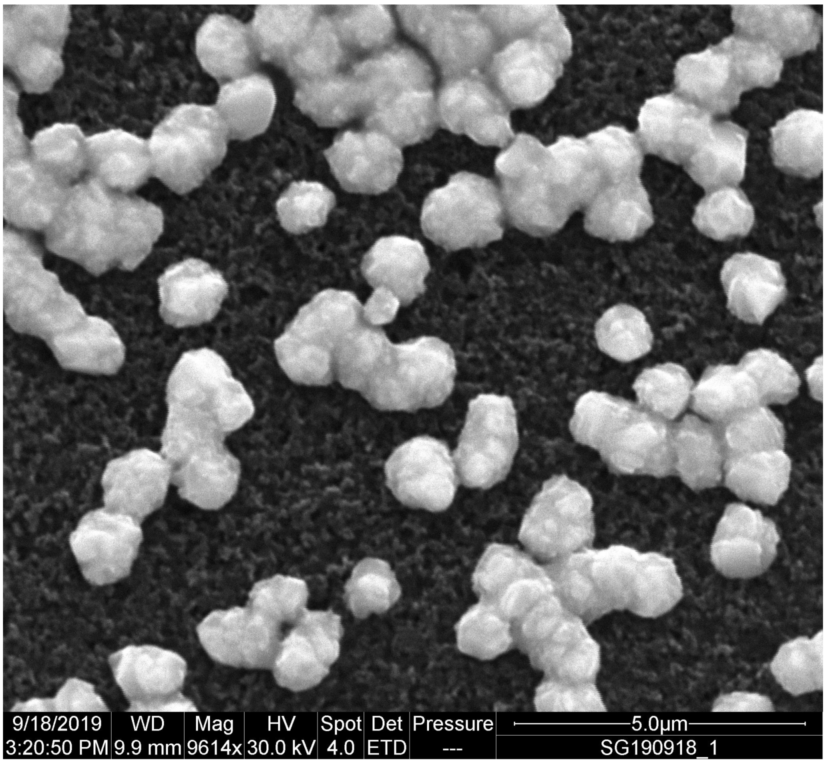
9/18/2019
3:20:50 PM
WD
9.9 mm
Mag
9614x
HV
30.0 kV
Spot
4.0
Det
ETD
Pressure

5.0µm
SG190918_1

Figure D.9: SEM Micrograph of Morphology 3 - 10000x (Enlarged)

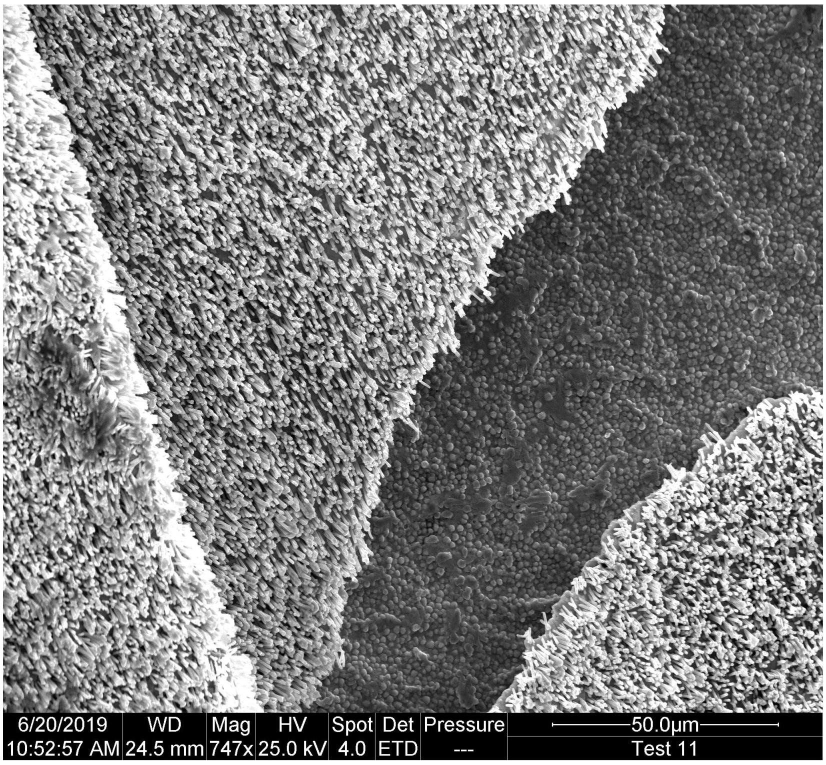
6/20/2019
10:52:57 AM
WD
24.5 mm
Mag
747x
HV
25.0 kV
Spot
4.0
Det
ETD
Pressure

50.0µm
Test 11

Figure D.10: SEM micrograph of Synthesized copper nanowires - 750x (Enlarged)

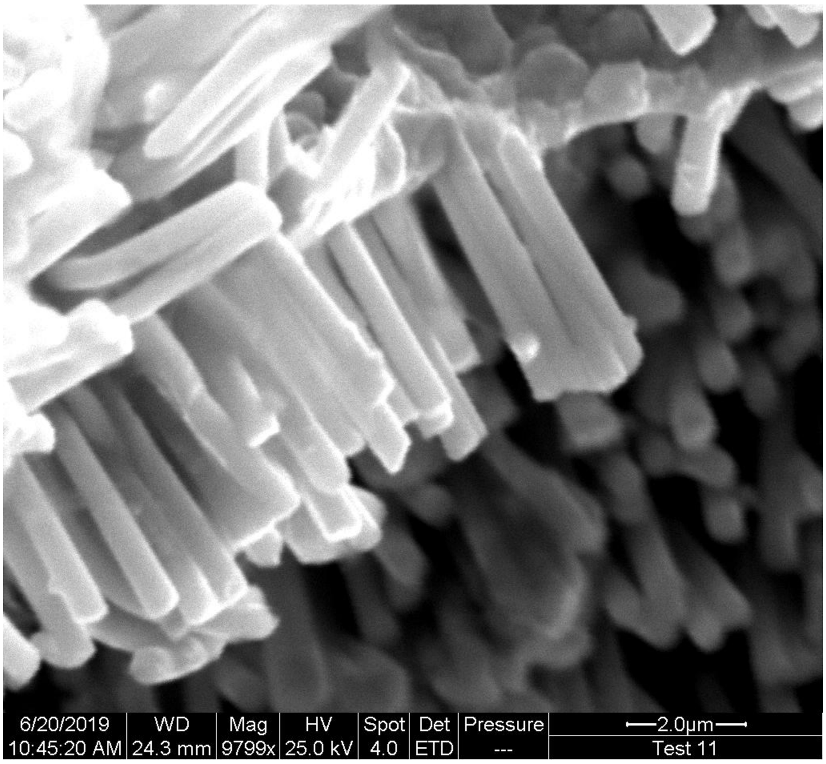
6/20/2019
10:45:20 AM
WD
24.3 mm
Mag
9799x
HV
25.0 kV
Spot
4.0
Det
ETD
Pressure

2.0μm
Test 11

Figure D.11: SEM micrograph of Synthesized copper nanowires - 10000x (Enlarged)

E

SUPPLEMENTARY CO_2 RR DATA

E.1. REACTION PARAMETERS

The reaction parameters for one set of experiments are mentioned below.

Potential (vs RHE)	**Cell Resistance (ohms)**	**pH WE (start)**	**ph CE (start)**	**pH WE (end)**	**ph CE (end)**
1.1	4	7.7	7.7	8.1	7.7
1.2	4.44	7.7	7.7	-	7.76
1.3	3.45	7.67	7.67	8.01	7.7
1.4	4.1	7.67	7.67	8.44	7.36
1.5	2.5	7.68	7.68	8.28	7.63
1.6	3	7.6	7.6	7.9	7.6

E.2. REPRODUCIBILITY

Potential	*V vs RHE*	**-1.1**	**-1.2**	**-1.3**	**-1.4**	**-1.5**	**-1.6**
Current Density	*mA/cm2*	22.415	36.17	42.805	60.445	75.149	87.775
Current Density Error	*mA/cm2*	4.325	2.84	0.205	4.305	2.609	13.825
Methane Avg FE	*%*	3.46	5.495	6.96	4.45	11.75	7.86
Methane Error	*%*	0.41	1.465	2.55	0.43	0.78	5.2
Ethylene Avg FE	*%*	5.81	7.67	9.43	4.54	14.07	8.65
Ethylene Error	*%*	1.13	0.33	0	0.16	3.02	5.89
Formic Acid Avg FE	*%*	19.33	18.89	13.13	5.68	8.135	6.75
Formic Acid Error	*%*	0.84	0.26	1.31	1.05	0.615	2.15

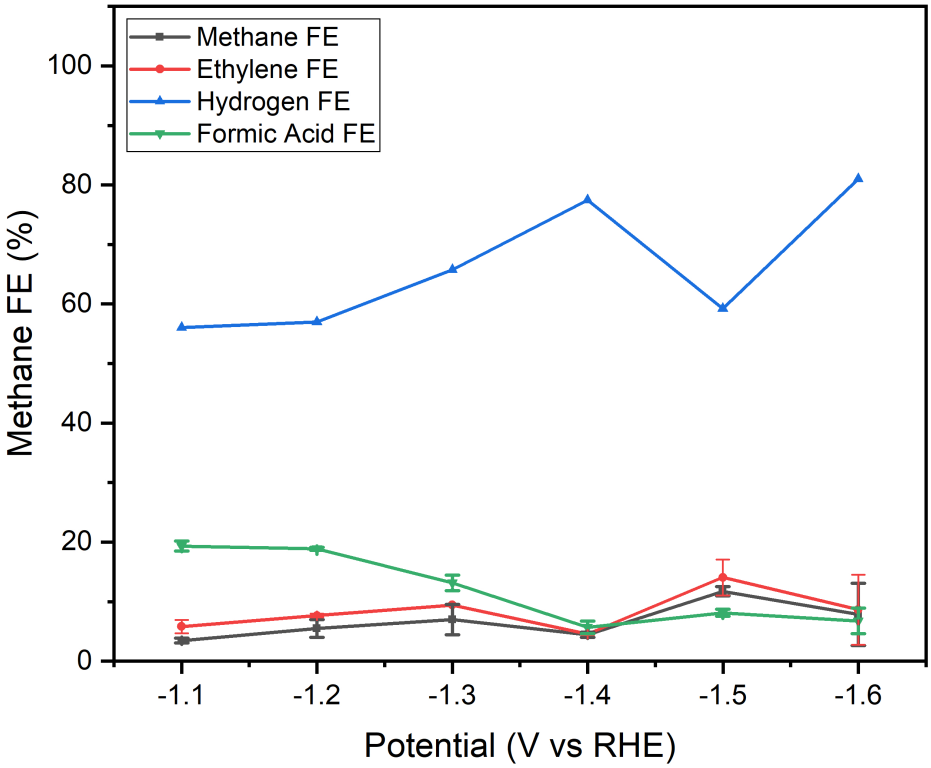

Figure E.1: FE% of the products with error

Glossary

CCU Carbon Capture & Utilization.

CO_2 Carbon Dioxide.

CO_2 RR Carbon Dioxide Reduction Reaction.

CV Cycliv Voltammetry.

ECSA Electrochemical Surface Area.

EDX Energy Dispersive X-ray Spectroscopy.

FE% Faradaic Efficiency.

FID Flame Ionization Detector.

GC Gas Chromatography.

GDE Gas Diffusion Electrode.

GDL Gas Diffusion Layer.

HER Hydrogen Evolution Reaction.

HPLC High Performance Liquid Chromatography.

OER Oxygen Evolution Reaction.

PCTE Track-etched Polycarbonate.

PEEK Polyether ether ketone .

PTFE Polytetrafluoroethene.

RHE Reversible Hydrogen Electrode.

SEM Scanning Electron Microscope.

SHE Standard Hydrogen Electrode.

TCD Thermal Conductivity Detector.

XRD X-Ray Diffraction.

BIBLIOGRAPHY

[1] National Aeronautics and Space Administration, *Global climate change- vital signs of the planet,* (2019).

[2] National Oceanic and Atmospheric Administration, *Atmospheric co$_2$ levels - direct measurement data,* (2019).

[3] Goddard Institute for Space Studies (GISS). , *Global land-ocean temperature index,* (2019).

[4] NASA Goddard Space Flight Center, *Sea level - vital signs,* (2019).

[5] B. Netz, O. Davidson, P. Bosch, R. Dave, L. Meyer, *et al.*, *Climate change 2007: Mitigation. contribution of working group iii to the fourth assessment report of the intergovernmental panel on climate change. summary for policymakers.* Climate change 2007: Mitigation. Contribution of Working Group III to the Fourth Assessment Report of the Intergovernmental Panel on Climate Change. Summary for Policymakers. (2007).

[6] D. T. Whipple and P. J. Kenis, *Prospects of co2 utilization via direct heterogeneous electrochemical reduction,* The Journal of Physical Chemistry Letters **1**, 3451 (2010).

[7] M. Ma, K. Djanashvili, and W. A. Smith, *Selective electrochemical reduction of co 2 to co on cuo-derived cu nanowires,* Physical Chemistry Chemical Physics **17**, 20861 (2015).

[8] K. P. Kuhl, E. R. Cave, D. N. Abram, and T. F. Jaramillo, *New insights into the electrochemical reduction of carbon dioxide on metallic copper surfaces,* Energy & Environmental Science **5**, 7050 (2012).

[9] G. Chui, *Plastics, fuels and chemical feedstocks from co2? they're working on it,* (2019).

[10] M. Ma and W. A. Smith, *Nanostructured catalysts for the electrochemical reduction of co 2,* in *Anisotropic and Shape-Selective Nanomaterials* (Springer, 2017) pp. 337–373.

[11] D. S. Ripatti, T. R. Veltman, and M. W. Kanan, *Carbon monoxide gas diffusion electrolysis that produces concentrated c2 products with high single-pass conversion,* Joule **3**, 240 (2019).

[12] D. Higgins, C. Hahn, C. Xiang, T. F. Jaramillo, and A. Z. Weber, *Gas-diffusion electrodes for carbon dioxide reduction: a new paradigm,* ACS Energy Letters **4**, 317 (2018).

[13] T. Burdyny and W. A. Smith, *Co 2 reduction on gas-diffusion electrodes and why catalytic performance must be assessed at commercially-relevant conditions,* Energy & Environmental Science **12**, 1442 (2019).

[14] Y. Y. Birdja, E. Pérez-Gallent, M. C. Figueiredo, A. J. Göttle, F. Calle-Vallejo, and M. T. Koper, *Advances and challenges in understanding the electrocatalytic conversion of carbon dioxide to fuels,* Nature Energy **4**, 732 (2019).

[15] K. Ogura, *Electrochemical reduction of carbon dioxide to ethylene: mechanistic approach,* Journal of CO2 Utilization **1**, 43 (2013).

[16] H. Miyake, T. Okada, G. Samjeské, and M. Osawa, *Formic acid electrooxidation on pd in acidic solutions studied by surface-enhanced infrared absorption spectroscopy,* Physical Chemistry Chemical Physics **10**, 3662 (2008).

[17] Y. i. Hori, *Electrochemical co 2 reduction on metal electrodes,* in *Modern aspects of electrochemistry* (Springer, 2008) pp. 89–189.

[18] P. Amos, H. Louis, K. Adesina Adegoke, E. A. Eno, A. O. Udochukwu, and T. Odey Magub, *Understanding the mechanism of electrochemical reduction of co2 using cu/cu-based electrodes: A review,* Asian Journal of Nanosciences and Materials **1**, 183 (2018).

[19] S. Nitopi, E. Bertheussen, S. B. Scott, X. Liu, A. K. Engstfeld, S. Horch, B. Seger, I. E. Stephens, K. Chan, C. Hahn, *et al.*, *Progress and perspectives of electrochemical co2 reduction on copper in aqueous electrolyte,* Chemical reviews **119**, 7610 (2019).

[20] R. Kortlever, J. Shen, K. J. P. Schouten, F. Calle-Vallejo, and M. T. Koper, *Catalysts and reaction pathways for the electrochemical reduction of carbon dioxide,* The journal of physical chemistry letters **6**, 4073 (2015).

[21] L.-C. Weng, A. T. Bell, and A. Z. Weber, *Modeling gas-diffusion electrodes for co 2 reduction,* Physical Chemistry Chemical Physics **20**, 16973 (2018).

[22] C. Zhao and J. Wang, *Electrochemical reduction of co2 to formate in aqueous solution using electrodeposited sn catalysts,* Chemical Engineering Journal **293**, 161 (2016).

[23] K. Liu, W. A. Smith, and T. Burdyny, *Introductory guide to assembling and operating gas diffusion electrodes for electrochemical co2 reduction,* ACS energy letters **4**, 639 (2019).

[24] K. Schouten, Y. Kwon, C. Van der Ham, Z. Qin, and M. Koper, *A new mechanism for the selectivity to c 1 and c 2 species in the electrochemical reduction of carbon dioxide on copper electrodes,* Chemical Science **2**, 1902 (2011).

[25] S. P. Liu, M. Zhao, W. Gao, and Q. Jiang, *Mechanistic insights into the unique role of copper in co2 electroreduction reactions,* ChemSusChem **10**, 387 (2017).

[26] A. J. Garza, A. T. Bell, and M. Head-Gordon, *Mechanism of co2 reduction at copper surfaces: pathways to c2 products,* ACS Catalysis **8**, 1490 (2018).

[27] M. Gattrell, N. Gupta, and A. Co, *A review of the aqueous electrochemical reduction of co2 to hydrocarbons at copper,* Journal of Electroanalytical Chemistry **594**, 1 (2006).

[28] M. Ma, *Selective electrocatalytic co2 conversion on metal surfaces,* (2017).

[29] C. Shi, H. A. Hansen, A. C. Lausche, and J. K. Nørskov, *Trends in electrochemical co 2 reduction activity for open and close-packed metal surfaces,* Physical Chemistry Chemical Physics **16**, 4720 (2014).

[30] M. Jaspers, *Electrochemical reduction of carbon dioxide to carbon monoxode: A study on gold as a catalyst* (TNO Restricted, 2019).

[31] L. Han, W. Zhou, and C. Xiang, *High-rate electrochemical reduction of carbon monoxide to ethylene using cu-nanoparticle-based gas diffusion electrodes,* ACS Energy Letters **3**, 855 (2018).

[32] M. E. Leonard, L. E. Clarke, A. Forner-Cuenca, S. M. Brown, and F. R. Brushett, *Investigating electrode flooding in a flowing electrolyte, gas-fed carbon dioxide electrolyzer,* ChemSusChem (2019).

[33] C.-T. Dinh, T. Burdyny, M. G. Kibria, A. Seifitokaldani, C. M. Gabardo, F. P. G. De Arquer, A. Kiani, J. P. Edwards, P. De Luna, O. S. Bushuyev, *et al.*, *Co2 electroreduction to ethylene via hydroxide-mediated copper catalysis at an abrupt interface,* Science **360**, 783 (2018).

[34] M. Jouny, W. Luc, and F. Jiao, *High-rate electroreduction of carbon monoxide to multi-carbon products,* Nature Catalysis **1**, 748 (2018).

[35] A. J. Bard, L. R. Faulkner, *et al.*, *Fundamentals and applications,* Electrochemical Methods **2**, 580 (2001).

[36] N. P. Prasad, *Electrochemical reduction of carbon dioxide to syngas: A study on gold as a catalyst* (TNO Restricted, 2018).

[37] E. Stauffer, J. Dolan, and R. Newman, *Fire Debris Analysis* (Elsevier Science, 2007).

[38] S. Fanali, P. R. Haddad, C. F. Poole, and M.-L. Riekkola, *Liquid Chromatography - Fundamentals and Instrumentation, Volume 1 (2nd Edition)* (Elsevier, 2017).

[39] G. Hübschen, I. Altpeter, R. Tschuncky, and H.-G. Herrmann, *Materials characterization using nondestructive evaluation (NDE) methods* (Woodhead Publishing, 2016).

[40] N. Elgrishi, K. J. Rountree, B. D. McCarthy, E. S. Rountree, T. T. Eisenhart, and J. L. Dempsey, *A practical beginner's guide to cyclic voltammetry,* Journal of Chemical Education **95**, 197 (2018).

[41] D. R. Lowde, J. O. Williams, and B. D. McNicol, *The characterisation of catalyst surfaces by cyclic voltammetry,* Applications of surface science **1**, 215 (1978).

[42] C. C. McCrory, S. Jung, J. C. Peters, and T. F. Jaramillo, *Benchmarking heterogeneous electrocatalysts for the oxygen evolution reaction,* Journal of the American Chemical Society **135**, 16977 (2013).

[43] F. P. G. de Arquer, C.-T. Dinh, A. Ozden, J. Wicks, C. McCallum, A. R. Kirmani, D.-H. Nam, C. Gabardo, A. Seifitokaldani, X. Wang, *et al.*, *Co2 electrolysis to multicarbon products at activities greater than 1 a cm-2,* Science **367**, 661 (2020).

[44] D. Raciti, M. Mao, J. H. Park, and C. Wang, *Mass transfer effects in co 2 reduction on cu nanowire electrocatalysts,* Catalysis Science & Technology **8**, 2364 (2018).

[45] J. Huang, N. Hörmann, E. Oveisi, A. Loiudice, G. L. De Gregorio, O. Andreussi, N. Marzari, and R. Buonsanti, *Potential-induced nanoclustering of metallic catalysts during electrochemical co 2 reduction,* Nature communications **9**, 1 (2018).

[46] K. Manthiram, Y. Surendranath, and A. P. Alivisatos, *Dendritic assembly of gold nanoparticles during fuel-forming electrocatalysis,* Journal of the American Chemical Society **136**, 7237 (2014).

[47] Z. Weng, X. Zhang, Y. Wu, S. Huo, J. Jiang, W. Liu, G. He, Y. Liang, and H. Wang, *Self-cleaning catalyst electrodes for stabilized co2 reduction to hydrocarbons,* Angewandte Chemie International Edition **56**, 13135 (2017).

[48] R. Kas, R. Kortlever, H. Yılmaz, M. T. Koper, and G. Mul, *Manipulating the hydrocarbon selectivity of copper nanoparticles in co2 electroreduction by process conditions,* ChemElectroChem **2**, 354 (2015).

[49] A. Engelbrecht, C. Uhlig, O. Stark, M. Hämmerle, G. Schmid, E. Magori, K. Wiesner-Fleischer, M. Fleischer, and R. Moos, *On the electrochemical co2 reduction at copper sheet electrodes with enhanced long-term stability by pulsed electrolysis*, Journal of The Electrochemical Society **165**, J3059 (2018).